A DETERMINATION OF THE FORMATION RATE OF MUONIC HYDROGEN MOLECULES IN THE MUCAP EXPERIMENT

BY

SARA ANITA KNAACK

DISSERTATION

Submitted in partial fulfillment of the requirements
for the degree of Doctor of Philosophy in Physics
in the Graduate College of the
University of Illinois at Urbana-Champaign, 2012

Urbana, Illinois

Doctoral Committee:

Professor Emeritus Paul Debevec, Chair
Professor David Hertzog, Adviser
Research Professor Peter Kammel, Director of Research
Professor Aida El-Khadra
Associate Professor Raffi Budakian

Abstract

The MuCap experiment measures the μ^- disappearance rate, λ_-, in a gaseous hydrogen time projection chamber (TPC) and compares it to the free μ^+ decay rate, λ_+, to obtain the μp singlet capture rate Λ_{S}. The motivation is a determination of the pseudoscalar form factor, g_P, of the proton, which relates quadratically to Λ_{S}. A μp atom, created after a muon stops in the TPC, can form molecular hydrogen at the rate $\lambda_{pp\mu}$. Muon capture from the molecular state is slower than from the singlet state and $\lambda_{pp\mu}$ must be known to correctly extract Λ_{S}. New data from the MuCap experiment reduces the uncertainty $\delta\lambda_-$ by a factor of 2.4, making the improved measurement of $\lambda_{pp\mu}$ critical.

This work presents results for $\lambda_{pp\mu}$ based on data obtained using an argon-doped hydrogen gas, but under otherwise identical TPC conditions as the main MuCap data set taken with ultra pure hydrogen. Argon introduces additional atomic processes involving the muon, which affect the time spectra of muon decay electrons and capture neutrons. Fits to these data determine $\lambda_{pp\mu}$ to a precision that is a significant improvement to the current world average. The main results are extracted from the decay electron time spectrum, which determines $\lambda_{pp\mu}$ to a relative precision of $\approx 3\%$, a threefold improvement compared to previous efforts. The measurement of $\lambda_{pp\mu}$ presented in this thesis contributes to a clear interpretation of the final result of the MuCap experiment.

To my mother,

for her love and gentle care,

and my father,

for his love and encouragement of creativity.

Acknowledgments

I am gratified to recognize excellent scientific advising throughout my graduate student experience. My adviser David Hertzog, and director of research Peter Kammel, have been the core of that. This project is a success I am proud of, and grateful to have been a part of. Through learning many new skills and acquiring new knowledge I have had the best possible people and resources around me. I thank them both for their patience and guidance in that process. I also thank Paul Debevec for his mentorship early in my graduate student career.

This work has relied on the support of the MuCap collaboration, the members of which I recognize as contributors. Those are: V.A. Andreev, T. I. Banks, R.M. Carey, T.A. Case, D.B. Chitwood, S.M. Clayton, K.M. Crowe, J. Deutsch, J. Egger, S.J. Freedman, V.A. Ganzha, T. Gorringe, F.E. Gray, D.W. Hertzog, M. Hildebrandt, P. Kammel, P.A. Kravtsov, A.G. Krivshich, B. Lauss, K.R. Lynch, E.M. Maev, F. Mulhauser, C.S. Özben, C. Petitjean, G.E. Petrov, R. Prieels, G.N. Schapkin, G.G. Semenchuk, M.A. Soroka, V. Tischenko, A.A. Vasilyev, A.A. Vorobyov, M. Vznuzdaev and P. Winter. Within the collaboration I particularly recognize Claude Petitjean, Malte Hildebrandt, Bernhardt Lauss, Marat Vznuzdaev, Tim Gorringe and Fred Gray, who oversaw various technical aspects of this experiment. Their contributions to the realization of this work are greatly appreciated. I especially thank Tim Gorringe for his participation in this project.

I have benefited greatly from working with the other graduate students and the post-docs in our research group over the years. Those individuals include Ron McNabb, Dan Chitwood, Steven Clayton, David Webber, Michael Murray, Jason Crnkovic, Brendan Kiburg and Peter Winter, among others. In particular I thank Brendan Kiburg and Peter Winter for their

contributions to the MuCap experiment, and as colleagues these past five years. I also acknowledge the careful and helpful support of Peter Winter in the preparation of this document.

I also appreciate the support of the Nuclear Physics Laboratory (NPL) and University of Illinois Urbana-Champaign physics department staff. Those persons include Penny Sigler, Mike Suchor, Wendy Wimmer, and Melodee Schweighart. From ensuring my Research Assistant status was up to date, to multiple Swiss visa applications, they have helped make this research possible.

A move in the late stages of a thesis project is a challenge, one I faced with my colleagues two years ago. I recognize the University of Washington (UW) department of physics and Center for Experimental Nuclear Physics and Astrophysics staff for their welcome and support. It has been a terrific opportunity and privilege to be at UW.

I thank my many friends from my time in Urbana. My first-year study partners Matt, Sarah, Suzie, Keiko, Charmaine and Zack, and my dear friends Jana and Francesca all have a place in my memories. I recognize Serena, Toni, Ibrahim and Ry for their camaraderie and friendship as well. To my newer Seattle friends I also extend my thanks.

Finally, my enduring gratitude goes to my parents, grandparents, my sisters, and the rest of my family for their love and care. I love you all dearly. Here it is, the end of an incredible journey. Regrettably, I will have omitted important people who were also a part of my success. To all who have helped me along the way to this achievement, thank you.

Funding for the MuCap experiment and NPL was provided by the National Science Foundation under grant #0855569, and CRDF. The analysis work was supported in part by the National Center for Supercomputing Applications under allocation TG-PHY060011N.

Table of Contents

Chapter 1

Introduction

The muon (μ) is a fundamental particle of the Standard Model of particle physics. As a charged lepton it interacts via the gravitational, electromagnetic and weak forces. It shares many properties with the other charged leptons, the electron (e) and tau (τ). These particles are spin 1/2 fermions and appear with either a positive or negative charge. A light, electrically neutral neutrino partners to each of the three lepton flavors, which are the ν_e, ν_μ and ν_τ, respectively.

The mass of the muon, $m_\mu \approx 105.7$ MeV/c^2, however, distinguishes it from the ≈207 times lighter electron, and ≈ 17 times heavier tau particle [1]. The mass of the muon notably enables its decay via the weak interaction:

$$\mu^+ \rightarrow e^+ + \nu_e + \bar{\nu}_\mu. \tag{1.1}$$

In this process a W^+ boson exchange mediates the decay of the muon into an electron and two neutrinos. The ≈ 2.2 µs lifetime of the muon makes it long lived compared to other particles that decay, and contributes to making it an experimentally accessible particle for physics measurements.

1.1 Muon Capture and Muon Kinetics

The weak force induces two characteristic phenomena of the negatively charged μ^- particle. The first is the dominant

$$\mu^- \rightarrow e^- + \bar{\nu}_e + \nu_\mu \tag{1.2}$$

decay mode of the μ^-. The decay rate of a free muon at rest, λ_μ, is related to the Fermi constant, G_F, as

$$\lambda_\mu = \frac{1}{\tau_\mu} = \frac{G_F^2 m_\mu^5}{192\pi^3}(1 + \Delta q), \tag{1.3}$$

where Δq accounts for QED, phase space and hadronic radiative corrections. Rare decay processes like

$$\mu^- \rightarrow e^- + \bar{\nu}_e + \nu_\mu + \gamma \tag{1.4}$$

and

$$\mu^- \rightarrow e^- + \bar{\nu}_e + \nu_\mu + e^+ + e^- \tag{1.5}$$

are taken into account in the full theoretical relation between λ_μ and G_F.

The Fermi constant quantifies the strength of the weak interaction. The recent measurement of the muon lifetime by the MuLan collaboration [2] determines the free muon decay rate to be $\lambda_\mu = 455170.2(5)$ s^{-1}. That result significantly improves the world knowledge of the Fermi constant, where $G_F = 1.1663787(6) \times 10^{-5}$ GeV^{-2}. The determination of the muon decay rate to 1 ppm relative precision is a foundation for the results of the MuCap experiment, which is the topic of this thesis.

The other characteristic phenomenon of the μ^- is muon capture, which is exemplified by capture onto the proton:

$$\mu^- + p \rightarrow n + \nu_\mu. \tag{1.6}$$

The underlying interaction in proton capture is diagrammed in Figure 1.1. The horizontal axis of this tree-level Feynman diagram is time, where the incoming μ^- and the three

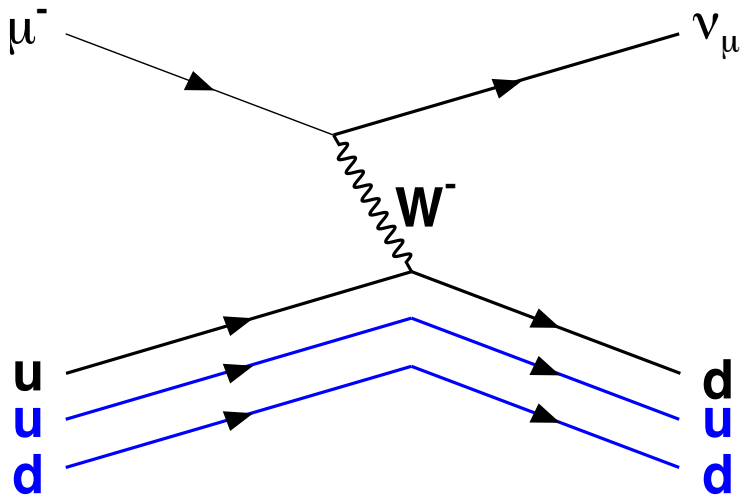

Figure 1.1: A tree-level Feynman diagram of muon capture on the proton (See Eq. 1.6). Time is represented on the horizontal axis of this diagram. The incoming proton and outgoing neutron are represented by their constituent quarks. The spectator quarks (blue) do not participate in the fundamental exchange of a W^- boson, but emphasize that this process is influenced by the strongly interacting QCD environment in which it takes place.

constituent quarks of the proton are depicted. The interaction proceeds via a W^- boson exchange between the μ^- and one of the constituent u quarks of the proton. The outgoing neutrino and neutron are depicted as the products of the interaction. The spectator quarks (blue) appear to indicate that this process is occurring in a strongly-interacting hadronic environment. This is a fundamental aspect of muon capture on the proton, and the source of interest in this process.

1.1.1 Muon Capture in the Standard Model

The capture process as described in Eq. 1.6 is called ordinary muon capture (OMC). Capture may proceed via

$$\mu^- + p \rightarrow n + \nu_\mu + \gamma, \tag{1.7}$$

which is referred to as radiative muon capture (RMC). For a muon in an atomic μp state, the OMC and RMC capture processes occur with $< 2 \times 10^{-3}$ and $< 10^{-8}$ probability, relative

to the dominant process of muon decay.

The kinematics of the ordinary muon capture process determine the momentum transfer of the interaction to be $q^2 = (q_n - q_p)^2 = -0.88m_\mu^2$ [3, 4]. The scale of this momentum transfer is small, meaning that this process can be well described as a point-like interaction. The transition amplitude of this process is quantified by a matrix element, M_C. The matrix element is expressed in terms of the Fermi constant G_F, as well as the leptonic, L_α, and hadronic, J^α, currents. The V_{ud} matrix element of the Cabibbo-Kobyashi-Maskawa (CKM) matrix appears to account for quark-flavor coupling. The matrix element M_C is expressed as

$$M_C = \frac{G_F V_{\text{ud}}}{\sqrt{2}} L_\alpha J^\alpha. \tag{1.8}$$

The characteristic "V-A" symmetry of the weak interaction appears in both the leptonic and hadronic currents, which are expressed as

$$L_\alpha = \bar{u}_\nu \gamma_\alpha (1 - \gamma_5) u_\mu,$$

and

$$J^\alpha = \bar{q}_d \gamma_\alpha (1 - \gamma_5) q_u,$$

respectively. The muon and neutrino fields are represented by u_μ and $\bar{u}_\nu$, respectively, and the up and down quark fields are represented by q_u and $\bar{q}_d$, respectively, in the above expressions.

As muon capture occurs in a hadronic environment, the interacting up and down quarks do not behave as free particles. The hadronic current, J^α, is modified to account for this reality. The hadronic current can be parameterized in terms of the form factors $g_V(q^2)$, $g_M(q^2)$, $g_A(q^2)$, $g_P(q^2)$, $g_S(q^2)$ and $g_T(q^2)$, where each is a function of the momentum transfer,

q^2. The hadronic current can be expressed in full generality[1] as

$$J^\alpha = \bar{q}_n \left(g_V \gamma^\alpha + \frac{i g_M}{2m_N} \sigma^{\alpha\beta} q_\beta + \frac{g_S}{m_\mu} q^\alpha - g_A \gamma^\alpha \gamma_5 - \frac{i g_T}{2m_N} \sigma^{\alpha\beta} q_\beta \gamma_5 - \frac{g_P}{m_\mu} q^\alpha \gamma_5 \right) q_p, \qquad (1.9)$$

where $\bar{q}_n$ and q_p represent the incoming and outgoing hadronic states. The first three terms represent the vector current, V^α, and the remaining the axial current A^α.

The general expression for J^α is reduced by symmetry arguments. The terms parameterized with $g_S(q^2)$ and $g_T(q^2)$ are called second-class currents, and vanish under the symmetry of G-parity, which is the product of charge conjugation and isospin rotation.

The conserved-vector-current (CVC) argument, which is a statement of weak charge conservation, relates the vector form factor $g_V(q^2)$ and the magnetic form factor $g_M(q^2)$ to the electromagnetic form factors of the proton. Results from electron scattering experiments determine the vector and magnetic form factors to be

$$g_V(-0.88 m_\mu^2) = 0.976(1)$$

and

$$g_M(-0.88 m_\mu^2) = 3.583(2),$$

respectively, where the use of $-0.88 m_\mu^2$ reflects that these values are specific for the momentum transfer relevant for muon capture.

The remaining axial-vector and pseudoscalar form factors, $g_A(q^2)$ and $g_P(q^2)$, respectively, are also determined experimentally. Neutron β-decay,

$$n \to p + e^- + \bar{\nu}_e, \qquad (1.10)$$

[1]This expression for the hadronic current J^α is the most general parameterization allowed that obeys Lorentz covariance symmetry. Any other terms would either violate that fundamental symmetry or be accounted for with the present parameterization.

is another charged-current weak process that can be utilized as a probe to determine these form factors. Experiments studying this process provide a precise determination of the axial-vector constant, $g_A(q^2 \approx 0) = 1.2695(29)$, which can be extrapolated to

$$g_A(-0.88m_\mu^2) = 1.247(2),$$

for the momentum transfer relevant for muon capture.

Nuclear β-decay experiments are insensitive to $g_P(q^2)$ because of the low momentum transfer of this process[2]. An experimental determination of $g_P(q^2)$ is therefore illusive in the context of β-decay, and leaves this coupling constant poorly understood experimentally. Muon capture on the proton is in contrast an experimentally practical probe to determine $g_P(q^2)$ [5].

Theory

Theoretical predictions for $g_P(q^2)$ are made from field theories [4]. The partially conserved axial current hypothesis (PCAC) relates $g_P(q^2)$ to the hadronic pion field $\pi(x)$ through the divergence of the axial current, where

$$\partial_\alpha A^\alpha \propto \pi(x)$$

As the pion is not not massless ($m_\pi \approx 139.6$ MeV/c^2), the PCAC condition relates the axial current coupling constant, g_A, to the pion field at $q^2 = 0$ [3–5]. The Goldberger-Treiman expression relates the axial vector constant $g_A(q^2 = 0)$ to the the weak coupling constant of the pion f_π, and the strong coupling constant of the pion in the nucleon $g_{\pi NN}$, where

$$g_A = \frac{f_\pi g_{\pi NN}}{m_N}, \tag{1.11}$$

[2]The insensitivity is also because direct neutrino detection is impractical.

and m_N is the nucleon mass[3]. An examination of the axial and vector current interaction further relates the divergence of A^α to $g_P(q^2)$ as

$$g_P(q^2) = \frac{2m_\mu m_N}{m_\pi^2 - q^2} g_A(q^2 = 0) \qquad \rightarrow \qquad g_P(-0.88m_\mu^2) = 8.59. \tag{1.12}$$

Chiral perturbation theory (χPT) provides additional theoretical tools for the determination of g_P. This effective field theory is a low energy expansion of QCD symmetries for the scale of the interaction momenta, q, that are small compared to the breaking scale of chiral symmetry, 1 GeV. Chiral perturbation in this context relates to the nucleon and pion fields. χPT reproduces the leading order result of PCAC shown in Eq. 1.12, but additionally provides for a systematic expansion to higher orders. The current χPT prediction [4–6] to next to leading order is

$$g_P^{\chi\mathrm{PT}}(-0.88m_\mu^2) = 8.26(23).$$

An experimental determination of the pseudoscalar coupling constant g_P is consequently a test of low energy QCD symmetries.

The Singlet Capture Rate

A measurement of the rate of capture from an atomic μp state is the experimental method for a determination of g_P. The rate of capture from the singlet μp state, Λ_S, can be determined with knowledge of the hadronic current, J^α, and the μp singlet (ground) state wavefunction, ψ_μ. The rate of muon capture depends on the spin state of the atomic system, but proceeds predominantly from the spin singlet state.

The singlet capture rate Λ_S is calculated by Czarnecki et al. [6] to be

$$\begin{aligned} \Lambda_\mathrm{S} &= |\psi_\mu(0)|^2 \frac{G_F^2 |V_\mathrm{ud}|^2}{2\pi} \frac{E_\nu^2}{M^2} (M - m_n)^2 \\ &\quad \cdot \left(\frac{2M - m_n}{M - m_n} g_V + \frac{2M - m_n}{M - m_n} g_A - \frac{g_P}{2} + (2(M + m_n) - 3m_\mu) \frac{g_M}{4m_N} \right)^2 \end{aligned} \tag{1.13}$$

[3]The nucleon mass is defined here as $m_N \equiv (1/2)(m_p + m_n)$

Here E_ν is the energy of the neutrino, $\psi_\mu(0)$ is the amplitude of the muon wavefunction at the origin, and M is the reduced mass of the μp system. The known values of the form factors and other parameters allow $\Lambda_{\rm S}$ to be expressed as a numerical function of $g_P(q^2)$. Relative to the χPT prediction, $g_P^{\chi{\rm PT}}$, the singlet capture rate is expressed as a function of a change in Δg_P where

$$\Lambda_{\rm S}(g_P^{\chi{\rm PT}} + \Delta g_P) = (692.3 \pm 3.4)(1 + \Delta r)(1 - 0.0108\Delta g_P)^2 \ {\rm s}^{-1}. \tag{1.14}$$

The electroweak radiative correction factor, $\Delta r = 0.028(4)$, is calculated in part from results of β-decay experiments. Eq. 1.14 analytically relates the pesudoscalar coupling constant g_P to the singlet capture rate $\Lambda_{\rm S}$. The theoretical prediction for the singlet capture rate from χPT is

$$\Lambda_{\rm S}^{\rm Theory} = \Lambda_{\rm S}(g_P^{\chi{\rm PT}}) = 711.5 \pm 3.4 \pm \ 2.8 \ {\rm s}^{-1},$$

where 3.4 and 2.8 $\rm s^{-1}$ represent the errors due to the uncertainty in $g_P^{\chi{\rm PT}}$ and the radiative correction Δr, respectively. An experimental measurement of $\Lambda_{\rm S}$ determines $g_P(-0.88m_\mu^2)$ by Eq. 1.14, where

$$g_P^{\rm Exp}(-0.88m_\mu^2) = g_P^{\chi{\rm PT}} + \Delta g_P.$$

Such a determination of $g_P(-0.88m_\mu^2)$ is the focus of the MuCap experiment discussed in this work, and the motivation of a 50-year long history of experimental efforts.

1.1.2 Muon Kinetics in Hydrogen

A muon (μ^-) entering a hydrogen filled volume undergoes a chain of fundamental particle interactions, as well as atomic and molecular processes, diagrammed in Figure 1.2. Muon decay and capture from the μp singlet state are two that were already presented. The density of a hydrogen target, ϕ, is a critical factor for many of these processes. The density is quoted relative to the density of liquid hydrogen, $\rho_{LH} = 3.5121 \times 10^4 \ \frac{\rm mol}{\rm m^3}$ [1]. The relevant densities

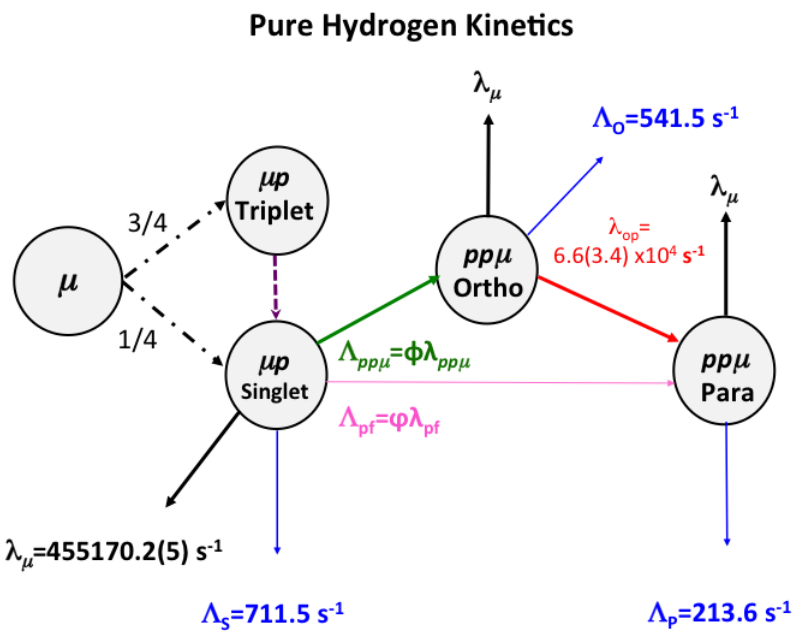

Figure 1.2: A diagram of the muon kinetics in a isotopically pure hydrogen (protium) gas, as presented in the text. On entering a hydrogen volume the muon quickly stops and rapidly populates the singlet and triplet μp states in a statistical ratio (dashed arrows) of three to one. Under thermal conditions the muon rapidly de-excites to the singlet state (purple arrow). From the μp state the muon will predominantly undergo decay with the rate λ_μ, but can capture onto the proton with the rate $\Lambda_{\rm S}$. Additionally, a $pp\mu$ molecular state can be formed with a rate $\Lambda_{pp\mu}$ (red), which transitions to a lower energy state with a rate $\lambda_{\rm op}$ (green), as will be presented in the text. The rate of direct para-molecular state formation, $\Lambda_{\rm pf}$ from the μp state is suppressed relative to the rate of ortho-molecular state formation, $\lambda_{pp\mu}$. The rate of capture on the proton (blue) is notably reduced from the molecular state.

of gaseous hydrogen targets are between 0.01 and 0.1.

As the muon slows in a hydrogen target via electromagnetic interactions, it enters an excited $n \approx 14$ principle quantum state of the μp atom. From that state the muon de-excites via a series of electromagnetic processes to more tightly bound (lower n) quantum states. Three processes exemplify the cascade physics [7, 8]: fast radiative transitions,

$$\mu p_n \rightarrow \mu p_{n'} + \gamma; \tag{1.15}$$

Coulombic de-excitation,

$$\mu p_n + \mathrm{H}_2 \rightarrow \mu p_{n'} + \mathrm{H}_2'; \tag{1.16}$$

and the external Auger process,

$$\mu p_n + \mathrm{H} \rightarrow \mu p_{n'} + p + e. \tag{1.17}$$

The muon arriving in the lowest energy states will populate the spin triplet state with a 3 to 1 statistical probability relative to the singlet state. The energy difference between these states (0.18 eV) causes thermalized μp atoms to de-excite from the triplet to singlet state through spin-flip ($(\mu p)_T + p \rightarrow (\mu p)_S + p$) interactions, and prevents spontaneous transitions from the singlet to the triplet state. In a hydrogen gas target at $\phi \geq 0.01$ this process proceeds irreversibly with a calculated rate of $2 \times 10^{10} \cdot \phi$ s^{-1} [4, 9]. The spin state of the muon at the end of the cascade process is of concern because the rate of capture from the triplet state, $\Lambda_{\mathrm{T}} \approx 12$ s^{-1} [9], is much slower than from the singlet state.

From the singlet μp state, weak decay proceeds with the rate $\lambda_\mu \approx 4.55 \times 10^5$ s^{-1} as the dominant disappearance mode for the muon. Muon capture proceeds from this same state with the rate $\Lambda_{\mathrm{S}} \approx 700$ s^{-1}. The singlet state μp atom may undergo a collisional interaction with a hydrogen molecule,

$$\mu p + \mathrm{H}_2 \rightarrow [(pp\mu)\ pe]^+ + e^-, \tag{1.18}$$

and form a $pp\mu$ molecular state. Typical hydrogen molecules, meaning those with only electrons orbiting hydrogen nuclei, have a complex spectrum of orbital angular momentum and rotational quantum states in thermal conditions. The $pp\mu$ state, in contrast, has only two orbital angular momentum states ($L = 1$ and 0) [5, 10, 11], with the energy splitting for the rotational states being larger than the thermal limit. This is a consequence of the $pp\mu$ molecular state being more tightly bound (and smaller in spatial extent) due to the larger mass of the muon. Molecular formation proceeds (predominantly) as an electric

dipole transition, where a conversion electron is emitted similar to an Auger interaction (See Eq. 1.17 [7, 8]). The formation of molecular states from the μp singlet state proceeds predominantly to the excited $L = 1$ state, referred to as the ortho-molecular state. Further details of this process will be discussed in Section 1.2.3.

The effective rate of molecular formation, $\Lambda_{pp\mu}$ (denoted by the red arrow in Figure 1.2), is density-dependent where

$$\Lambda_{pp\mu} = \phi \cdot \lambda_{pp\mu}. \tag{1.19}$$

Here $\lambda_{pp\mu}$ is the rate of molecular formation at liquid hydrogen density. The excited molecular state has a binding energy of 107.3 eV relative to the original $\mu p + H_2$ state [11]. The normalized rate of ortho-state molecular formation is theoretically predicted to be $1.80(9) \times 10^6$ s^{-1} [11].

The ortho-molecular state further evolves to the lower-energy $L = 0$ para-molecular state with a rate $\lambda_{\rm op}$, depicted in green in Figure 1.2. The para-molecular an additional energy loss of 145.9 eV relative to the ortho-molecular state, and has a total binding energy of 253.2 eV. The $\lambda_{\rm op}$ transition rate is experimentally determined [4] to be

$$\lambda_{\rm op} = 6.6(3.4) \times 10^4 \text{ s}^{-1}.$$

The uncertainty in this rate is dominated by two experimental results [12, 13] that are inconsistent at the level of 2.8 σ, leading to an inflated error for the average[4] of $\lambda_{\rm op}$. The processes of $pp\mu$ molecular formation and ortho- to para-molecular state transitions are both irreversible in a gaseous hydrogen environment because the binding energies of these states are larger than the thermal energy of $\approx 1/40$ eV at room temperature. The rate of para-state formation from the atomic μp state, $\lambda_{\rm pf}$, is suppressed relative to the formation of the ortho-molecular state by a factor of $\approx 3 \times 10^{-3}$, and is theoretically predicted to be $\lambda_{\rm pf} = 7.5 \times 10^3$ s^{-1} [11]. The effective rate of direct para-molecular state formation from the

[4]These experimental values for $\lambda_{\rm op}$ are llustrated in Figure 1.6.

μp singlet state, $\Lambda_{\rm pf}$, is expressed as

$$\Lambda_{\rm pf} = \phi \cdot \lambda_{\rm pf}, \tag{1.20}$$

in analogy to $\Lambda_{pp\mu}$.

The rate of OMC in the ortho-molecular state, $\Lambda_{\rm O}$ is expressed as

$$\Lambda_{\rm O} = 2\gamma_{om}(\frac{3}{4}\Lambda_{\rm S} + \frac{1}{4}\Lambda_{\rm T}), \tag{1.21}$$

where $2\gamma_{om}$ is a correction factor for the molecular state wavefunction of the muon, theoretically determined to be 1.009(1) [14]. The 3/4 and 1/4 symmetry of the singlet and triplet captures rates ($\Lambda_{\rm S}$ and $\Lambda_{\rm T}$, respectively) reflects the symmetry of the muon wavefunction in this state. The para-molecular state capture rate, $\Lambda_{\rm P}$, is

$$\Lambda_{\rm P} = 2\gamma_{pm}(\frac{1}{4}\Lambda_{\rm S} + \frac{3}{4}\Lambda_{\rm T}). \tag{1.22}$$

The para-molecular state correction factor, $2\gamma_{pm}$, is likewise determined [14] to be $2\gamma_{pm} = 1.143(1)$. The rates of muon capture from these states (blue in Figure 1.2) are thus determined to be

$$\Lambda_{\rm O} = 541.5 \text{ s}^{-1} \text{ and } \Lambda_{\rm P} = 213.6 \text{ s}^{-1}, \text{ respectively.}$$

It is worth emphasizing that ordinary muon decay still proceeds with the rate λ_μ in the molecular states as in the μp state[5], depicted in Figure 1.2.

The point of interest in the molecular states in any experimental measurement of $\Lambda_{\rm S}$ is that the rates of capture from these states are slower than in the singlet state, representing a systematic effect in the time spectrum of events. The effective disappearance rate of the muon due to capture on the proton may be interpreted as slower than it actually is.

[5]Apart from a 1 ppm-level change in the rate of muon decay in the μp atomic and $pp\mu$ molecular states due to phase space suppression. Such effects will be discussed in grater detail in Section 4.1.2.

Knowledge of the population of molecular states is hence crucial to correctly extract Λ_S.

1.1.3 Experimental History of Muon Capture

Early experiments to measure the singlet capture rate used liquid hydrogen targets. The time spectrum of decay electrons or capture neutrons was used to determine the muon disappearance rate from the μp state, and subsequently determine the singlet capture rate Λ_S. Liquid hydrogen is favorable because it efficiently stops muons in the target volume away from walls of heavier ($Z > 1$) elements. This is desirable because the muon disappears via capture in such materials with rates as much as 5 orders of magnitude faster than Λ_S, inducing a potential systematic effect in the time spectrum of events. In a liquid hydrogen target molecular formation proceeds at a rate which is $\approx$4 times faster than the muon decay rate λ_μ. This qualitatively illustrates how significant the populations of the $pp\mu$ molecular states are on the time scale of the muon lifetime, and how significantly they affect the time spectrum of decay and capture events in liquid hydrogen conditions.

The probability of the muon being in either the μp singlet state, $n_{\mu p}(t)$, ortho-molecular state, $n_{\mathrm{Ortho}}(t)$ or para-molecular state $n_{\mathrm{Para}}(t)$ is shown in Figure 1.3(a) for liquid hydrogen conditions. The horizontal axis represents the time t relative to the stopping of a muon and the formation of a μp state atom. Within one 2.2 µs lifetime the likelihood of the muon being in the ortho-molecular state is an order of magnitude larger than for it to be in the atomic state that it initially formed after stopping in hydrogen.

Figure 1.3(b) shows the analogous plot for the condition of the MuCap experiment using a 10 bar hydrogen gas. The population of both the ortho- and para-molecular states remain suppressed relative to the dominant μp state. This condition maximizes the fraction of observed events representing capture from the singlet μp state, which minimizes the systematic error due to the uncertainty of the muon chemistry of the $pp\mu$ molecular states. While the hydrogen density could be further minimized relative to a 10 bar gas, a lower density reduces

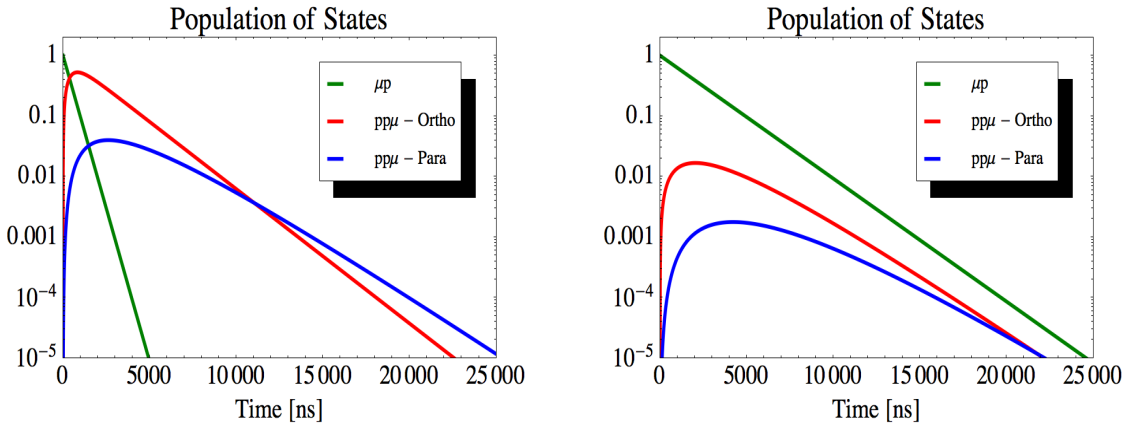

(a) Liquid Hydrogen ($\phi = 1.0$)

(b) Gaseous Hydrogen ($\phi = 0.1$)

Figure 1.3: Time dependence of the population of kinetic states for the stopped muon in pure hydrogen under the liquid hydrogen ($\phi = 1.0$) density condition, and the nominal MuCap condition of gaseous hydrogen at 10 bar pressure ($\phi = 0.01$). The gaseous target condition minimizes the formation of the $pp\mu$ molecular states and consequently the systematic effect of the reduced rate of muon capture on the proton from these states on the observed muon disappearance rate in hydrogen.

the stopping power of the target[6]. Experimental determination of the muon stop location is critical information in a gaseous target condition, for the rejection of events where the μ^- may have interacted with materials other than hydrogen. The MuCap experiment implements a novel hydrogen time projection chamber target detector for this purpose, which will be presented in Chapter 2.

1.1.4 The MuCap Experiment

The MuCap experiment measures the singlet capture rate Λ_S with a lifetime method. The lifetime of the μ^- in a pure hydrogen gas is perturbed from the free muon decay rate, λ_μ, by $\approx \Lambda_S$. A measurement of the μ^- decay rate in hydrogen, λ_-, allows a comparison to the positive muon lifetime in hydrogen[7], λ_+ ($\approx \lambda_\mu$), and a determination of the singlet capture rate where

$$\Lambda_S \approx \lambda_- - \lambda_+.$$

[6]It will be mentioned later that the observed fraction of muons which stop in the 10 bar target gas is $\approx 50\%$

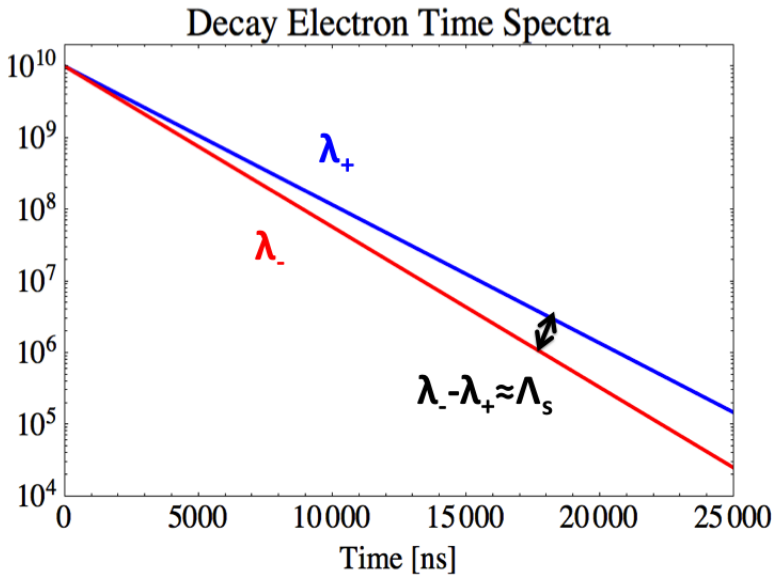

Figure 1.4: The above plot is a representation of the lifetime measurement method used by the MuCap experiment. A measurement of the effective disappearance rate of the μ^- in hydrogen, λ_- can be compared to the μ^+ or free muon decay rate to determine the singlet capture rate Λ_S. Note: The rate of Λ_S has been artificially increased by a factor of 10^2 to produce this illustrative plot.

The method is qualitatively illustrated in Figure 1.4. Because the μ^+, or free muon, decay rate is experimentally determined to 1 ppm relative precision [2], the determination of Λ_S with this method can be done precisely.

The first result of the MuCap experiment [15] leads to a determination of Λ_S to be

$$\Lambda_S = 725.0(17.4)\ \mathrm{s}^{-1}.$$

This result was obtained with a data set with 10^8 muon decays, which determined the λ_- disappearance rate in hydrogen to be $\lambda_- = 455851.4 \pm (12.5)_{\mathrm{stat}} \pm (8.5)_{\mathrm{sys}}\ \mathrm{s}^{-1}$. The pseudoscalar coupling constant is subsequently determined to be $g_P(-0.88m_\mu^2) = 7.3(1.1)$, which is currently the most precise experimental determination of $g_P(-0.88m_\mu^2)$. This and the previous determinations of $g_P(-0.88m_{\mu^2})$ are summarized in Figure 1.5.

The design of the MuCap experiment minimizes the formation of $pp\mu$ molecular states,

[7]Here the positive muon lifetime in hydrogen, λ_+, is not explicitly the same as the free muon decay rate. It is reduced at a level of 1 ppm due to phase space suppression effects in the bound μp state. This represents a small correction to the results of the MuCap experiment.

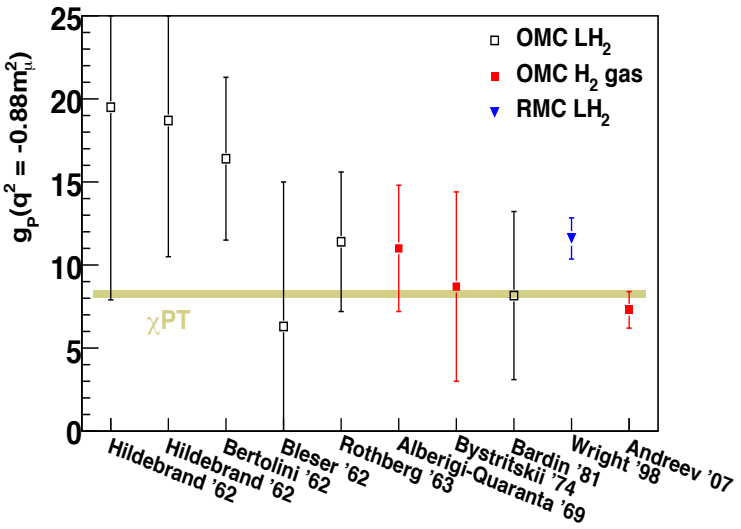

Figure 1.5: A summary plot of previous experimental efforts to determine $g_P(-0.88m_\mu^2)$. The information presented here reflects the current knowledge of the form factors as summarized in Eq. 1.14. The experiments are broken into two main categories; those that study OMC in liquid (black) or gaseous (red) hydrogen targets. One experiment (blue) studied RMC using a liquid state target. The first MuCap result (Andreev et al. '07 [15]), is the most precise to date. Lastly, the current status of the χPT prediction of $g_P(-0.88m_\mu^2)$ is shown (gold). Reproduced from the recent review of muon capture on the proton [4].

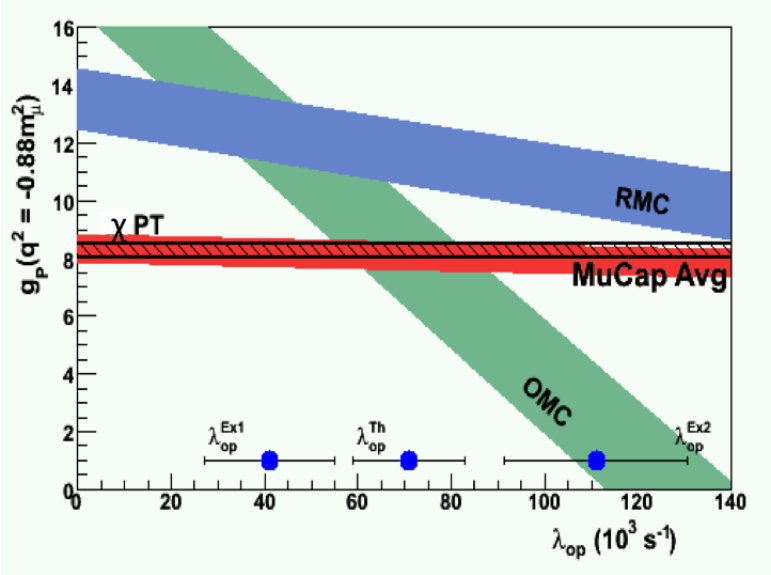

Figure 1.6: An illustration of the sensitivity of recent experiments to determine g_P on knowledge of the the ortho-para molecular state transition rate, $\lambda_{\rm op}$. The result of Wright et al. [16], extracted from measuring the rate of RMC in liquid hydrogen, is shown as it depends on the molecular transition rate $\lambda_{\rm op}$. Also shown is the result of Bardin et al. [17], obtained from measuring the rate of OMC in liquid hydrogen. The result of the Mucap experiment (red) is in contrast less sensitive to molecular effects because of the choice of a 10 bar hydrogen gas target. The prediction of χPT is shown in black. The present experimental and theoretical knowledge of $\lambda_{\rm op}$ is summarized at the bottom of the plot, as reported in references [12–14], respectively.

making the result of this experiment unambiguously interpretable compared to previous measurements. The effect of the molecular kinetics on the interpretability of the previous results is summarized in Figure 1.6. Here the most recent RMC [16] and OMC [17] results are presented as correlated to the $\lambda_{\rm op}$ transition rate of the molecular state. The values at the bottom of the plot represent two experimental values and a theoretical prediction for the transition rate. What is clearly illustrated here is that the interpretation of $g_p(-0.88m_{\mu^2})$ from these measurements requires knowledge of the molecular kinetics. The MuCap result in contrast is relatively insensitive to $\lambda_{\rm op}$, and the extraction of the singlet capture rate $\Lambda_{\rm S}$ is more precise and unambiguous. The prediction of χPT (black) is shown for comparison.

The effect of the $pp\mu$ molecular state kinetics in the hydrogen gas is accounted for with

a systematic correction, $\Delta_{pp\mu}$ where

$$\lambda_- - \lambda_+ = \Lambda_{\rm S} - \Delta_{pp\mu}. \tag{1.23}$$

The correction $\Delta_{pp\mu}$ is in approximation[8] expressed as

$$\begin{aligned}
\Delta_{pp\mu} &\approx (2-3\gamma_{om})\frac{\Lambda_{pp\mu}}{\lambda_\mu}\Lambda_{\rm S} + \frac{3}{2}(3\gamma_{om}-\gamma_{pm})\frac{\Lambda_{pp\mu}}{\lambda_\mu}\frac{\lambda_{\rm op}}{\lambda_\mu}\Lambda_{\rm S} && (1.24)\\
&\pm (2-3\gamma_{om})\frac{\Lambda_{\rm S}}{\lambda_\mu}\Delta\Lambda_{pp\mu} && (1.25)\\
&\pm \frac{3}{2}(3\gamma_{om}-\gamma_{pm})\frac{\Lambda_{pp\mu}}{\lambda_\mu}\frac{\Lambda_{\rm S}}{\lambda_\mu}\Delta\lambda_{\rm op}. && (1.26)
\end{aligned}$$

Here $\Delta\Lambda_{pp\mu}$ and $\Delta\lambda_{\rm op}$ represent the known uncertainties in the rates of molecular formation and the ortho-to-para state transition, respectively.

For the first result of the MuCap experiment this correction was determined to be $\Delta_{pp\mu} = 23.5 \pm (4.3)_{\Lambda_{pp\mu}} \pm (3.9)_{\lambda_{\rm op}}$ s^{-1}. This approximation motivates how knowledge of the molecular kinetics must be used in the extraction of the singlet capture rate. Although the MuCap experiment minimizes the sensitivity to the molecular kinetics in the decay electron time spectrum, it is a critical correction to this result. The first result assumed a conservative value of $\lambda_{pp\mu} = 2.3(5)\times 10^6$ s^{-1}, which dominated the systematic uncertainty associated with the effective rate of molecular formation, where $\Lambda_{pp\mu} = \phi \cdot \lambda_{pp\mu}$. That value represents the experimental world average of $\lambda_{pp\mu}$ under liquid and gaseous hydrogen conditions. The assumed value for the ortho-para transition rate was $\lambda_{\rm op} = 6.9(4.3) \times 10^6$ s^{-1}, which is

[8]This expression derives from the approximation that the average muon disappearance rate, λ_-, can be expressed analytically as

$$\lambda_- \approx \frac{\int_0^\infty n_e^{\rm H}(t)dt}{\int_0^\infty t\cdot n_e^{\rm H}(t)dt},$$

where $n_e^{\rm H}(t)$ is the time spectrum of decay electrons in the pure hydrogen gas. The time distribution is expressed as a function of λ_μ, $\Lambda_{\rm S}$, $\Lambda_{pp\mu}$, γ_{om}, $\lambda_{\rm op}$ and γ_{op} and the disappearance rate can be expressed to first order in $\Lambda_{\rm S}$, $\lambda_{\rm op}$ and $\Lambda_{pp\mu}$ in a Taylor series approximation. This obtains a leading order approximation of the molecular state correction, $\Delta_{pp\mu}$. In full, however, the average disappearance rate is sensitive to the time range of the fit applied to the pure hydrogen data and other effects to be presented later. The full correction is determined from simulation that takes these effects into account.

different than the updated average of $\lambda_{\rm op} = 6.6(3.4) \times 10^4$ s^{-1} [4] which is used in this present work.

While the choice of a gaseous target condition minimizes the rate of molecular formation, knowledge of $\Lambda_{pp\mu}$ is required to correctly extract $\Lambda_{\rm S}$, and more so than under liquid hydrogen conditions. In liquid hydrogen the population of the ortho-molecular state dominates the population of the μp state after ≈ 2.2 µs. The dominant kinetic state of capture events is the ortho-molecular state in such target conditions. The transition rate to the para-molecular state, $\lambda_{\rm op}$ is more crucial to correctly interpreting results under these conditions than the molecular formation rate, $\Lambda_{pp\mu}$. This is illustrated in Figures 1.3(a) and 1.6.

A new data set from the MuCap experiment with 10^{10} decay events now determines λ_- with a statistical uncertainty of ≈ 5 s^{-1} and a systematic error of ≈ 5 s^{-1}. Without improved knowledge of the molecular formation rate, $\lambda_{pp\mu}$, this single systematic error is of comparable magnitude to the statistical and systematic errors of the new result. The uncertainties of the kinetic rates, $\Lambda_{pp\mu}$ and $\lambda_{\rm op}$, produce errors that are significant in magnitude relative to the improved statistical precision of $\Lambda_{\rm S}$, and the subsequent determination of $g_P(-0.88m_\mu^2)$. An improved experimental determination of $\Lambda_{pp\mu}$ from the same conditions of the MuCap experiment is highly motivated. To constrain the systematic error associated with the molecular formation rate to 2 s^{-1} or smaller, the effective molecular formation rate $\Lambda_{pp\mu}$ would have to be known to 10% or better relative precision. It will be shown that a special data set taken with an argon-doped target gas provides for a measurement of $\Lambda_{pp\mu}$ to $\approx 3\%$ relative precision, which surpasses this benchmark.

1.2 Muon Induced Processes and $pp\mu$ Formation

1.2.1 Muon Chemistry With $Z > 1$ Atoms

Muon Transfer From the μp Singlet State

When $Z > 1$ elements are present in a hydrogen gas two additional processes involving the muon can proceed. The first is that a muon can transfer from the μp singlet state to form a new μZ atomic state with the nucleus of the heavier atom. In such an atom the muon is bound in an increasingly smaller orbit, where the orbital radius scales inversely with the increasing charge of the nucleus. Once in a μZ bound state the muon can undergo ordinary decay, or capture onto the nucleus of the atom. The neutral μp atom is $m_\mu/m_e \approx 200$ times smaller than the typical hydrogen atom, with a Bohr radius that is m_μ/m_e times smaller.

The process of muon transfer to a heavier element from the singlet μp state,

$$\mu p + Z \rightarrow \mu Z + p, \tag{1.27}$$

results in the muon arriving in the excited ($n \leq Z - 1$) principle quantum states of the newly formed μZ atom. As with the μp cascade process, the muon is driven quickly to the ground state, which is dominated by radiative transitions in the heavier μZ systems. Auger electrons and X-rays produced with radiative de-excitations of the muon are characteristically emitted, providing a prompt signal of transfer to a heavier element [10]. Such X-rays typically correspond to the K line transitions of the μZ atom, which are characteristically on the scale of MeV to keV for most muonic atoms.

Muon transfer is a collisional process with a density-dependent rate, similar to molecular formation. The effective rate of transfer of the muon to an element Z, Λ_{pZ}, is expressed as

$$\Lambda_{pZ} = c_Z \cdot \phi \cdot \lambda_{pZ}, \tag{1.28}$$

where ϕ is the hydrogen density, c_z is the relative atomic concentration of the element, and λ_{pZ} is a characteristic rate of transfer for that element. The neutral and small μp atom can get close enough to the Z nucleus that a significant wavefunction overlap is possible. The characteristic rate of transfer typically scales as Z^2, because the amplitude of the wavefunction overlap scales with this factor [10].

Muon Capture From a μZ State

The capture of the muon from a μZ state,

$$\begin{aligned} \mu^- + Z &\rightarrow (Z-1)^* + \nu_\mu \\ &\hookrightarrow Z' + n, \end{aligned} \tag{1.29}$$

proceeds with a rate Λ_Z that is characteristic of that element. Muon capture rates from such states scales as Z_{eff}^4, where Z_{eff} is the effective charge of the nucleus. This can be separated into several sources, the first being that the heavy atom contains Z protons which increases the rate of capture. The muon orbital radius is smaller in this state because of the reduced mass and increased charge of the nucleus of the μZ atom. The singlet state orbital wavefunction of the muon overlaps at the origin with an amplitude that is $\approx Z_{eff}^3$ greater than in the μp state.

The capture rate of the muon from a μZ state is expressed as [18]

$$\Lambda_Z(A,Z) = Z_{eff}^4 x_1 \left(1 - x_2 \frac{A-Z}{2A}\right), \tag{1.30}$$

where Z and A describe the isotopic state of the atom. The variable x_1 represents the capture rate in hydrogen as reduced by the available neutrino phase space in the capture onto a heavy nucleus[9]. The variable x_2 accounts for the Pauli exclusion principle in the

[9]This is to say that it represents the base rate of capture onto a proton, but in a nuclear state. This rate is not the same as the Λ_S rate of interest in the MuCap experiment, and is phase space suppressed.

nuclear environment, associated with the size of the nucleus.

In capture onto $Z > 1$ nuclei a $(Z-1)$ product nucleus remains, identified in Eq. 1.29. This nucleus can be left in an excited state following capture and typically emits a neutron as depicted, which is the dominant de-excitation mode in capture onto argon. The remnant nucleus may also emit a charged particle (a proton or alpha particle) in the de-excitation process. This means the capture process may appear as

$$\begin{aligned} \mu^- + Z \quad &\rightarrow \quad (Z-1)^* + \nu_\mu \\ &\hookrightarrow Z' + n + X \end{aligned} \tag{1.31}$$

where X is the emitted charged particle. This process occurs for $\approx 5\%$ of capture events onto medium mass nuclei (meaning elements where Z is between 10 and 30). A similar fraction of capture events result in multiple neutrons being emitted from the product nucleus, which is another de-excitation mode of the excited nucleus.

The neutrons produced in the μZ capture process are an experimental observable for the study of muon kinetics. One final observation to make is that while capture onto the proton produces monoenergetic 5.2 MeV neutrons, capture onto heavier elements produces neutrons with a distribution of energies. The complexity of the nuclear environment makes this a difficult feature of the capture process to describe theoretically.

1.2.2 Determinations of the $\lambda_{pp\mu}$ Molecular Formation Rate

The current world knowledge of the molecular formation rate, $\lambda_{pp\mu}$, is based on several measurements [19–22] that represent a large variation of results and methods. Much of the experimental history surrounding the molecular formation arose out of interest in muon catalyzed fusion processes such as

$$pd\mu \rightarrow {}^3\mathrm{He}\mu + \gamma, \tag{1.32}$$

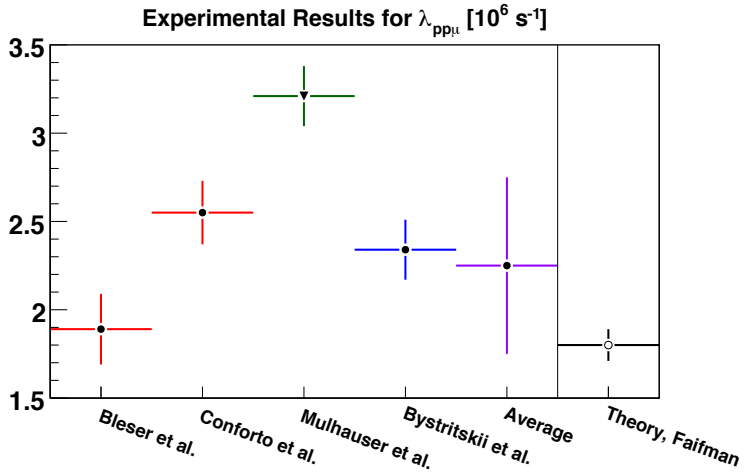

Figure 1.7: The plot above reports the four most precise experimental determinations of the molecular formation rate, $\lambda_{pp\mu}$. Two experiments made under liquid hydrogen target conditions [19, 20] (red) produce results that agree at the level of 2.5 σ. The only previous gaseous hydrogen target result (blue) is provided by Bystritskii et al. [21]. Additionally, a fourth result is determined from experiments utilizing a solid hydrogen target (red) [22]. The current $1.80(9)\times10^6$ s^{-1} theoretical prediction [11], and the average ($2.3(5) \times 10^6$ s^{-1}) of the liquid and gaseous target results (black) are shown.

where a 5.4 MeV gamma ray is a unique signature of this process. Early efforts utilized hydrogen targets with varying concentrations of deuterium and tritium to determine the kinetics of the muon in such conditions. Figure 1.7 reports the quantitative comparison of these results and the current status of theory and the average of the liquid and gaseous state target results. This average was used to assess the molecular state systematic correction for the first MuCap result [15].

Two early results for the molecular formation rate, $\lambda_{pp\mu}$, $2.55(18) \times 10^6$ s^{-1} [20] and $1.89(20) \times 10^6$ s^{-1} [19], were obtained under liquid hydrogen conditions. These reports show consistency at the level of 2.5 σ. Both experiments relied on analysis of the time spectrum of fusion gamma rays to determine the disappearance rate of the μ^- after stopping in the target, and subsequently $\lambda_{pp\mu}$.

Bystritskii et al. [21] report a result, $2.34(17) \times 10^6$ s^{-1}, that is within the range of variation of the liquid hydrogen results. It is currently the only reported result obtained under gaseous hydrogen conditions. This experiment utilized a hydrogen gas doped with

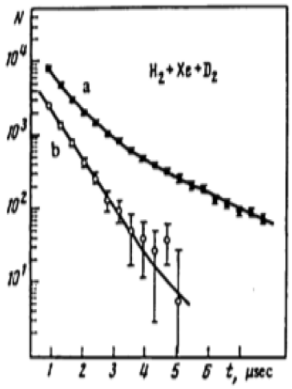

FIG. 8. Time spectra of events recorded by the e detectors in run III (the normalized background has been subtracted): a—coincidences with counter 5 ($e+5$), b—anticoincidences with counter 5 ($e-5$); the solid lines are theoretical curves.

(a) Decay electron time spectrum

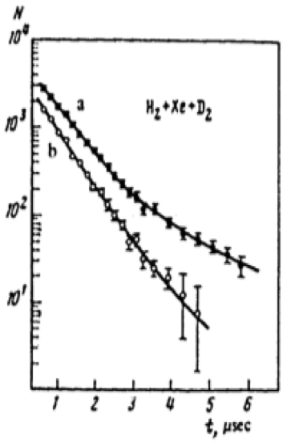

FIG. 9. Time spectra of events recorded by the γ detectors in run III (the normalized background has been subtracted): a—coincidences with counter 5 (γ+5), b—anticoincidences with counter 5 (γ−5).

(b) Fusion gamma ray time spectrum

Figure 1.8: The figures here represent the decay electron (left) and gamma ray time spectra observed in the experiment of Bystritskii et al. [21].

up to 30 ppm of xenon and 7% of deuterium at 40 bar pressure. Like the liquid target experiments, this effort utilized the time spectrum of gamma rays, but also that of decay electrons, to determine the molecular formation rate. In this experiment the gamma ray spectrum is predominantly associated with the 3.8 MeV K_α line of the μXe atom, which is a signature of transfer from hydrogen to the μXe state. Figure 1.8 reproduces the time spectra for decay electrons and fusion gamma rays from this experiment [21].

The most recent experimental result, utilizing a solid hydrogen target, determines a value for $\lambda_{pp\mu} = 3.21(18) \times 10^6$ s^{-1} that is inconsistent with the average of the results obtained by the liquid and gaseous hydrogen target experiments ($2.3(5) \times 10^6$ s^{-1}) by 1.5 σ, and differs from the result of Bystritskii et al. by 3 σ. That experiment utilized the time spectra of fusion neutrons and alpha particles from a special deuterium and tritium enriched target to determine the molecular formation rate. The initial MuCap result utilized the average of the results of liquid and gaseous target experiments in part because of concerns for additional systematic effects in the solid state that may explain the deviation of that result from those

obtained under liquid or gaseous conditions.

The present status of experimental knowledge of $\lambda_{pp\mu}$ is a source of difficulty for the precise interpretation of the final MuCap result in part because of the varying target conditions and methods applied in these efforts. Furthermore, the MuCap experiment utilizes an isotopically pure protium gas stopping target.

1.2.3 Theoretical Description of Molecular Formation

The adiabatic limit (the Bohr-Oppenheimer approximation) is useful for the case of an electron in orbit around a proton, and has been used to describe many atomic and molecular processes in hydrogen. Because the muon mass is sufficiently large relative to the proton mass, and the orbital radius of the muon is characteristically $\approx m_\mu/m_e$ times smaller, the theoretical interpretation of this process requires a description of the three-body dynamics of the $pp\mu$ molecule. Early theoretical efforts applied variational methods and expansions in the relative mass of the muon and proton to determine the wavefunction of the molecular state [10,23,24] as necessary to calculate the rate of formation and other processes associated with the $pp\mu$ state [10, 13]. The most recent theoretical efforts apply an adiabatic representation to the three-body $pp\mu$ system [11].

The molecular formation process is interpreted as an electric dipole or monopole transition [10], induced by a collision of a μp atom in the singlet state and a hydrogen molecule H_2, as expressed in Eq 1.18. The initial relative orbital angular momentum, L_i of the $\mu p + \mathrm{H}_2$ state is dominated by the S-wave ($L_i = 0$) component of the relative motion of the atom and molecule. The quantum selection rules for dipole and monopole transitions can be related [10, 11, 25] to the formation of the $pp\mu$ molecular states from the μp singlet state. The allowed ($\Delta L = 1$) dipole transition to the $L_f = 1$ quantum state, the excited ortho-molecular state, is the dominant mechanism of molecular formation.

The electric monopole transition to the $L_f = 0$ para-molecular state is suppressed relative to the dipole transition. While suppressed, the monopole ($\Delta L = 0$) transition to the para-

molecular state is allowed and the total rate of direct para-molecular state formation is predicted to be $\lambda_{\rm pf} = 7.5 \times 10^3$ s^{-1}.

The initial state of the collisional orbital angular momentum does include $L_i = 1$ and higher components, but they are suppressed because of the small size of the μp atom and the low-energy (momenta) of thermal collisions. Table 1.1 summarizes the calculation of the molecular formation rate obtained from Faifman [11]. The magnitude of the rates follow the pattern described by the quantum selection rules discussed above. The current status of the theoretical prediction of

$$\lambda_{pp\mu}^{Theory} = 1.80(9) \times 10^6 \text{ s}^{-1}$$

is lower than the current experimental average. A more precise experimental determination is hence a test of our present theoretical understanding of this process.

Table 1.1: Table of rates for the collisional formation of $pp\mu$ molecular states from the μp singlet state. The results below are quoted from Faifman, et all [11], and are calculated for a collisional energy of $\epsilon = 0.04$ eV. These calculations are assumed to have a $\approx 5\%$ error [11, 24].

Table of Molecular Formation Processes			
L_i	L_f, final state	Type of Transition	Rate [10^6 s^{-1}]
0	0, para	monopole	7.42×10^{-3}
0	1, ortho	dipole	1.8
1	1, ortho	monopole	1.08×10^{-5}
1	0, para	dipole	9.48×10^{-5}
2	1, ortho	dipole	3.03×10^{-6}

1.3 Goal and Method of Present Experiment

In order to determine the systematic error due to the molecular formation rate to better than 2 s^{-1} for the final result of the MuCap experiment, a measurement to determine $\lambda_{pp\mu}$ to at least 10% relative precision is required. The present work achieves this with the use of an argon-doped hydrogen target gas under the identical conditions as the pure hydrogen

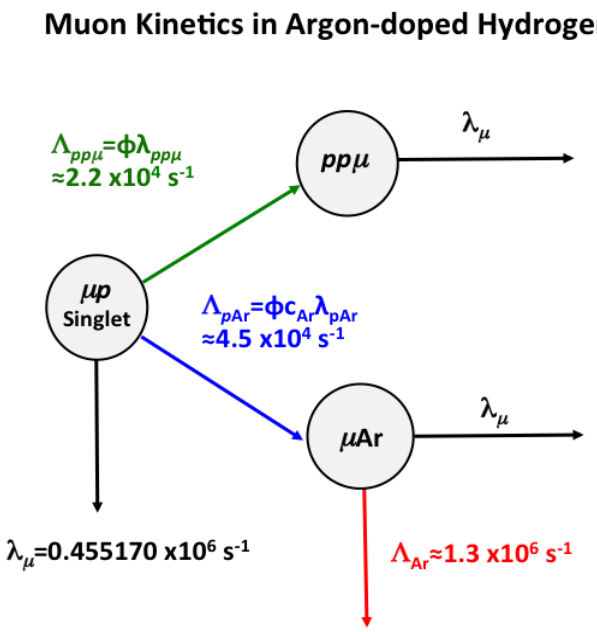

Figure 1.9: Diagram summarizing the kinetics of a muon stopped in a hydrogen gas doped with $\approx$ 20 ppm (atomic) of argon. Two of the kinetic states in an argon-doped protium gas are the μp and μAr atomic states. The $pp\mu$ ortho- and para-molecular states can be approximated as a single state with a lifetime very similar to the muon lifetime. This model is useful for illustration. Extensions to this model will be discussed in Chapter 4.

measurement. This provides an unambiguous determination of the molecular formation rate under the same conditions as the Λ_S measurement for the final MuCap result.

The time spectra of both decay electrons and capture neutrons each provide information in this experiment. The motivation for using argon has to do with the characteristics of the muon kinetics associated with this element, shown in Figure 1.9. The specific characteristics of interest for the present experiment are the transfer and capture rates, $\lambda_{p\mathrm{Ar}}$ and Λ_{Ar}, respectively. As a noble gas argon is an experimentally practical dopant for a hydrogen gas and has been used in a history of experiments going back to the 1960's [26, 27].

1.3.1 Muon Kinetics In An Argon-doped Hydrogen Gas

The mass and charge of an argon nucleus is such that the effective muon transfer rate $\Lambda_{p\mathrm{Ar}}$ from the μp state with $\approx$ 20 ppm (atomic) of argon in an isotopically pure protium gas

changes the disappearance rate of the μp state by $\approx 10\%$. The capture rate, $\Lambda_{\rm Ar}$, is $\approx$3 times larger than the muon decay rate λ_μ. Nearly $\approx 10\%$ of muons stopping in the argon-doped gas will enter the μAr state and undergo decay for capture with a total disappearance rate ≈ 4 times faster than the muon decay rate. The $pp\mu$ molecular states are approximated as a single state with a disappearance rate that is the muon lifetime, and the effective formation rate of $\Lambda_{pp\mu}$.

A ≈ 20 ppm concentration of argon perturbs the muon kinetics such that a single lifetime approximation is insufficient to describe the decay electron time spectrum. The electron time spectrum is dominated by the three distinct and statistically resolvable disappearance rates of the three dominant kinetic states

$$r_{\mu p} \approx \lambda_\mu + \Lambda_{pp\mu} + \Lambda_{p\rm Ar} \tag{1.33}$$

$$r_{\mu\rm Ar} \approx \lambda_\mu + \Lambda_{\rm Ar}, \tag{1.34}$$

$$\text{and } r_{pp\mu} \approx \lambda_\mu. \tag{1.35}$$

The contributions of muon decay events from each of these states are determined by non-linear expressions of the kinetic rates λ_μ, $\Lambda_{pp\mu}$, $\Lambda_{p\rm Ar}$ and $\Lambda_{\rm Ar}$. In this limit the time spectrum of the decay electrons, $n_e(t)$ is approximated as

$$n_e(t) = C_{\mu p} e^{-r_{\mu p} t} + C_{\mu\rm Ar} e^{-r_{\mu\rm Ar} t} + C_{pp\mu} e^{-r_{pp\mu} t}, \tag{1.36}$$

where the coefficients $C_{\mu p}$, $C_{\mu\rm Ar}$ and $C_{pp\mu}$ are expressed as

$$C_{\mu p} = \frac{\Lambda_{p\rm Ar} \cdot \Lambda_{\rm Ar}}{\Lambda_{\rm Ar} - \Lambda_{pp\mu} - \Lambda_{p\rm Ar}} \tag{1.37}$$

$$C_{pp\mu} = \frac{\Lambda_{pp\mu}}{\Lambda_{pp\mu} + \Lambda_{p\rm Ar}} \tag{1.38}$$

$$\text{and } C_{\mu\rm Ar} = \frac{-\Lambda_{p\rm Ar}}{\Lambda_{\rm Ar} - \Lambda_{pp\mu}}. \tag{1.39}$$

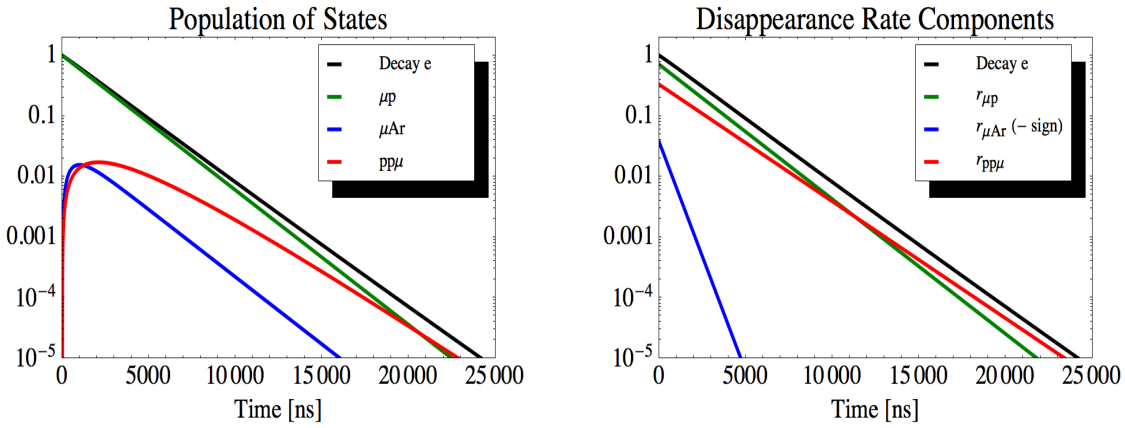

(a) (b)

Figure 1.10: Left:Time dependence of the population of the kinetic states for the stopped muon in a ≈20 ppm (atomic) argon-doped hydrogen gas at 10 bar pressure. Right: The electron time spectrum (black)

Figure 1.10(b) illustrates the decay electron time spectrum in an argon-doped gas as broken down into the individual exponential components. The contribution of the μAr state disappearance rate was multiplied by -1 for easier presentation. The above equations illustrate the non-linear and correlated relationship between the dominant λ_μ, $\Lambda_{pp\mu}$, $\Lambda_{p\mathrm{Ar}}$ and Λ_{Ar} kinetic rates that determine the time spectrum of decay and capture events. Extensions to this approximate model of the muon kinetics in an argon-doped hydrogen are presented in Chapter 4.

1.3.2 Experimental History of the Argon Transfer and Capture Rates

The experimental history of the transfer and capture rates of argon is summarized in Table 1.2, with the reported values and associated references indicated for each result. Experimental efforts to measure the transfer rate typically used hydrogen gas targets at varying pressures and concentrations of argon. The transfer rate, $\lambda_{p\mathrm{Ar}}$ is in part difficult to measure

because it requires an extraction of $\lambda_{p\mathrm{Ar}}$ from the effective transfer rate $\Lambda_{p\mathrm{Ar}}$, where

$$\Lambda_{p\mathrm{Ar}} = \phi \cdot \mathrm{c_{Ar}} \cdot \lambda_{\mathrm{pAr}}. \tag{1.40}$$

Knowledge of the atomic concentration of argon, $\mathrm{c_{Ar}}$, and the gas density are just one systematic limitation to determining $\lambda_{p\mathrm{Ar}}$. The effective rate of the transfer process changes with conditions and other systematic effects can appear. This is illustrated by a history of measurements that have a wide range of variation between 1 and 10 in units of $\times 10^{11}$ s^{-1}. Most of these were made prior to 1990. The most recent effort [28] obtains precision result from an analysis of the gamma ray time spectrum of the K line transitions of the μAr atom, $1.63(9) \times 10^{11}$ s^{-1}. That work indicates the presence of thermalization and excited state transfer effects, which are sensitive to target conditions like temperature and density. The current experimental status of the argon transfer rate is therefore inconclusive, and the value for $\lambda_{p\mathrm{Ar}}$ is not well known. Reported results for the Λ_{Ar} capture rate [29–31] exhibit variation, but at a less significant scale.

Table 1.2: Table of reported experimental determinations of the argon transfer, $\lambda_{p\mathrm{Ar}}$, and capture, Λ_{Ar} rates. Note: The results reported for the transfer rate $\lambda_{p\mathrm{Ar}}$ are compiled in part from reference [27].

Experimental Determinations of $\lambda_{p\mathrm{Ar}}$ and Λ_{Ar}.			
$\lambda_{p\mathrm{Ar}}$ [$\times 10^{11}$ s^{-1}]		Λ_{Ar} [$\times 10^{6}$ s^{-1}]	
Result	Reference	Result	Reference
1.42(16)	[32]	1.31(1)	[29]
1.46(5)	[32]	1.20(8)	[30]
1.47(8)	[33]	1.41(11)	[31]
1.41(5)	[33]		
3.61(2.20)	[34]		
3.55(1.10)	[34]		
3.77(1.40)	[34]		
3.81(1.70)	[34]		
9.8(1.50)	[35]		
1.63(9)	[28]		

1.3.3 Decay Electron Time Spectrum Analysis

The main experiment presented in this work is the analysis of the decay electron time spectrum obtained using an argon-doped gas target. With an argon-doped target gas substituted for the pure protium gas of the Λ_S measurement, such a data set is readily obtainable from the MuCap experimental setup. Moreover this can be done with a data sample of $10^8 - 10^9$ decay events.

The known free muon decay rate λ_μ allows a novel analysis of such data. With λ_μ fixed, independent results for the $\Lambda_{pp\mu}$, $\Lambda_{p\mathrm{Ar}}$ and Λ_{Ar} kinetic rates are obtained in a single fit to the decay electron time spectrum, described in Eq. 1.36. This method determines the effective molecular formation rate, $\Lambda_{pp\mu}$, to better than 5.0% relative precision, while independently determining $\Lambda_{p\mathrm{Ar}}$ and Λ_{Ar} to better than 2.0% relative precision. An independent determination of the argon kinetics rates minimizes systematic bias due to the correlated relationship these parameters have in the fit function, described in Eq. 1.36. That is further motivated by the observation that the argon transfer and capture rates are not known to better precision than this method can determine.

The statistical power of a fit to the decay electron time spectrum arises from the distinct disappearance rates of the kinetic states and the non-linear expressions that determine the contribution of each of these rates. The non-linear and correlated features of the fit function means that it will be important to verify the stability and reproducibility of the fit procedure as a critical factor in the examination of the extracted results.

Capture Neutron Time Spectrum Analysis

The MuCap experiment also provides for the detection of capture neutrons. Under the conditions described here, $\approx 7\%$ of all muon stop events result in capture onto argon, generating a statistical sample of $\mathcal{O}(10^6)$ such events. The time spectrum of capture events is dominated

by the population of the μAr state, $n_{\mu\mathrm{Ar}}(t)$, where

$$n_{\mu\mathrm{Ar}} \propto e^{-r_{\mu p}t} - e^{-r_{\mu\mathrm{Ar}}t}. \tag{1.41}$$

An analyses of the capture time distribution by direct measurement of the capture neutrons can determine the $r_{\mu p}$ and $r_{\mu\mathrm{Ar}}$ disappearance rates. The comparison of such results is a valuable consistency check for the more precise decay electron time spectrum analysis, which also determines these disappearance rates (Equations 1.33 and 1.34).

Chapter 2

The MuCap Experiment

This chapter presents the techniques and methods used in the MuCap experiment. The experiment depends on observing muons stoped in an isotopically pure hydrogen gas. A time projection chamber (TPC) detector is both a hydrogen target and an active detection volume for the identification of muon stop events in a well-defined fiducial volume. This design enables a clear differentiation between events that stop in the target gas, and those that may have interacted with heavier materials.

The experimental concept is to identify muon entrances into, and stops in, the TPC detector. The subsequent detection of the decay electrons and capture neutrons is the basis for obtaining time spectra data for the analyses described and motivated[1] in Chapter 1.

The muon beam will be described first. The first of the detector components to be presented are the entrance detectors, including the μSC scintillator. The TPC and cylindrical electron tracking and timing detectors, named the ePC and eSC respectively, are also presented. Eight liquid scintillator neutron detectors complete the detector setup. The layout of the detector components is illustrated in Figure 2.1.

2.1 The Muon Beam

The source of muons for the MuCap experiment is the πE3 beamline at the Paul Scherrer Institute (PSI) in Villigen, Switzerland. The PSI accelerator produces a 590 MeV (kinetic energy) proton beam with a current of 2.2 mA, making it one of the most powerful sources

[1]Section 1.3 for the present work.

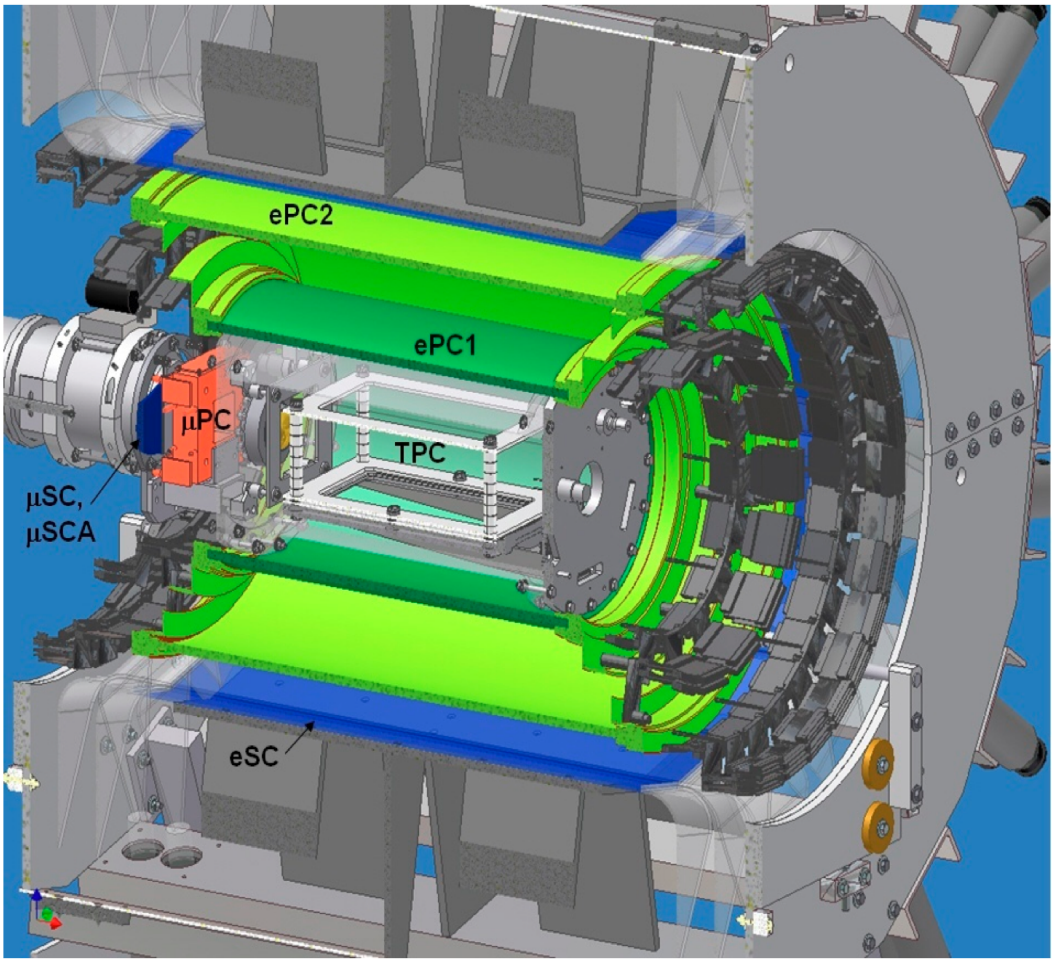

Figure 2.1: Diagram of the MuCap detector, starting with the muon entrance detectors, including the μSC entrance counter. The muon then enters the central target TPC and stops in the 10 bar hydrogen gas. Around the TPC are the cylindrical ePC wire chambers and eSC scintillator hodoscope for the tracking and timing of decay electrons, respectively. Eight liquid scintillator neutron detectors are mounted at a distance that places them outside the eSC hodoscope, as depicted in Figure 2.6.

in the world. The 1.3 MW proton beam is used to generate high-intensity pion and muon beams for applied and fundamental physics experiments. The πE3 beamline is produced from proton collisions on a graphite target, on which a low-energy pion "cloud" is created near the surface. The muon beam is generated by the dominant

$$\pi^- \rightarrow \mu^- + \nu_\mu$$

decay mode of the π^-. The muons are collected and channeled by a series of focusing (quadrupole) and bending (dipole) magnets. A low momentum beam of $p \approx 32.6(1)$ MeV/c is selected, which corresponds to $\approx$ 5.0 MeV in energy. The low momentum maximizes the fraction of muons that stop in the hydrogen target gas (observed to be $\approx$ 50%), and subsequently the rate at which decay and capture events are observed in the experiment. The standard operating conditions produce a beam rate of $7{\times}10^4$ muons/s, which corresponds to a $\approx$14 µs wait time between muon events.

The beam line has two components that are critical to the MuCap experiment. The first is the separator, which is a $\vec{E} \times \vec{B}$ velocity filter. This device uses a magnetic field and a compensating, transverse, electric field to select particles of a given mass and momentum. The muon beam contains an electron background produced from decays in flight, and at the production target from other pion decay modes. These electrons are a potential background to the experiment that the separator reduces. The magnetic and electric fields of the separator are empirically tuned to produce no net deflection for muon at the beam momentum of 32.6 MeV/c, and to deflect the faster moving electrons. The electrons are stopped in a collimator slit at the downstream side of the separator. The μSC entrance counter measures the ratio of muons to electrons in the beam to be 15:1. One critical use of the μSC is to distinguish between muons and electrons entering the experiment.

The second key beamline component is the electrostatic kicker [36]. The kicker applies a 25.0 kV potential difference across a 12 mm gap between two sets of 75 cm-long, 20 cm-wide

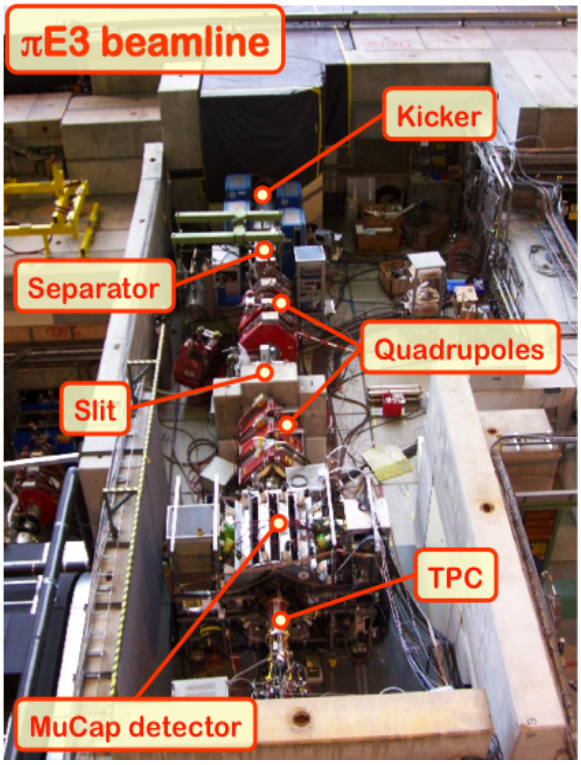

Figure 2.2: Overhead-view photograph of the πE3 beamline at PSI. The separator and kicker components are labeled along with several others. The beam leads the muons too the detector and ultimately into the TPC. Note: This photo was taken with the TPC positioned outside of the detectors for servicing. The aluminum pressure vessel (visible) containing the TPC is positioned inside the center of the cylindrical electron detectors under normal operating conditions, as depicted in Figure 2.1.

aluminum conducting plates. The two plates of each set are centered and parallel to each other around the beam axis, and produce a vertical and uniform electric field. The two sets of plates produce a field region that is a total of 150 cm long along the beam axis, with a 5 cm gap between each set of plates. Four sets of fast-switching MOSFET cards control the kicker electronics such that the plates can be fully charged to their maximum potential difference within 60 ns. When the kicker is off, the muon beam passes through the vacuum vessel of this device unaffected by any electric field. When turned on the kicker electric field deflects the muons away from the beam trajectory and suppresses the beam rate by ≈ 100.

2.1.1 Muon Entrance Counters

After exiting the beamline through a mylar window the muons encounter a series of detectors that identify muon entrances into the experiment. The first detector, the μSCA as labeled in Figure 2.1 is a 5 mm-thick plastic scintillator veto counter, with a 40 mm diameter hole in the center. The hole is centered around the optical axis of the beam as it enters the experiment. This detector identifies and vetoes events when the incoming muon is divergent from the beam axis, and unlikely to enter the TPC. The downstream side of this detector is lined with lead that is thick enough to stop such muons. The stopped muons quickly capture onto the lead with a rate $\Lambda_{\mathrm{Pb}} = 12 \times 10^6$ s^{-1}, which removes the decay of these muons as a source of background.

The μSC entrance counter is a 0.5 mm-thick scintillator mounted immediately downstream from the veto counter and centered on the optical axis of the beam. The low-energy (≈ 5 MeV) beam muons deposit ≈ 4 times [1] more energy per distance traveled (dE/dX) in the scintillator than the faster electrons. The electrons are minimally ionizing particles in the scintillator medium and induce pulses with smaller amplitudes. The pulse signal of a muon is thus distinguishable from that of an electron. The detector, moreover, is thin enough to minimize the scattering of incoming muons that must pass though this detector.

In addition to providing particle identification for muon entrance events, the μSC provides critical timing information for the muon stop events. The muon entrance time assigned by this detector, t_μ, is taken as the time of a muon stop in the hydrogen gas. This assumption is experimentally appropriate since a stopped muon will rapidly enter the μp cascade process, and find the singlet μp ground state on a prompt time scale of 10 ns.

The last detector associated with the study of muon entrances into the TPC is the μPC. This detector is a 2-D multi-wire proportional chamber that provides a cross section view of the muon beam as it enters the experiment. The μPC consists of two sets of 24 anode wires with 2 mm spacing, which are each surrounded by two cathode planes. One set of

anodes is oriented horizontally, and the other vertically, to define the two-dimensional (x, y) coordinate of a through-going muon. The mylar windows in the entering and exiting side of this detector are 50 µm thick and minimize scattering of the through-going muons. The veto, μSC, and μPC detectors are each readout by time-to digital converter (TDC) electronics[2]. The muon entrance detector (μSC, See Figure 2.1.) triggers the kicker and prevents muons from entering the experiment for one 25000 ns cycle in the Muon-On-REquest (MORE) mode. The beam is fully suppressed $\approx$ 600 ns after an initial muon entrance into the experiment[3], and the kicker remains on for a full 25000 ns cycle[4]. A fraction of beam muons can still reach the detector in the first 600 ns after the muon entrance trigger, but the efficiency of the μSC detector is such that $< 1 \times 10^{-4}$ of these events are not detected (and subsequently rejected). The veto and μSC detectors are used to reject any events with multiple muons associated with a single cycle of the kicker. The kicker combined with the entrance detectors implements a single muon event structure for the study of decay and capture products in the target gas in the MORE mode of operation.

The significance of the single-muon event structure implemented with the MORE mode is to prevent events where more than one muon enters the experiment in a single kicker cycle, called pileup events. When multiple muons enter the experiment, they can each produce a decay electron or capture neutron. An ambiguity arises if multiple muons undergo decay, for example, as to which electron is associated with which muon stop. One motivation of the MORE mode is to remove such an ambiguity from the interpretation of events and provide pileup-protection.

The other motivation for implementing the MORE setup is that the use of the kicker enhances the rate at which the experiment can record pileup-protected events. Without the

[2]The specific device used is the V767 module from CAEN.

[3]The 600 ns between the initial muon hit in the μSC and the kicker being fully turned on is due to the following: $\approx$350 ns is from the processing time of the electronics, $\approx$100 ns is associated with the speed of the electrical trigger signal reaching the kicker, $\approx$60 ns is due to the switching time of the kicker, and finally the time of flight for the undeflected muons to reach the experiment is $\approx$100 ns.

[4]A 500 ns time buffer is applied after each kicker cycle to prevent damage to the MOSFET electronics.

kicker beamline design the DC rate of the beam line must be reduced to 2×10^4 muons/s to minimize the fraction of pileup events. The reduced beam rate results in an increased wait time of $\approx$ 50 µs between events. The MORE mode of the beamline setup was critical to recording 10^{10} muon decay events for the pure hydrogen data set in a practical measurement period of $\approx$6 months. The theses of Kiburg and Banks [37, 38] present the MORE mode setup, and the issue of pileup for the MuCap experiment in further detail, respectively.

2.2 Hydrogen Target Detector: The TPC

An incoming muon enters the TPC pressure vessel through a hemispherical beryllium window that is 0.5 mm-thick. The cylindrical aluminum TPC vessel is 395 mm in diameter with 4 mm thick side walls. The vessel thickness is minimized to safely hold the hydrogen gas at 10 bar pressure, while minimizing the scattering and energy loss of through-going electrons and neutrons.

2.2.1 Target Gas Preparation

The main measurement of the muon disappearance rate, λ_-, requires an isotopically pure protium target gas. The pure protium gas is prepared from the electrolysis of deuterium-depleted water [39]. Subsequent isotopic separation in a cryogenic distillation column further reduces the concentration of deuterium to less than 0.01 ppm. In the pure hydrogen experiment the TPC target gas is continuously circulated through the CHUPS purification system [40], which maintains the concentration of both oxygen and nitrogen in the target gas at <0.01 ppm.

The present work for the measurement of $\lambda_{pp\mu}$ requires an argon-doped protium gas. A sample of pure protium doped with c_{Ar} =19.6(1.1) ppm (atomic) of argon is injected into the TPC[5]. Argon is removed from the target gas by the CHUPS, which is counter to

[5]The 19.6(1.1) ppm value for the concentration of argon covers the range of variation defined by the results

the needs of this experiment. The TPC vessel was consequently taken out of circulation with the purification system for taking these data. The result is that the concentration of oxygen and nitrogen impurities in the argon-doped gas is greater than under the pure hydrogen conditions. Chromatography analysis of argon-doped target gas shows 0.23 ppm of oxygen and 0.23 ppm of nitrogen at the end of the measurement period. Impurities in the target gas are a potential source of distortion in the decay electron and capture neutron time spectra. The oxygen and nitrogen impurities will be discussed as systematic effects in Sections 4.3 and 6.7, respectively.

The density of the argon-doped hydrogen gas is necessary to determine the final normalized $\lambda_{pp\mu}$ and $\lambda_{p\mathrm{Ar}}$ kinetic rates from the effective $\Lambda_{pp\mu}$ and $\Lambda_{p\mathrm{Ar}}$ rates extracted from the analysis fo the decay electron time spectrum. Pressure (P) and temperature (T) sensors in the detector setup provide for the determination of the gas density, where $P = 10.18(4)$ bar and $T = 301.5(3.0)$ K, respectively[6]. The pressure and temperature determine the molar density of the gas, ρ, to be $\rho = 403.5(4.7)\ \frac{\mathrm{mol}}{\mathrm{m}^3}$. The central value for the density obtained from calculations that take into account non-ideal gas properties of hydrogen [42], and which are accurate to 0.04% precision. The argon-doped hydrogen gas is very close to the ideal gas limit (to better than 1.0% accuracy), and the total error includes the uncertainties associated with P and T as determined by the ideal gas equation of state,

$$\rho = \frac{P}{RT},$$

where R is the ideal gas constant, $R = 8.314\ \frac{\mathrm{bar}\cdot\mathrm{m}^3}{\mathrm{K}\cdot\mathrm{mol}}$. Relative to the density of liquid hydrogen, $\rho_{\mathrm{LH}} = 3.5121 \times 10^4\ \frac{\mathrm{mol}}{\mathrm{m}^3}$, the relative density of the argon-doped target gas is

from gas chromatography analysis of the target gas, 18.5(5) ppm, and the expected 20.6 ppm concentration determined from the gas mixing procedure.

[6]The quoted errors for the pressure and temperature include both the 1.0 σ variation of the sensor readout data, and the respective systematic error in the calibration of each sensor, determined to be 0.04 bar and 3.0 K, respectively [41].

determined to be

$$\phi = 0.0115(1).$$

2.2.2 The TPC

Energy deposition due to a charged particle moving in the detector (nominally a negative muon in this work) creates a cloud of electrons via ionization of the hydrogen gas. A 24 kV potential difference applies a uniform 2.0 kV/cm electric field across the 120 mm vertical height of the TPC. The electric field induces the cloud of electrons to drift downward to the bottom plane of the TPC with a velocity $v_{\text{drift}} \approx 5.5$ mm/µs. The drifting ionization electrons are subsequently detected on the 2-D multi-wire proportional chamber (MWPC) plane at the bottom of the TPC. The potential difference across the drift region of the TPC is generated by a cathode plane at -29.1 kV at the top of the detector, and the upper surface of the MWPC at -5.1 kV. Seven copper wires mounted around the frame of the TPC enhance the uniformity of the electric field. The TPC frame is pictured in Figure 2.3(a). The mounted pressure vessel setup is pictured in Figure 2.3(b). The sensitive volume of the detector is $15 \times 12 \times 28$ cm.

The MWPC plane consists of an anode plane of wires sandwiched between two cathode planes with a 3.5 mm half-gap separation. The 75 gold-plated tungsten wires of the anode plane are 25 µm thick and spaced 4 mm apart along the 28 cm length of the detector in the z (transverse to the beam axis) dimension. The cathode planes consist of 35 strips held at -5.1 kV relative to the anode wires at ground potential. The cathode strips are spaced 4 mm apart along the 15 cm width of the detector volume in the x axis (parallel to the incoming muon beam). Each cathode strip consists of 4 wires that are 50 µm thick and spaced by 1 mm that are connected to a single charge-integrating preamplifier for readout[7]. The anode and lower cathode planes are readout by the detector electronics.

The anode wires determine the z coordinate of the location of a muon stop, and the

[7]The strips towards the edge of the detector include a more than 4 [38].

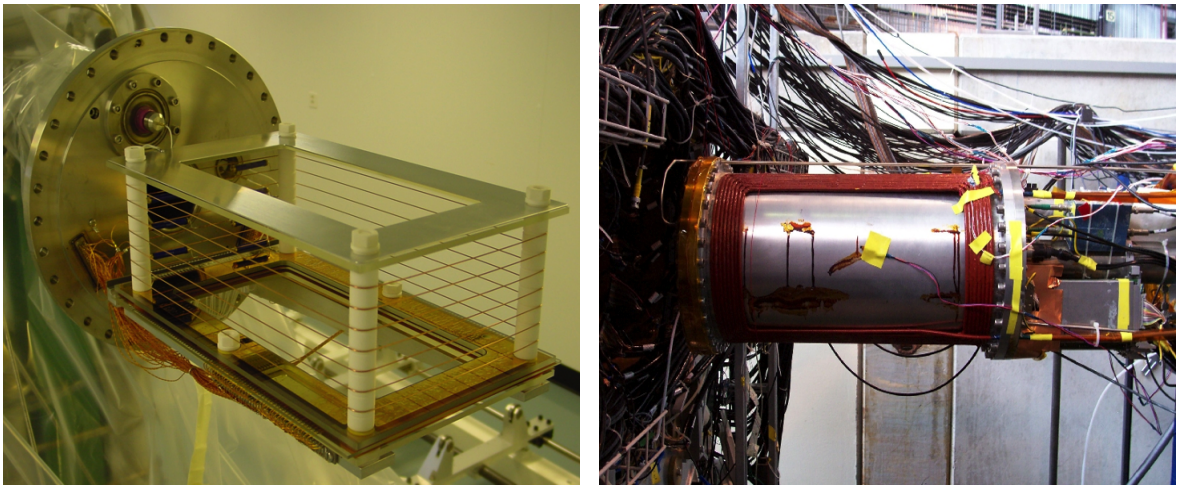

(a) TPC (b) TPC Pressure Vessel

Figure 2.3: Left: A picture of the TPC frame while removed from the aluminum pressure vessel. Right:A picture of the TPC as mounted in the aluminum pressure vessel being moved into alignment with the rest of the MuCap detector.

cathode strips determine the x coordinate. The drifting electrons are accelerated in the high-field region around the wires of the MWPC, which creates ionizing collisions with H_2 molecules and amplifies the signals induced on the chamber wires by a factor of ≈ 60 [38,43]. The anode wires and cathode strips of the chamber are read out in 200 ns intervals by custom TDC electronics. The notable feature of the electronics is that the TDCs operate as threshold discriminators at three independently adjustable energy thresholds. The energy settings of each threshold are motivated by the physics of the muon in the detector gas.

The working principle of the TPC is illustrated in Figure 2.4. The ionization electrons (green) induced by a muon event (blue) drift a given distance Δy every 200 ns, which corresponds to ≈ 1.1 mm in the y axis. The time-dependent readout of the MWPC (red) correlates with the vertical distribution of charge deposited in the gas as it drifts downwards in the y axis to the MWPC plane. This detection modality gives the projection of the charge deposited in the hydrogen gas onto the two-dimensional plane of the MWPC (light blue). The pairing of a 200 ns time bin at a given energy threshold and the wire on which the pulse is observed is the $\approx$1.1 mm by 4 mm two-dimensional coordinate of the TPC, called

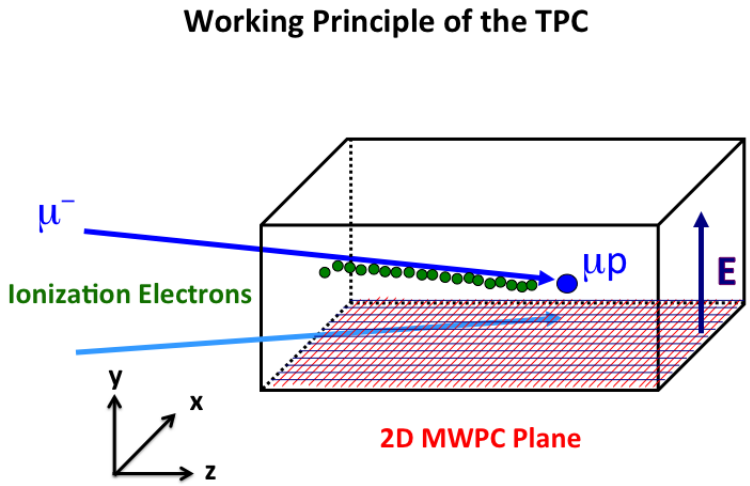

Figure 2.4: A μ^- particle (blue) moving through the active volume of the detector (black) creates a cloud of electrons (green) from ionization of the hydrogen gas. A 2 kV/cm electric field (purple) induces the cloud of electrons to drift downward to the bottom MWPC plane (red) of the TPC. The ionization charge induces electrical pulses in the high-field region of MWPC plane, in part through the amplification of the ionization signal from collisions in the hydrogen gas in this region. The pattern of charge observed by the MWPC is the projection (light blue) of the muon track onto the bottom plane of the detector. The signals induced on each individual wire are readout in 200 ns intervals by TDC threshold discriminators at three energy thresholds.

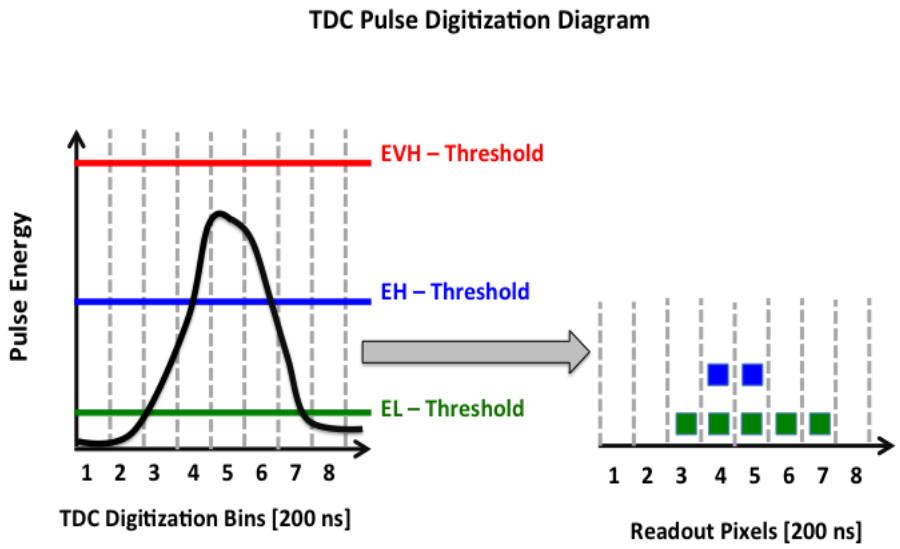

Figure 2.5: An illustration of an analog pulse on a wire in the chamber of the TPC target detector. In the TDC readout of the detector such a pulse is analyzed in 200 ns time bins and digitized into threshold discrimination information. The threshold discrimination is done at three physically significant energies, as discussed in the text.

a *pixel*. The TPC provides 3D coordinates, which are used to track muons that stop in the detector gas. The novel feature of the TPC design is that the detector is essentially a gaseous hydrogen target, while also providing readout information for the analysis of muon stop events.

The lowest energy threshold applied in the TDC readout of the MWPC anode wires is the EL "low" threshold. At 0.014 MeV in energy this threshold is associated with the energy deposition of a low-energy muon traveling through the hydrogen gas. The 0.060 MeV EH "high" energy threshold is associated with the increased (dE/dX) energy deposition of the muon as it slows down to stop in the hydrogen gas. The increased energy deposition of the muon as it slows is well quantified by the Bethe-Bloch relation[8]for dE/dX [1]. The EH "high" threshold is used as a signature of a muon stopping in the target gas. Finally, the

0.290 MeV EVH "very high" threshold is associated with a pulse induced from the recoiling nucleus in muon capture onto a $Z > 1$ nucleus. Such events are predominantly associated with the

$$\mu^- + \mathrm{Ar} \rightarrow \mathrm{Cl} + n + \nu_\mu$$

capture process in the conditions of this experiment.

Figure 2.5 depicts the read out of the deposited charge pulse arriving on a chamber wire at the bottom of the TPC, and the 200 ns digitization of the pulse. If a given threshold (EL, EH or EVH) is met at the clock boundary of the TDC time bin, then the following bin (pixel) is assigned as being above that threshold. A given pixel may meet more than one threshold condition since the EL-threshold is automatically met if the EH-threshold is indicated, and likewise for the EH and EL thresholds if the EVH-threshold is observed.

The cathode strips are readout in a similar way to anode wires, but the channels are discriminated only at the corresponding EL and EH energy thresholds. The cathode strips are oriented parallel to the beam axis, and a single muon track may only cross and be observed on a few (< 5) strips. That condition provides poor resolution for the dE/dX shape of the charge deposited by the muon stop in the x dimension. The result is that the EH-threshold discrimination is an unreliable indication of the muon stop location, and only the EL-threshold information is used in the analysis. In contrast the muon crosses more anodes (typically greater than 10) in the z axis, and the charge deposition of an event is better resolved in that dimension.

[8]This relation describes the increase in energy deposition for a muon with momenta between 1.0 and 10^7 MeV/c, but less well for momenta below ≈10.0 MeV/c [1].

[8]These thresholds are not strictly the same as those applied on the anode wires, in part because the strips are composed of multiple wires and the gain of the strips is different than for a single anode wire.

2.3 Decay Electron Detectors

The electron detectors include the ePC MWPCs and the eSC scintillator hodoscope. The cylindrical ePC chambers are the innermost detectors outside of the TPC vessel, as shown in Figure 2.1. The purpose of these detectors is to obtain 3D tracking information of the decay electrons. The ePC1 detector is the smaller of the two chambers, with a radius of 19.2 cm and a length of 69 cm. It is mounted directly outside the TPC pressure vessel. This detector consists of 512 anode wires with 2 mm spacing and 192 cathode strips in each of two cathode planes. The larger ePC2 chamber is mounted concentrically outside of the ePC1, is 32 cm in radius and 91 cm long. The ePC2 chamber consists of 1024 anode wires with 2 mm spacing, and 320 cathode strips in each of the two cathode planes. The operating voltages for the ePC1 and ePC 2 chambers in this experiment are 2640 kV, and 2740 kV, respectively.

The three planes (one anode and two cathode) of each chamber are read out to obtain temporal and spatial information about the decay electrons emerging from the TPC. The anode wires of each detector are parallel to the beam axis and represent lines of constant angle in the plane of cylindrical symmetry. The two cathode planes of each chamber are in right- and left-handed helical trajectories around the detector. The coincidence of an anode and a cathode hit provides a coordinate for the position of the electron hit in the surface plane of the chamber. The combination of a spatially and temporally coincident hit in the ePC1 and ePC2 chambers indicates a through-going decay electron track. The spatial coordinates determined by the chambers then define the trajectory of such an electron.

The timing of decay electrons is determined by the eSC scintillating hodoscope. The 16 segments of the eSC are mounted cylindrically around the TPC vessel outside of the ePC2 chamber, as shown in Figure 2.1. Each segment of the hodoscope consists of two 5 mm-thick scintillator layers that are 90 cm long. One photomultiplier tubes (PMT) is connected to both the upstream and downstream ends of the inner and outer layers of each segment, meaning four channels attached to each segment. The ePC and eSC detectors are read out

with customized TDC electronics (COMP). The timing resolution of readout electronics of the eSC detector is 1.25 ns. The eSC detector is additionally readout by custom waveform digitizer (WFD) electronics, originally developed for the MuLan experiment.

2.4 Liquid Scintillator Neutron Detectors

The MuCap experiment is equipped for the detection of capture neutrons with eight liquid scintillator detectors, mounted as indicated in Figure 2.1. Fast (MeV-scale energy) neutrons undergo scattering in the organic liquid scintillator medium, and the resulting recoils of protons induces a light pulse in the scintillator readout by a PMT optically coupled to the volume. Such detectors are also sensitive to pulses induced by gamma rays, which are a significant background to neutron signals in these detectors. Gamma rays with ≈ 1.0 MeV in energy undergo Compton scattering in the scintillator medium, producing scattered electrons. Electrons efficiently induce a prompt scintillation response that is linear with the (dE/dX) energy loss of the particle. Protons recoiled from a fast neutron hit, in contrast, are heavier and have a slower velocity than an electron with equivalent energy. The energy deposition (dE/dX) of a proton is larger than for an electron with the same energy [44]. The scintillator light response to protons is weaker than for electrons, which is due to quenching effects induced by molecules changed or "damaged" by interaction with the proton. A neutron hit consequently requires ≈ 3.0 MeV in energy to produce the same light yield as a ≈ 1.0 MeV gamma ray [44].

Decay and scattered beam electrons can induce pulses in these detectors. The decay electrons in particular become a background consideration for the selection of capture neutron events. This will be addressed in Section 3.1.6.

Organic liquids that are useful as scintillators have a characteristic π-electron structure to the energy levels [44] of the molecule. At room temperature the molecules exist in a singlet spin (S_0) states. The spin states in this case are split in the energy spectrum by the

vibrational modes of the molecule. The scintillation process of the organic molecule proceeds through the absorption of energy deposited by the incoming particle and the excitation to excited ($\approx$ 4 eV) S_1 singlet spin states. From the S_1 spin states, fluorescence proceeds on the time scale of ns, representing the dominant component of the scintillation response. The triplet T_1 spin states have lower energy than the S_1 states, and a much longer lifetime of $\approx 10^{-3}$ s that decay through phosphorescence. A crossing from the S_1 to T_1 states can occur [44], populating the longer-lived triplet state.

The larger the dE/dX energy deposition of a particle in the scintillator is, the more molecules are excited to the triplet state along the path of that particle. Bi-molecular interactions between two such excited molecules result in one molecule that is in a singlet S_1 state, and one in a lower energy S_0 ground state [44]. The molecule in the S_1 singlet state hence undergoes florescence on a delayed time scale. The larger the dE/dX of the particle interaction in the scintillator, the greater the delayed time component in the light pulse created by the event. The slower, heavier protons scattered in a neutron hit induce a light pulse with a larger delayed time component than observed in pulses induced by gamma rays via compton scattering. The pulse shape characteristics of events enable the identification of neutron and gamma ray hits in the detectors [44–46].

The neutrons produced in capture onto argon are predominantly between 1.0 and 3.0 MeV in energy, and those produced from capture onto the proton are 5.2 MeV. Detectors of this type can have a detection efficiency of greater than $\approx$ 50.0% for neutrons in this energy range [46]. The liquid scintillator detection methods are therefore well suited to the needs of this experiment.

The neutron detectors used in this experiment are on loan from the DEMON collaboration, which designed them for fast neutron detection [45, 47]. The cylindrical aluminum containers of the detectors are 160 mm in diameter and 200 mm in length, and hold 4 liters of NE213 organic liquid scintillator. The containers each have a front entrance wall (through which neutrons enter) that is 6.35 mm thick, and 21.5 mm thick side walls. The back wall of

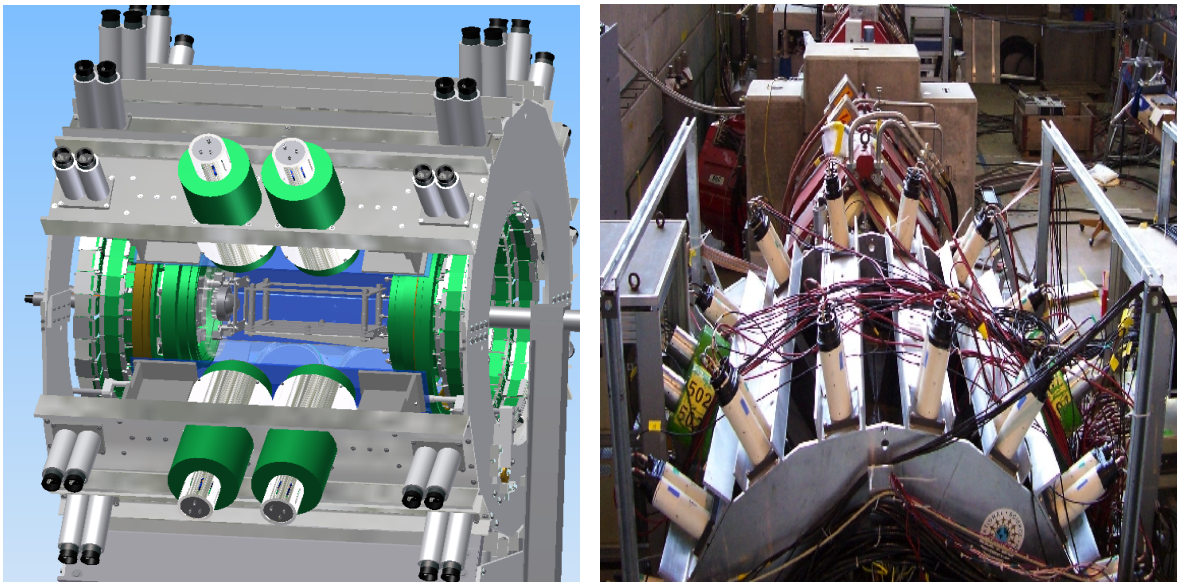

(a) Diagram (b) Picture of Installation

Figure 2.6: Left: A diagram depicting the mounting of the neutron detectors in the MuCap experiment, particularly with respect to the TPC. Right, an overhead picture of the actual detector, showing the neutron detectors (green) mounted in between the eSC hodoscope segments.

each container is made of 10 mm thick glass, which directly couples to a 130 mm diameter PMT. The size of the PMT enhances the efficiency of light collection and the linearity of the electrical response to the induced scintillation signal. These characteristics facilitate the pulse shape discrimination of neutron and gamma ray hits, because they make the PMT response more sensitive to the time-dependent shape of the light pulse.

The liquid scintillator detectors are mounted in four pairs in a cylindrically symmetric pattern around the central detectors, as shown in Figure 2.1. The radial distance from the center (beam) axis of the TPC to the front face of each scintillator detector is 400 mm. The detector volumes in each mounted pair are centered 120 mm up- and down-stream from the longitudinal center of the TPC. The total distance from the center of the TPC to the center of one of the scintillator volumes is 566 mm. A diagram and photo of the detector installation is shown in Figure 2.6.

The PMT signals from the detectors are read out by flash analog-to-digital-converter

(FADC) electronics, which are custom designed for the MuCap experiment [48]. The electronics are based on the Maxim MAX1213 12-bit ADC device, which has a maximum sampling rate of 170 MHz and a signal input range of ± 0.75 V. The measured noise level of the electronics is approximately 1.1 ADC-bits or 0.2 mV. These electronics are read out to the data acquisition system through an ethernet connection that is integrated into the FADC boards. The electronics provide a digitized waveform sample of each pulse observed in the detectors.

2.5 Data Acquisition and Processing

The respective electronic readout systems for each component of the MuCap detector are integrated into a single data acquisition system (DAQ). The DAQ is based on the Maximum Integration Data Acquisition Framework (MIDAS) [49], which organizes a collection of frontend software for each readout system and integrates the data from each detector on a single frontend PC. The entire detector system is read out in 100 ms intervals, and the recorded data are written out to a single run file. Each data run includes the readout from ≈ 2500 time blocks, and represents between 2 and 3 minutes of real-time data taking. The files are 1.6 GB in size and copied both to an archival backup system at PSI, and written to LTO2 magnetic tapes. At the conclusion of the measurement run the LTO2 tapes, which in total represented 50 TB of raw data for the run 11 measurement period, were readout and archived for analysis at the National Center for Supercomputing Applications (NCSA) in Illinois.

The analysis of the MuCap data relied both on the NCSA supercomputing facilities and the Nuclear Physics Laboratory (NPL) computing cluster. Each run file is processed in two stages. The raw level analysis code processes the electronic read out information from the detectors and organizes it into basic particle tracking and analysis information. Importantly, the data of TPC, electron and muon detectors are organized into analysis objects for further

processing.

The analysis code integrates with the foundation of the ROOT [50] software package, which is a widely used set of software tools for data analysis. The raw analysis makes basic diagnostic plots such as event distributions and rates and integrates important (slow-control) monitoring information about the experimental conditions. Finally, the raw stage processing organizes the data into a ROOT tree structure for further analysis. The muon, electron and neutron event analyses are kept separate at the first stage of the data processing to allow each detector system to be independently analyzed and calibrated.

The second stage of the analysis is where event selection criteria are implemented, and the decay electron and capture neutron time spectra are histogrammed. It is at this stage that the neutron pulse waveform analysis, to be discussed in Section 3.1.5, is applied to the raw waveform data obtained from the FADC readout. The bulk processing of the data was performed at the NCSA, and the fitting and higher level-level analysis work at the NPL cluster.

Chapter 3

Data Analysis and Preparation

This chapter will present the analysis techniques and criteria used for the identification of muon decay and capture events. The selection of decay events uses the standard procedures and criteria developed for the analysis of the pure hydrogen data set [37]. Finally, the pulse discrimination of neutron signals and selection of the muon-neutron pairs for the capture neutron time spectrum is discussed.

3.1 Event Analysis and Selection

3.1.1 Muon Entrance Criteria

The μSC detector provides the timing information for a muon entrance into the TPC, and it is used along with the kicker to implement a single muon event structure and initiate a 25000 ns measurement period. The μSC detector signal for a candidate muon entrance is first subject to a 29 ns software dead time, where a second hit in the detector is not individually recognized if it occurs within 29 ns of a hit. Time-coincident information in the μPC is paired with each μSC event to form a candidate entrance. The data collection also includes signals verifying kicker transitions. Several analysis conditions are applied for the selection of muon entrance events.

The analysis identifies coincident clusters of hits in the μPC detector. A software dead-time of 650 ns is applied to the μPC hits, which prevents after-pulsing in the chamber wires from being recognized as independent events. A $\pm$230 ns coincidence window is applied to

clusters of hits in the horizontal and vertical anode wires. Clusters must be separated by 2 wires (4 mm) in order to be processed as separate events. The earliest hit in a cluster determines the time of the event in each anode plane. The hits observed in the x and y planes of the detector are then subject to a $\pm$190 ns temporal coincidence to define full xy-coincident hits. The μPC data is also used to determine the profile of the beam immediately upstream of the TPC.

The μSC and μPC hits are paired with a $\pm$130 ns coincidence condition for each candidate muon entrance. The μPC chamber has poorer time resolution than the μSC scintillator, and the time of the μSC determines the time of the muon entrance, t_μ, as indicated in Section 2.1.1. The final coincidence condition applied to each candidate entrance event is that there must be a kicker transition signal within $\pm$10 ns of the candidate μSC time. Each candidate entrance event that meets the above μSC$\cdot\mu$PC$\cdot$kicker coincidence criteria must additionally be separated by 25000 ns from any other entrance counter hits to be accepted as a muon entrance signal. This final condition completes the definition for *pileup-protected muon entrances* into the experiment.

3.1.2 Muon Stop Identification and Selection

A muon entrance that meets the above conditions is used in the analysis as a trigger to look for TDC readout information for identifying a muon stop in the TPC. The TDC data for muon stop events is organized into analysis objects at the raw stage of the data processing. Several analysis procedures are applied to the TDC data that extract information for selection cuts implemented in the later stage of the analysis. An observed event in the TPC must first be in coincidence with a pileup-protected muon entrance to be accepted as a *muon stop event*.

The deposition of energy from a muon stopping in hydrogen creates a series of pixels at the EL energy threshold (or higher) which are contiguous in space (anode wires) and coincident in time. A contiguous series of coincident pixels is called an *island*. A candidate

island must have at least one EH pixel. In some muon tracks every contiguous wire may not be excited above the EL-threshold, and a 1 pixel discontinuity within an island is allowed in the $z:y$ plane. Two potential islands are separated only if they are spaced by two or more pixels that show no EL-threshold discrimination in y and z. Two events depositing charge in the TPC must be separated by 8 mm in the wire chamber plane and 400 ns in the vertical time axis (corresponding to ≈ 2.2 mm in y) in order for each to be identified separately in the analysis.

Figure 3.1 displays the pixelated readout of a muon stop event. The horizontal axis represents the time of each pixel relative to the muon entrance time t_μ. The vertical axis corresponds to the anode wires (z axis) of the chamber in the $0 - 80$ range, and the cathode strips (x axis) in the $81 - 115$ range in the upper region of the plot. The contiguous region of charge deposition induced by the muon stop is represented by the EL- (green) and EH-threshold (blue) pixels determined from the TDC readout of the event. A loose (red) and tight (blue) fiducial volume is indicated in both the $z:y$ and $x:y$ planes by line boxes. These volumes are used to implement several analysis cuts for the stop location and any EH-threshold pixels of a candidate event, as will be explained below. The event shown meets all of the analysis cuts applied in this work.

Fiducial Volume Cuts

The pixel island of each candidate event is analyzed to determine the muon stop location and several track parameters. The z coordinate of the stop location is established by identifying the most downstream anode involved in the event that is excited to the EH energy threshold, which is the anode on which the muon stop is assumed to have been detected. The $y_{\rm stop}$ coordinate is determined from the time of the first EH-threshold pixel observed on the stop-anode, $t_{\rm stop}$, and the time of the observed entrance t_μ, where

$$y_{\rm stop} = v_{\rm drift}(t_{\rm stop} - t_\mu).$$

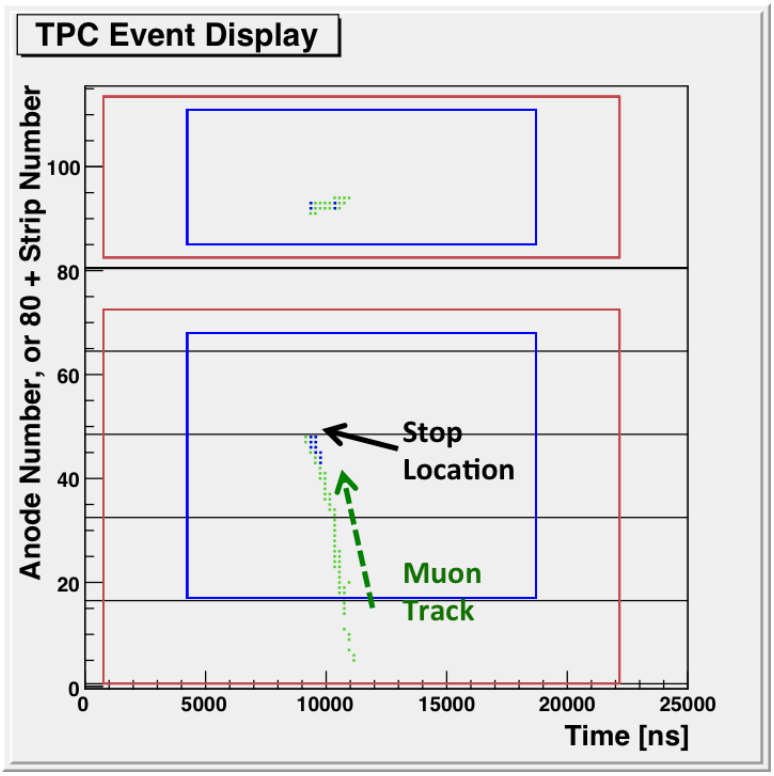

Figure 3.1: Example of the pixelated read-out information from the TPC for a typical muon stop in the MuCap TPC event display. The horizontal axis represents the time (y) coordinate of each pixel, relative to the muon entrance time t_μ. The vertical axis of this plot represents the anode and cathode wires of the MWPC (and also the x and z spatial coordinates of the pixels). The readout of the anode wires is represented in the lower ($1 - 80$) region of the vertical axis of the plot. The readout of the 35 cathode strips is likewise shown in upper ($81 - 115$) region of this plot. The EL- (green) and EH-threshold (blue) pixels are shown in color, as illustrated in Figure 2.5. This event meets all analysis cuts applied to select fiducial muon stops.

A cathode strip EL-threshold pixel must additionally be found in coincidence within ±200 ns of t_{stop}. The x coordinate of the stop location is taken as the weighted sum of the coordinates of all cathode strips excited to the EL-threshold in same time bin as t_{stop}. If no cathode pixels are coincident in the same time slice at t_{stop}, the adjacent time bin information is used to determine the x coordinate.

A series of fiducial volume cuts are applied to each candidate event. The first is that the pixel island must be entirely contained within a loose "Track" fiducial volume. The determined stop location of the event must be within a tighter "Muon Stop" fiducial volume. These volumes are represented by the red and blue line boxes in Figure 3.1, and the coordinate ranges are reported in Table 3.1. The final fiducial volume condition is that no EH-threshold pixels in the event island can be outside of the muon stop fiducial volume in the $z : y$ (anode:drift) plane.

Table 3.1: Table of coordinate ranges for the track and the tighter muon stop fiducial volume. The pixel ranges are reported respectively in units of: cathode wire number; time relative to the muon entrance t_μ in ns; and anode wire number for the x, y and z axes of the detector. These ranges correspond to the spatial coordinates of the detector. Note: The ranges indicated are inclusive for these conditions.

	Track Fiducial Volume		Muon Stop Fiducial Volume	
Axis	Pixel	Coordinate	Pixel	Coordinate
x	3- 33	-60 - 60	5 - 31	-52 - 52
y	750 - 22175 ns	-59.3 - 59.3	4237.5 - 18687.5 ns	-40 - 40 mm
z	1-72	-132 - 154	17 - 68	-66.4 - 137.6

Particle Track Cuts

Three particle track criteria are applied to the pixel island of each candidate muon stop event. A straight-line fit to the EL-threshold pixels is performed, and the reduced χ^2 of that fit determines the goodness-of-fit for a particle track. A minority of the candidate events are not well described with a single-line fit. Such events are potentially associated with $\mu + p$ scattering. The charge deposited at the interaction point in such an event may result

in a EH-threshold signal in the TPC readout, but in this case the EH threshold is not an indication of a muon stop. The outgoing muon may deposit a EL-threshold track of pixels away from the point where it scattered. A two-line fit (meaning two connected straight-line segments) is applied to the 5% of the events that exhibit the poorest goodness-of-fit. The reduced χ^2 of the one-line or two-line fit must be less than 2.0 for an event to be accepted in the analysis.

The second characteristic determined from the fit is the total length l of the pixel island. A candidate track event must be at least 32 mm long to prevent noise events from being accepted in the analysis.

The final track criteria is the "head" cut, which is the distance between the fitted end point of the track and the muon stop location, h_t. In some events, such as cases of $\mu + p$ scattering, a trail of EL-threshold pixels may exist past the muon stop location. Applying a cut on the spatial extent of such downstream EL-threshold pixels removes events where the muon may not have stopped in the fiducial volume of the detector. The analysis requires that $h_t \leq 18$ mm. The χ^2, track length, and head cut conditions are required for a particle track in the TPC.

The EH-threshold, fiducial volume, cathode coincidence and track-fitting criteria represent the complete set of analysis cuts for the selection of muon stop events. Additional details about these analysis methods have been documented extensively in the theses of Kiburg [37], Clayton [51] and Banks [38].

3.1.3 Electron Track Selection

The analysis of the ePC and eSC detectors proceeds in the raw stage of the data processing. The analysis processes electron detector data separately in the raw level, and prepares the data to later create muon-electron pairs.

The electron timing is determined by the eSC scintillator hodoscope detector, as described in Section 2.3. A software deadtime of 50 ns is applied to the discriminated signals of each

PMT channel of the detector readout. A candidate electron hit in the hodoscope is identified by a fourfold coincidence condition with a 25 ns resolving time[1] The time of an observed electron, t_e, is defined as the average of the pulse times observed from the four PMTs.

The electron track (Section 2.3) is determined from the ePC wire chamber detectors. A cluster of hits must be observed on the anode plane and on one of two cathode planes of a chamber to be identified as an event in that detector. The analysis procedure forms spatially and temporally coincident clusters of hits within the readout planes of each chamber, respectively. A temporal coincidence is then applied to pairs of ePC1 and ePC2 hits, to identify through-going electron tracks. The combination of a longitudinal and angular coordinate (z, ϕ_{eTrack}) from each chamber defines a three-dimensional vector.

The complete electron track definition includes the timing determined by the eSC, and the spatial tracking determined by the ePC wire chambers. A spatial and temporal coincidence between a paired eSC hit and ePC1-ePC2 coincidence event is required for electron tracks accepted in the analysis. Further information about the tracking algorithms and coincidence conditions applied in the analysis are available in the thesis of Clayton [51].

3.1.4 Decay Electron Event Selection

In the second stage of the analysis, coincident pairs of muon stop and and electron events are created. The decay time, t_{decay}, of each muon - electron pair is defined as

$$t_{\text{decay}} \equiv t_e - t_\mu,$$

where t_μ and t_e are the muon and electron times as determined by the μSC and eSC, respectively. The individual electron track and muon stop selection criteria are applied for each candidate coincidence pair where $-30000 < t_e - t_\mu < 30000$ ns.

Each muon - electron pair is further analyzed to determine the distance of closest ap-

[1]Each of the four PMTs connected to the segment of the eSC involved in the hit is required to show a discriminated pulse within 25 ns.

proach, b, between the electron track and the muon stop location, called the impact parameter. That distance is a discriminant for cases where the observed electron is not causally connected to the muon stop. A maximum threshold value is set at $b \leq 120$ mm. Applying this cut reduces the random background of the decay electron time spectrum by a factor of ≈ 5. This analysis cut is discussed further in Section 5.4.

The decay time spectrum is histogrammed with 40 ns binning, which corresponds to the 25 MHz clock frequency of the TDC electronics used for the eSC readout. The decay electron time spectrum is thus defined and the analysis of these data will be discussed in Chapters 4 and 5.

3.1.5 Neutron Pulse Analysis

The analysis of pulses in liquid scintillator detectors is necessary for the identification of capture neutron events. The FADC readout of pulse events in the scintillator detectors provides information for the discrimination of neutron and gamma ray hits. The 170 MHz ADC sampling rate corresponds to ≈ 5.9 ns time bins in the raw pulse waveforms. Each raw pulse waveform is fitted with an interpolation function and resampled from that function by factor of 20. The interpolation fit is implemented in ROOT with a TSpline3 object. The procedure applies a third-order polynomial fit to the raw waveform and determines the values assigned to a resampled waveform in 0.3 ns intervals. An example of a raw waveform pulse and the resampled waveform is shown in Figure 3.2. The time assigned to each event, t_n, is the time of the peak bin in the resampled waveform. The pedestal offset of each pulse, p, is determined by the average value of the first six sample bins of the raw waveform. The pulses observed in the liquid scintillator detectors are on the scale of 250 ns in length.

The remaining analysis procedures relate to the discrimination of pulses from neutron and gamma rays from the waveform data. A hit in the liquid scintillator detector from a neutron produces a pulse that decays more slowly in time than a pulse induced by a gamma ray. The ratio of the total pulse integral and the integral of the pulse in a later time region

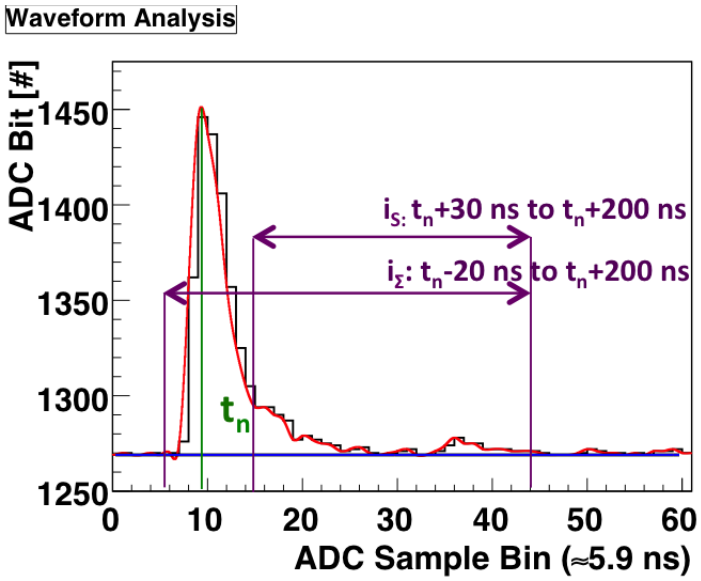

Figure 3.2: A sample pulse waveform from the ADC electronics (black) is shown here. The raw pulse, which has $\approx$ 5.9 ns time resolution, is resampled with $\approx$ 0.3 ns resolution with an interpolation method, as discussed in the text. The pedestal offset (blue) of the pulse is determined by the average of the first 6 sample bins of the raw waveform. The resampled waveform (red) is used for the analysis of the pulse. The peak bin of the resampled pulse defines the time of the observed hit, t_n. The total integral of the pulse, i_Σ, is defined in the -20 to 200 ns time region relative to t_n. The slow integral of the pulse i_S is defined in the 30 to 200 ns time region relative to t_n (noted in purple). The ratio of i_S to i_Σ defines the pulse-shape discrimination ratio r_{PSD}, used for the discrimination of neutron and gamma ray events. The pulse shown here is an example of an identified neutron signal.

(after the pulse peak) is the pulse shape discrimination (PSD) ratio, r_{PSD}. This ratio is a discriminant for identifying the two types of events.

The total integral of each pulse, i_Σ, is determined by the integral of the resampled waveform from 20 ns before to 200 ns after t_n after the pedestal subtraction, (noted in purple in Figure 3.2). The slow integral, i_S, of each pulse is analogously defined for the region 30 - 200 ns after the peak (noted in Figure 3.2). The PSD ratio is determined as

$$r_{\mathrm{PSD}} = \frac{i_S}{i_\Sigma}.$$

The separation of neutron (red) and gamma ray (blue) pulses in the discrimination procedure is depicted in Figure 3.3. The criteria for neutron events are determined for each

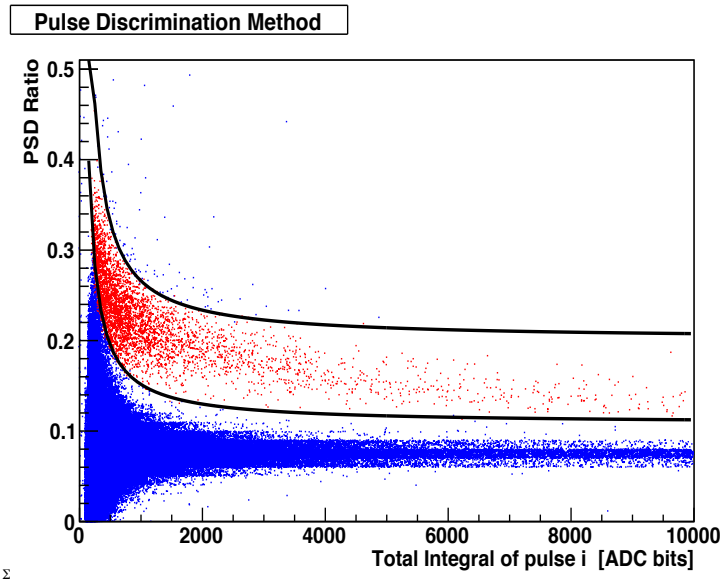

Figure 3.3: This plot illustrates the separation of the neutron and gamma ray pulses using the PSD ratio discriminant, r_{PSD}. The vertical axis is the PSD ratio of pulses, and the horizontal axis is the total integral, i_Σ. The gamma ray pulses (blue) are well separated from the neutron (red) for pulses down to 300 bits in i_Σ. The criteria implemented in the analysis require that a given pulse meet the requirement that $l_{min}(i_\Sigma) < r_{\mathrm{PSD}} < l_{max}(i_\Sigma)$ to be identified as a neutron signal. The lower and upper limits (black), $l_{min}(i_\Sigma)$ and $l_{max}(i_\Sigma)$ respectively are also shown here. The above plot represents the discrimination of neutron and gamma ray pulses in a single channel, detector 2 as reported in Table 3.2.

detector channel, where r_{PSD} must be between a minimum and maximum value [52], l_{min} and l_{max}. The limits, l_{min} and l_{max}, vary empirically with the total integral of the pulse where

$$l_{min} = c_{min} + \frac{k_{min}}{i_\Sigma} \text{ and } l_{max} = c_{max} + \frac{k_{max}}{i_\Sigma}.$$

The discrimination condition is then applied such that

$$l_{min} < r_{\mathrm{PSD}} < l_{max},$$

as appropriate to the channel and total integral of each pulse. The pulse discrimination parameters (c_{min}, k_{main}, c_{max}, and k_{max}) for each of the seven detector channels are reported in Table 3.2. One detector is excluded from the analysis because noise in that channel of electronics causes the pulse discrimination to be unreliable, making those data unusable.

Table 3.2: Table of the neutron pulse discrimination parameters (c_{min}, k_{main}, c_{max}, and k_{max}) determined for each of the 7 detector channels used in this analysis, as discussed in the text. Obtained from T. Gorringe [52].

Table of Pulse Discrimination Parameters				
Channel	c_{min}	k_{main}	c_{max}	k_{max}
1	0.0918	41.686	0.1535	64.084
2	0.1081	43.463	0.2012	64.784
3	0.0827	50.796	0.1544	65.904
4	0.0995	67.818	0.1946	83.943
5	0.0894	58.791	0.1798	73.817
6	0.0694	58.791	0.1616	80.793
7	0.1051	56.969	0.2096	88.194

The total integral of each pulse is associated with the energy of each detected event. The final criteria applied to the selection of neutron pulses in the analysis is that the total integral i_Σ must be between 400 and 5000 bits. That selection criteria is calibrated to correspond to neutrons between 0.8 and $\approx$ 5 MeV in energy. The pulse discrimination and total integral selection cut completes the analysis definition of a neutron signal.

3.1.6 Capture Neutron Event Selection

As for the decay electron analysis, the processing of the muon stop and neutron events is done separately. The FADC data from the neutron detectors is pre-processed into raw waveform samples in the first stage of the analysis, and the pulse discrimination analysis is implemented in the second stage. Muon-neutron pairs are made in the second processing stage. The time of capture relative to the muon stop for these events, t^n_{capture}, is defined as

$$t^n_{\text{capture}} \equiv t_n - t_\mu,$$

where t_n and t_μ are the times of the neutron and muon, respectively. The same muon stop selection criteria discussed in Section 3.1.2 are applied to the selection of capture events.

The analysis examines each candidate muon-neutron pair where $-35000 < t_n - t_\mu < 35000$ ns. An event pair is selected if there is at least one pixel island that meets the above-described analysis cuts for the muon stop. No event is double counted if a second pixel island that is coincident with the same muon entrance meets the analysis cuts as well. The reasons for this will be explained in greater detail in Section 6.2. If multiple neutrons are found relative to a single muon stop, each neutron becomes part of an accepted muon-neutron pair.

A final condition is applied to each candidate capture event. Decay electrons represent the majority of events in this experiment, and muon decay is a process which is inconsistent with a capture neutron. Any paired eSC electron hit within $0 - 20000$ ns of a muon stop is taken as a veto condition for any neutron signal coincident with the same muon event. The $0 - 20000$ ns time region is used because the causality of the experiment dictates that a true decay electron or capture neutron will be observed after the muon stop. More details about this veto condition and a correction for the neutron background will be discussed in Section 6.1. The spectrum of capture times is histogrammed with 60 ns binning for each muon-neutron pair that meets this and the individual analysis conditions for a neutron signal

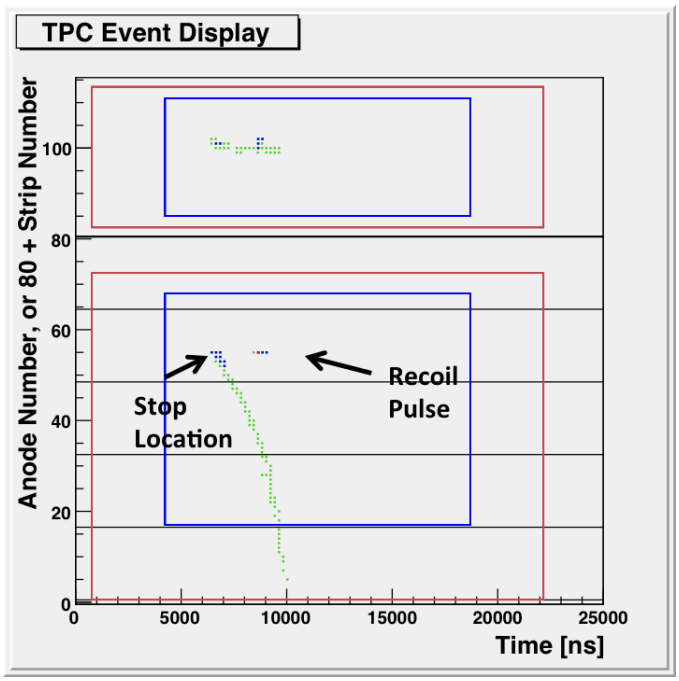

Figure 3.4: A recoil capture event as viewed in the TPC event display. The event is an example of muon capture onto a $Z > 1$ nucleus with only a nuclear recoil pulse observed following the muon stop. Events of this kind are the majority of those accepted in the capture neutron analysis.

and a muon stop. The binning ensures that the statistics of each time bin of the spectrum is sufficient to be assumed gaussian.

The neutron events in these data are predominantly associated with instances of muon capture onto an argon nucleus. In such events the remnant nucleus is recoiled and is a source of charge deposition in the TPC, which can result in an independently identifiable pulse in the muon event display. An example of such an event is shown in Figure 3.4.

Charge deposition due to the recoiling nucleus, or other aspects of the capture process, can interfere with the readout data of the muon stop in such events. Charge interference induced by the recoiling nucleus is largely excluded as a source of time-dependent bias in the selection of capture neutron events, which is discussed in Section 6.2. In a minority of capture events, however, the product nucleus is left in an excited state and a charge particle such as a proton or alpha particle may be emitted in the de-excitation process. The emission of such particles following muon capture is a significant source of interference with the muon

stop read out in the TPC, and a correction for this effect is presented in Section 6.2.

The recoil pulses observed in the TPC are a second observable for identifying events of muon capture onto argon. The y coordinates of the muon stop and the capture recoil nucleus are nearly identical, and the deposited charge of each drifts with the same drift velocity, v_{drift}. Because of that the capture time, t^R_{capture}, is defined by the time difference between the time of the first pixel of the recoil pulse that excites at least the EL threshold in the wire chamber, t_{recoil}, and the time coordinate of the muon stop location, t_{stop}, where

$$t^R_{\text{capture}} \equiv t_{\text{recoil}} - t_{\text{stop}}.$$

The series of conditions for the selection of such events is summarized as:

- A muon stop candidate event that survives all analysis cuts must be observed in the TPC.
- The anode on which the recoil pulse is detected must be within two wires of the anode on which it is determined that muon stop location is observed.
- The recoil pulse must be separated from the pulse of the muon stop by at least 400 ns in time to be identified in the analysis as separate pixel island.
- The recoil pulse must include at least one pixel excited to the EVH energy threshold.

Finally, an electron veto condition is applied, as for the capture neutron events.

The analysis of the capture recoil events is limited at early times because of the required 400 ns separation between the muon stop and recoil pulse in the TPC. That time is in addition to the $\approx$ 400 ns width of the muon stop pulse itself. Recoil pulses are not reliably identified until at least 1000 ns after the muon stop[2], owing in part to the 200 ns time resolution of the TPC. Fits to the time spectrum of these events are hence limited to a 1000 ns or later start-time. The statistical precision of the $r_{\mu p}$ and $r_{\mu\text{Ar}}$ results extracted

from these data is consequently uncompetitive with the analysis of the capture neutron time spectrum. The analysis of these data are not discussed further in this work for that reason. This method of observing capture events is presented as an alternative to neutron detection.

3.2 Summary of Argon-doped Gas Data

The argon-doped gas data was obtained over a measurement period of 46 hours during run 11. A total of 552 runs (0.9 TB of raw data) were obtained for these target conditions. The statistics obtained are summarized in Table 3.3. The number of fully selected muon-electron pairs obtained is 7.2×10^8. Additionally 1.1×10^7 discriminated neutron events are found, resulting in 3.0×10^6 muon-neutron pairs for the capture neutron time spectrum analysis.

Table 3.3: Table of event statistics obtained with the argon-doped target gas, both for an individual data run and the full data set. The first row reports the number of recorded muon stop events that meet all analysis cuts and are fully pileup-protected in the 30000 ns time region. The second row represents the number of detected electron hits that meet the full analysis criteria implemented for the ePC and eSC detectors. The number of muon-electron pair events with a 30000 ns time coincidence and meet the impact parameter cut condition is reported in row 3. The total number of recorded liquid scintillator events is reported in row 4 and the number of those that are identified as neutron signals is reported in row 5. Finally, the number of muon - neutron event pairs with a 35000 ns coincidence that meet the decay electron veto condition for a capture event is reported in the bottom row.

Table of Event Statistics		
Condition	Per Run	Full Data Set
Muon stop events	1.8×10^6	9.9×10^8
Electron hits	2.4×10^6	1.3×10^9
Muon-electron pairs	1.3×10^6	7.2×10^8
Liquid scintillator events	1.4×10^6	7.7×10^8
Discriminated neutron events	2.0×10^4	1.1×10^7
Muon-neutron pairs	5.5×10^3	3.0×10^6

[2]The selection of such events is arguably not reliable until 1900 ns after the muon stop. That is observed by looking at the variation of fit results with the start-time of the fit, which are not stable until this later time scale. This highlights the statistical sensitivity of the fit to the capture time distribution to the start-time allowed by the data, also true for the neutron time spectrum analysis.

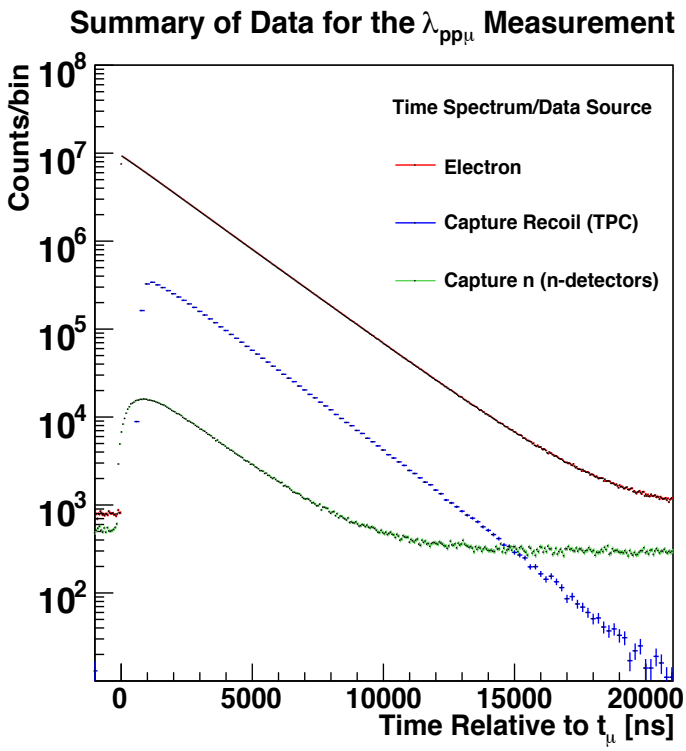

Figure 3.5: A summary of the full event statistics for the decay electron (red) and capture neutron (green) time spectra. The time spectrum of the recoil capture events observed in the TPC is also shown (blue) with 200 ns binning of the TDC readout. These are a special class of events that represent the capture time spectrum, as discussed in the text. Note: The binning of decay electron and capture neutron time spectra is 40 ns and 60 ns, respectively.

Figure 3.5 compares the summed decay electron time spectrum, to the summed neutron time spectrum. The number of counts in the decay electron time spectrum between 0 and 20000 ns after the muon stop is 4.8×10^8. The neutron time spectrum has 9.3×10^5 counts in the same time window. The analyses of these data and the extracted results are now the focus of the remaining chapters of this work. The time spectrum of capture recoil events appears for comparison, with statistics of 4.4×10^6 events in the 0 - 20000 ns time window.

Chapter 4

The Decay Electron Time Spectrum Analysis: Systematic Effects

The initial model for the decay electron time distribution considers three kinematic states: the μp and μAr atomic states and the $pp\mu$ molecular state. The time spectrum depends on four kinematic rates: the known free muon decay rate λ_μ; the effective molecular formation rate, $\Lambda_{pp\mu}$; the rate of muon transfer to the μAr state, $\Lambda_{p\mathrm{Ar}}$; and the muon capture rate onto argon, Λ_{Ar}. It is the extraction of these latter three rates that is the goal of the analysis of the decay electron time spectrum. In this chapter we will cover the physics effects to be considered in this analysis and the resulting corrections and errors for each of these rates.

The systematic effects in the decay electron time spectrum fall into three categories. The first are atomic physics effects associated with the formation of, or muon decay from, the μAr state. The systematic corrections and errors due to these effects are determined by previous measurements, calculations, and simulation. The muon kinetics involving hydrogen must also be taken into account: which includes the singlet μp capture rate; the effect of the ortho-molecular state evolving to the para-molecular state; and the reduced rate of proton capture in the molecular states. The rates of these processes are determined by previous measurements. The 0.23 ppm concentration of both oxygen and nitrogen (indicated by the chromatography analysis of the argon-doped hydrogen gas) means that atomic impurities are a source of error. Finally, a detector timing calibration uncertainty is applied. These effects are determined from measurement and simulation, and lead to a physics result that is well understood.

4.1 Atomic Physics Effects

4.1.1 Prompt μAr Formation

A muon stopping in the hydrogen gas can directly form a μAr atom on a time scale of 10 ns, without having undergone transfer to argon from the dominant μp singlet state. Prompt μAr formation is the first of several extensions to our initial model of the muon kinetics to be implemented in the fit to the decay electron time spectrum. The probability of a muon stopping directly on argon f_d is described with

$$f_d = \frac{2\mathrm{c}_{\mathrm{Ar}}}{A(\mathrm{H}_2, \mathrm{Ar})}, \tag{4.1}$$

where $\mathrm{c}_{\mathrm{Ar}} = 19.6(1.1)$ ppm is the atomic concentration of argon and $A(\mathrm{H}_2, \mathrm{Ar})$ is the relative probability of a muon stopping on a hydrogen molecule compared to an argon atom. As the muon slows to stop an argon atom is a larger and more attractive target than a hydrogen atom. The probability of direct μAr formation is not the statistical probability of the muon finding an argon atom in the gas[1] ($2\mathrm{c}_{\mathrm{Ar}}$), but greater because of this attraction. A previous experiment [53] measured $A(\mathrm{H}_2, \mathrm{Ar})$ to be 0.21(2) in a hydrogen gas at 15 bar pressure doped with 0.03% (atomic) argon. That result is assumed to be independent of the gas pressure and the concentration of argon. The predicted fraction of direct μAr stop events at the MuCap experimental condition of 10 bar pressure is $f_d = 1.87(20) \times 10^{-4}$.

Prompt μAr formation also occurs through excited-state transfer of the muon to argon

[1]The factor of 2 in Eq. 4.1 is due to the fact that hydrogen is a diatomic molecule, where as argon is monatomic. This scales as the number density of argon atoms, N_{Ar}, divided by the number density of hydrogen molecules, N_{H_2}, which is 2 times greater than its atomic concentration c_{Ar}, such that

$$\frac{N_{\mathrm{Ar}}}{N_{\mathrm{H}_2}} = 2\mathrm{c}_{\mathrm{Ar}}$$

.

during the μp cascade, involving an additional fraction of events f_e where

$$f_e = F_{\rm e}\frac{2c_{\rm Ar}}{A(H_2, {\rm Ar})} = F_{\rm e} f_d, \tag{4.2}$$

and $F_{\rm e}$ is the ratio of the number of excited-state transfer events to the number of events with a direct muon stop on argon. A stopping muon nominally enters the $n \approx 14$ principle quantum state of a μp atom and rapidly de-excites into lower n states in a cascade chain of physics processes, arriving in the $n = 1$ singlet ground-state on a time scale of 10 ns. The cascade physics includes fast radiative transitions driven by the Coulombic attraction of the muon and proton, and collisional interactions that result in the muon de-exciting to a more tightly bound (lower n) quantum state. The μp cascade physics is theoretically quantified [7,8]. The rates of collisional interactions, $\gamma_{\rm c}$, are proportional to the density of the hydrogen (such that $\gamma_{\rm c} \propto \phi$), whereas the rate of radiative de-excitation, $\gamma_{\rm r}$, is independent of the gas density. Excited-state transfer is a collisional interaction in competition with the other μp cascade processes. The rate of excited-state transfer, $\gamma_{\rm e}$, is likewise density-dependent. The rates of these processes, moreover, vary with the quantum state (n) the muon is momentarily in as it cascades.

In the $n > 5$ principle quantum states of the μp atom, excited-state transfer is predominantly in competition with other collisional processes of the muon cascade. The relative probability, $r_{n>5}$, that a muon undergoes excited state-transfer from these states scales as

$$r_{n>5} \approx \gamma_{\rm e}/\gamma_{\rm c},$$

and is density-independent. From the $n > 5$ quantum states the relative probability of excited-state transfer occurring is the same at 10 bar pressure as for the published measurement [53] at 15 bar.

In the $n < 5$ quantum states excited-state transfer is in competition with radiative de-

excitation, the rate of which dominates in these states. The relative probability of excited-state transfer from these states scales as

$$r_{n<5} \approx \gamma_{\mathrm{e}}/\gamma_{\mathrm{r}} \propto \phi,$$

and is proportional to the gas density because γ_{r} is density-independent. From the $n < 5$ quantum states the relative probability of excited-state transfer is $\frac{2}{3}$ of that at 15 bar, because the 10 bar gas is $\frac{2}{3}$ as dense. It is not certain with what likelihood excited-state transfer occurs from each principle quantum state of the μp system.

Following from these physics considerations, the reported excited-state transfer ratio in reference [53] $F_{\mathrm{e}}(15\text{ bar}) = 1.99(39)$ cannot be assumed under the conditions of the MuCap experiment. At 10 bar, F_{e} could vary between the reported value to $\frac{1}{3}$ smaller. A $\frac{5}{6} \pm \frac{1}{6}$ correction is applied to cover the anticipated range of error, where

$$f_e = \left(\frac{5}{6} \pm \frac{1}{6}\right) F_{\mathrm{e}}(15\text{ bar}) f_d = 3.08(89) \times 10^{-4}. \tag{4.3}$$

Combined with the direct stopping contribution f_d, prompt μAr formation is predicted for a total

$$f = 4.95(99) \times 10^{-4} \tag{4.4}$$

fraction of events.

4.1.2 Bound Atomic State Effects

The relativistic bound-state orbit of the muon in the μAr atomic state is the source of two additional systematic effects in the decay electron time spectrum. The characteristics of muon decay from atomic states were evaluated in the 1960s by Huff [54] and Überall [55]. One effect is that the muon decay rate is reduced by a factor h relative to that of a free muon at rest. The fractional change in the decay rate $1 - h$ increases from a level of 1 ppm

for the μp atom to $\approx$ 1.5 % for the μAr analog. The reduced rate of decay is intuitively understood as a consequence of time dilation from the muon orbital motion. A phase-space suppression of the number of final states available in the decay of a muon from an atomic state [54] additionally contributes to this effect. Further effects considered in the work of Huff and Überall are due to the Coulomb field of the nucleus as well as its finite size, the latter inducing perturbations to the muon (and electron) wavefunction.

The energy spectrum of decay electrons is also affected in muon decay from μZ atoms, and was first predicted in 1951 by Porter and Primakoff [56]. In atomic states the decay electrons must overcome the nuclear Coulomb potential energy barrier as they stream away. The loss of energy due to that barrier is a dominant effect in the energy spectrum. Effects from phase-space suppression and time dilation appear as well. In the rest frame of a muonic atom the nucleus may acquire momentum in the complete decay kinematics. For this reason the maximally allowed energy of a decay electron increases in atomic states above the $m_\mu/2$ ($\approx$53 MeV) limit observed in the muon rest frame. The energy spectrum consequently acquires a distribution for energies above that rest-frame limit. Time dilation alone predicts decay electrons with an energy greater than the muon rest frame limit, which contributes to the distribution of events above $m_\mu/2$.

An analytical description of the energy spectrum of decay electrons from muon decay in atoms is offered by Johnson et al. [57]. The physics model assumed in that work includes time dilation, phase-space and Coulomb field effects, while dropping perturbations due to finite nuclear size. The latter represent a 1.0 %-level variation in the energy spectrum. The calculated (normalized) spectra for μp and μAr decay electrons from this model are shown in Figure 4.1, as well as that of free muon decay electrons. The spectra for the μp state (green) and free muon decays (red) are very similar; a fractional difference of $\approx 10^{-3}$ exists near $m_\mu/2$. In contrast, the spectrum of μAr state decay electrons (blue) illustrates the perturbations owing to the atomic state effects just described.

The practical concern is that the efficiency of detection may be lower for decay electrons

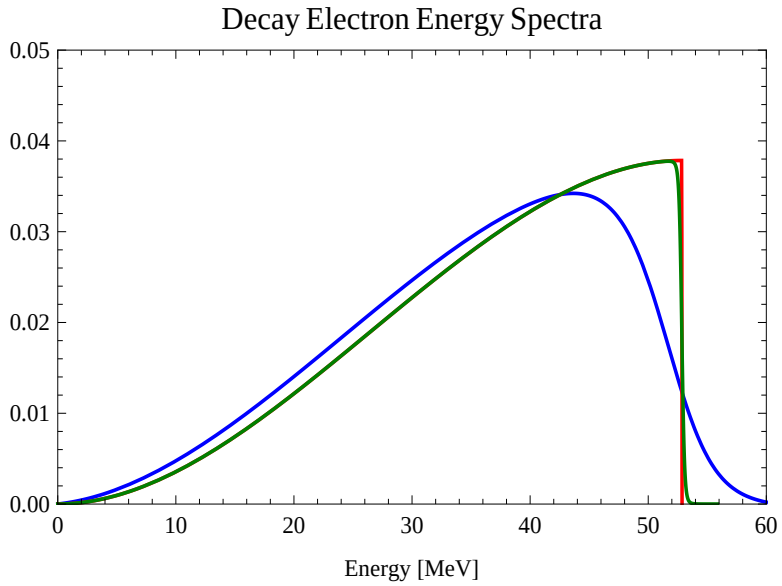

Figure 4.1: The calculated [57] probability of a muon decaying and producing an electron with a given energy (in MeV) is shown for muon decay from the μAr and μp states, displayed in blue and green respectively. The energy spectrum of electrons from the decay of free muons is shown by the curve in red.

emerging from the μAr state compared to the μp state. The relative efficiency e_{Ar} of decay electrons from the μAr state is used to correct for this effect in the fit to the decay electron time spectrum.

Watanabe et al. [58, 59] extended the work of Huff, Überall and Johnson et al. by evaluating the finite nuclear size effect perturbations more accurately. These perturbations increase with the Z value of the nucleus because the muon orbit is made smaller with the increased mass of the central nucleus. A non-uniform distribution of nuclear charge is additionally considered in this model. Recent experimental results from the TWIST collaboration [60] indicate that the energy spectrum of decay electrons from muons in a μAl state agrees with the calculations of Watanabe et al. for that system, which substantiates the importance of these effects for elements like argon[2].

[2]A recent calculation of these effects in μAl is presented by Czarnecki et al. [61]. That work is motivated by an interest in the highest energy (85 - 105 MeV) spectrum of decay electrons appearing with $10^{-8} - 10^{-20}$ probability, and focuses on the nuclear recoil effect. Such decay electrons are a background for experiments searching for $\mu \rightarrow e$ conversion; a signal of charged-lepton flavor violation and physics beyond the standard model.

The Muon Decay Rate Effect

Previous calculations facilitate an estimate of the μAr muon decay rate effect h. Computational results are available from the extended model of bound muon decay [58] for several atomic systems with Z values similar to argon, but not specifically argon. Calculated values of h utilizing the earlier model are tabulated in reference [18] for both the elements considered in reference [58] and argon.[3] The average difference between the two models for the selected μZ systems is taken as a correction to the μAr prediction from the earlier model. Applying such a correction ensures that the estimated value accounts for the effects included in the extended model, and the errors of the two models and calculation methods[4]. Using the results reported in Table 4.1 it is predicted that $h = 0.985(3)$.

[3]Reference [18] cites the original work of Huff for the calculated results tabulated in that paper. The error quoted for these calculations in the first column of Table 4.1 is as indicated by the original paper [54]. The error appearing in Table 4.1 for the (second) column of results from Watanabe et al. [59] is reported directly with those calculations.

[4]The results for the elements calcium and iron and oxygen indicate that the finite nuclear size effects are indeed significant compared to the errors for the two sets of calculations. The error assigned to h for argon estimate must cover the variation from the effects taken into account in the extended model and the two calculation methods, which a range of 0.003 achieves. The 0.003 error means that the estimated value for the μAr atom is consistent with the $h = 0.988$ result from the original model.

Table 4.1: Calculated values for the bound-state muon decay effect h in several μZ atoms. Results obtained from the original model of Huff [54] as tabulated in reference [18] and an extended [58] model including finite nuclear size effects are reported here in the first two columns of the table. The difference in the results of the two models is reported in the third column, which values are averaged and used to estimate an updated value for argon as explained in the text. The result for oxygen from the extended model is the only value obtained assuming a point like nucleus, as noted in the table.

Comparison of Results For the Bound Muon Decay Rate Effect			
Element (Z)	Original	Extended	Difference
Error	($\sigma \approx \pm 0.002$)	($\sigma < \pm 0.001$)	($\sigma \approx \pm 0.002$)
Oxygen (Z=8)	0.998	0.994 (point-like nucleus)	-0.004
Aluminum (Z=13)	0.993	0.992	-0.001
Silicon (Z=14)	0.992	0.991	-0.001
Argon (Z=18)	0.988	N/A	N/A
Calcium (Z=20)	0.985	0.981	-0.004
Iron (Z=26)	0.975	0.971	-0.004
Ave. Difference:			-0.003(2)
Argon Estimate:		0.988(2)-0.003(2)=0.985(3)	

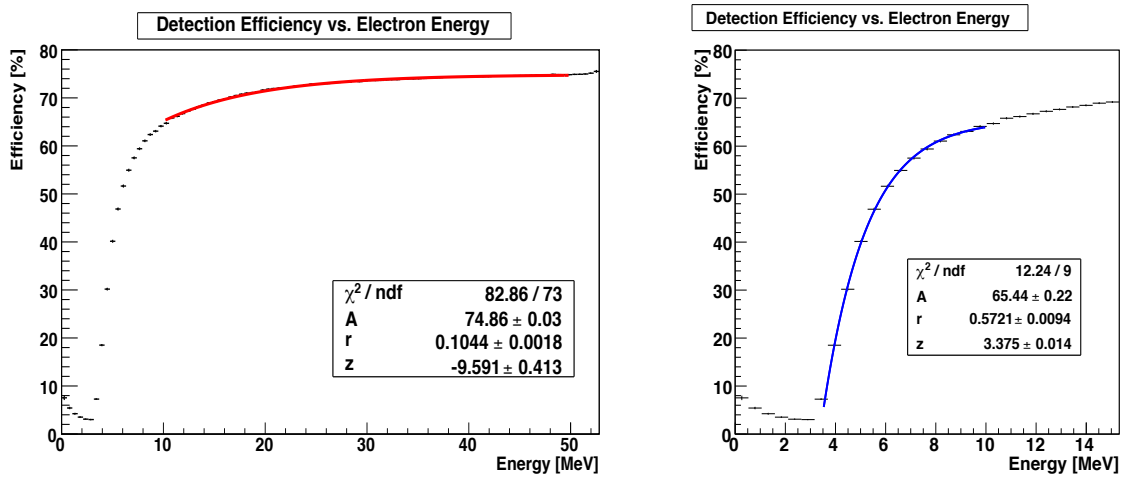

(a) Full range

(b) 0.0 - 15.0 MeV sub-range

Figure 4.2: Simulation results for the detector efficiency versus the energy of the decay electrons. The plot on the left shows the results of the simulation for energies up to $m_\mu/2$ in black. The fit to the curve between 10.0 and 50.0 MeV (red) is shown, with the numerical results reported in the lower-right corner of the plot. The fit function used to describe the curve is Eq. 4.5 defined in the text. To the right is a close up of the 0.0 - 15.0 MeV energy region of the same simulation results, with the fit result for energies between 3.5 and 10 MeV (blue) shown for comparison.

Decay Electron Detection Efficiency

Assessing the relative efficiency of the μAr decay electrons requires knowledge of the μAr and μp energy spectra, and the detection efficiency for electrons with energies between[5] 3.5 and 60.0 MeV. Simulation results [62] for the detector efficiency (black) are presented in Figure 4.2, which shows the probability that a decay electron with a given energy will be detected[6].

The detector efficiency is $\approx 70\%$ for electrons with energies between 10.0 and 50.0 MeV, yet shows definite variation. The largest variation in the efficiency is observed between 3.5 and 10.0 MeV in electron energy. Effects such as energy loss in detector materials dominate for electrons below 3.5 MeV in energy.

[5]Decay electrons with less than 3.5 MeV or more than than 60.0 MeV in energy are not produced from the μAr state in numbers that are statistically significant for this experiment. The range of 3.5 - 60.0 MeV is consequently practical for this work.

[6]The simulation results are from GEANT [63] models of the MuCap electron detector, and are provided by internal collaborators. [62] A series of 10^8 μ^- decay events are randomly generated in the simulation. The

Fits to the simulated efficiency curve are reported in Figure 4.2 for the 10.0 - 50.0 MeV (blue) and 3.5 - 10.0 MeV (red) energy regions. The detector efficiency $\epsilon(x)$ is empirically described by the fit function

$$\epsilon(x) = A(1 - e^{r(x-z)}), \tag{4.5}$$

where r and z parameterize the change with energy (x). The fit results for the 10.0 - 50.0 MeV region are reported in Figure 4.2a. For the 50.0 - 60.0 MeV energy range the 10.0 - 50.0 MeV fit result is applied up to the 60.0 MeV limit. Between 3.5 - 10.0 MeV the efficiency exhibits an empirically different variation and requires a separate fit. The detector efficiency $\epsilon(x)$ versus energy is consequently defined piece-wise between 3.5 - 60.0 MeV.

The relative efficiency of the μAr decay electrons e_{Ar} is calculated by

$$e_{\mathrm{Ar}} = \frac{\int_{3.5\ \mathrm{MeV}}^{60\ \mathrm{MeV}} \epsilon(x) s_{\mathrm{Ar}}(x) dx}{\int_{3.5\ \mathrm{MeV}}^{60\ \mathrm{MeV}} \epsilon(x) s_p(x) dx}, \tag{4.6}$$

where $s_{\mathrm{Ar}}(x)$ and $s_p(x)$ are the energy spectra previously shown in Figure 4.1 of the μAr state decay electrons [57]. The calculated result is $e_{\mathrm{Ar}} = 0.9956$. The two uncertainties to consider are the simulation of the detector efficiency $\epsilon(x)$ and the calculated energy spectra $s_{\mathrm{Ar}}(x)$ of the μAr state decay electrons.

The error to be assessed from the efficiency simulation is tested in two ways. Applying a 10% variation to the detector efficiency function (multiplying the $\epsilon(x)s(x)$ terms in Eq. 4.6 by $(1 \pm \frac{0.10}{60.00}x)$) produces a ± 0.0025 change in e_{Ar}. The same change in e_{Ar} results from varying the fit results by 10 σ of the errors. The value of 0.0025 is taken as an upper limit for the error due to the simulation.

The $s_{\mathrm{Ar}}(x)$ energy spectrum calculation follows from a model that does not assess finite nuclear size effects [57], which are a $\approx 1.0\%$ variation in the time spectrum.[7] The change in

probability of an electron being detected in the simulated detector is plotted versus the energy with which it appears from the decay event. The simulation includes the eSC and ePC electron detector components.

[7] This is verified by comparing the spectra of calcium ($Z = 20$) decay electron calculated from the extended model [58] and as calculated from the earlier, analytical, model [57]. The relative difference of the predicted spectra from these two models is $\approx 1.0\%$, being greater in the lowest (< 15.0 MeV) and highest (> 53.0 MeV)

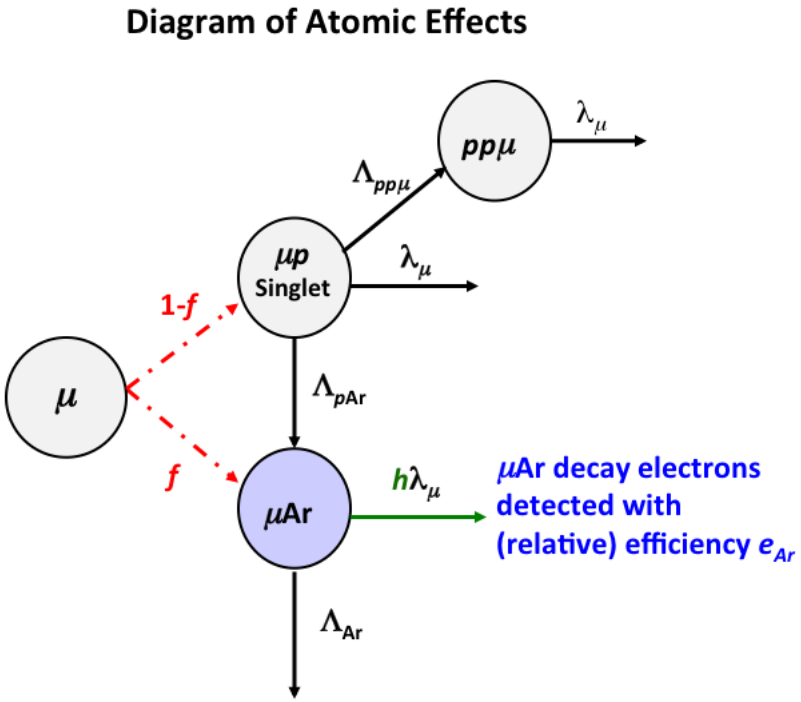

Figure 4.3: A diagram of the atomic physics effects in the argon-doped hydrogen gas. A muon may promptly form a μAr atom instead of the dominant μp state for a fraction f of events. This is highlighted above by the elements in red. The red arrows are dashed to indicate that they do not represent kinetic processes (i.e. rates) but the fractional probability of a muon forming the μp or μAr state. This occurs along with the processes of molecular formation ($\Lambda_{pp\mu}$), muon transfer ($\Lambda_{p\mathrm{Ar}}$) processes and capture onto argon (Λ_{Ar}) that are the focus of this analysis. The μAr muon decay rate effect h is represented by the elements in green, and the relative efficiency e_{Ar} is noted in blue. Previous measurements and calculations as well as detector simulation allow constraints to be placed on the quantities f, h and e_{Ar} as discussed in the text.

e_{Ar} from such a variation is 0.0005, which the 0.0025 overall uncertainty anticipates[8].

Each of the atomic physics effects produces a statistically significant correction to the $\Lambda_{pp\mu}$, $\Lambda_{p\mathrm{Ar}}$ and Λ_{Ar} results. It will be shown that these effects contribute minimally to the error of the measurement, introducing a combined systematic error that is less than 1/2 of the statistical error for each extracted rate. A diagram depicting these effects in the muon kinetics is shown in Figure 4.3.

energy regions.

[8]The μp decay electron energy spectrum is the same as the free muon decay spectrum to the level of 10^{-3}; no error is anticipated due to the model of s_p used for the calculation.

4.2 Extended Model of the Muon Kinetics and Description of the Decay Electron Time Spectrum

The second class of systematic effects is the muonic chemistry associated with hydrogen, which is not initially taken into account in the muon kinetics model of the argon- doped gas presented in Section 1.3.1. The most significant of these effects is the inclusion of the singlet capture rate Λ_S in the kinetics model. The value used for Λ_S is the theoretical prediction of 711.5 s^{-1}, which is used in calculating the final molecular state systematic corrections for the extraction of Λ_S as discussed in Section 1.1.4. The experimental error of 17.4 s^{-1} from the first results of the MuCap experiment [15] is used for assessing the systematic error due to this rate[9]. The remaining processes to take into account relate to the molecular states.

We first described the molecular processes in the argon-doped gas kinetics in approximation with a single formation rate $\Lambda_{pp\mu}$, and a single disappearance rate λ_μ. In the full extent of the muon hydrogen chemistry the transition rate $\lambda_{op} = 6.6(3.4) \times 10^4$ s^{-1} of the ortho-molecular state to the para-molecular state is not negligible. The direct formation of the para-molecular state is also not negligible. The effective rate of direct para-state formation is assumed to be $\Lambda_{pf} = 8.63(86) \times 10$ s^{-1}, which is determined from the theoretical prediction for the normalized rate $\lambda_{pf} = 7.5 \times 10^3$ s^{-1} and the gas density ($\phi = 0.0115(1)$). A 10% relative error is applied to λ_{pf}, which exceeds the $\approx 5\%$ relative error from the theoretical prediction for λ_{pf} [11], and the 1% relative error for ϕ.

The rates of muon capture on the proton from the ortho- and para- molecular states (Λ_O and Λ_P respectively), are distinct from Λ_S. The values $\Lambda_O = 541.4(13.1)$ s^{-1} and $\Lambda_P = 213.6(4.4)$ s^{-1} are determined by the theoretical value of Λ_S and the triplet state capture rate as introduced in Section 1.1.2. The errors for Λ_O and Λ_P are determined

[9]The theoretical value for Λ_S is within the experimental error of the first MuCap result. The effect of choosing either the experimental or theoretical value for Λ_S on the results of this analysis is an order of magnitude smaller than the statistical errors for the extracted rates. The significance of using either value will be shown by the systematic errors due to proton capture in Table 4.2.

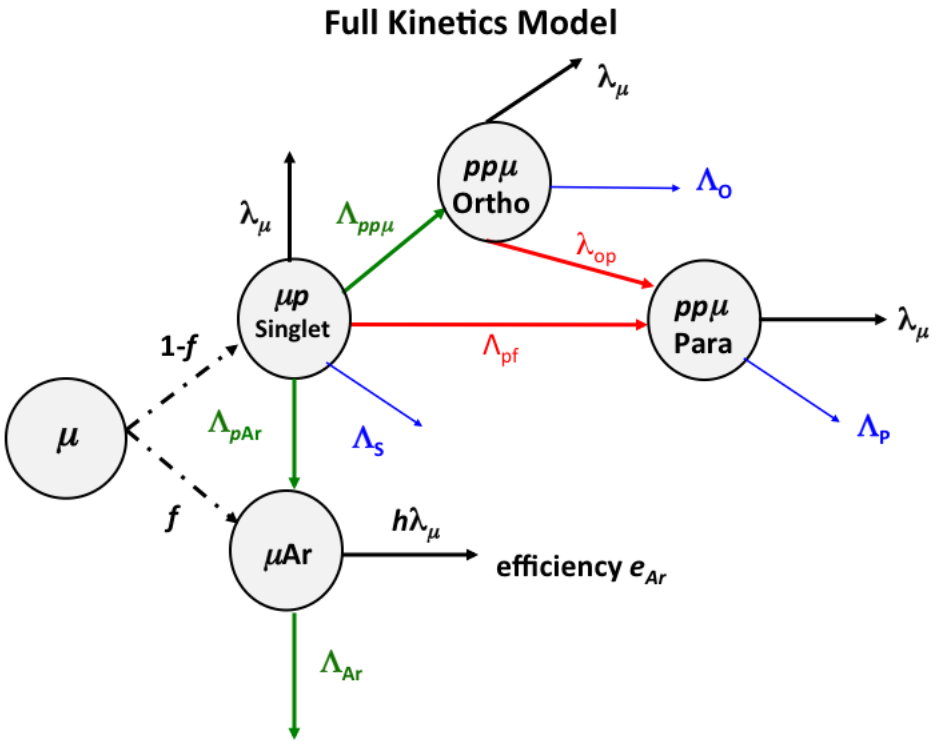

Figure 4.4: A diagram of the full model of muon kinetics and atomic physics effects implemented in the fit to the decay electron time spectrum. The atomic effects diagramed in Figure 4.3 are shown, as well as the hydrogen chemistry processes. The first of the latter is muon capture on the proton (Λ_S) (blue). The rate of the ortho–molecular state evolving to the para-molecular state λ_{op} (red) is included in the full kinetics model, as is the rate of para-molecular state formation from the μp state, Λ_{pf}. The rates of proton capture from the molecular states (Λ_O and Λ_P) are also noted (blue). The kinetic rates $\Lambda_{pp\mu}$, $\Lambda_{p\mathrm{Ar}}$ and Λ_{Ar}, which are the focus of this analysis, are highlighted in green.

from the experimental error in Λ_S from the first MuCap result[10]. It will be shown that the hydrogen state kinetics introduce sub-statistical systematic errors, but non-trivial corrections to the results of this analysis.

The complete model of the physics for the decay electron time spectrum analysis is depicted in Figure 4.4. The electron time spectrum analysis implements the complete muon kinetics in the fit function. The full model for the populations of the μp, μAr and molecular

[10]These errors follow from the approximations $\Lambda_O \approx \frac{3}{4}\Lambda_S$ and $\Lambda_P \approx \frac{1}{4}\Lambda_S$. The errors due to the molecular state effects for these rates are neglected.

states is shown in the following equations:

$$
\begin{aligned}
n'_{\mu p}(t) &= -(\lambda_\mu + \Lambda_{pp\mu} + \Lambda_{p\mathrm{Ar}} + \Lambda_\mathrm{S} + \Lambda_\mathrm{pf}) n_{\mu p}(t), && (4.7)\\
n'_{\mu\mathrm{Ar}}(t) &= \Lambda_{p\mathrm{Ar}} n_{\mu p}(t) - (h\lambda_\mu + \Lambda_\mathrm{Ar}) n_{\mu\mathrm{Ar}}(t), && (4.8)\\
n'_\mathrm{Ortho}(t) &= \Lambda_{pp\mu} n_{\mu p}(t) - (\lambda_\mu + \lambda_\mathrm{op} + \Lambda_\mathrm{O}) n_\mathrm{Ortho}(t), && (4.9)\\
n'_\mathrm{Para}(t) &= \Lambda_\mathrm{pf} n_{\mu p}(t) + \lambda_\mathrm{op} n_\mathrm{Ortho}(t) - (\lambda_\mu + \Lambda_\mathrm{P}) n_\mathrm{Para}(t). && (4.10)
\end{aligned}
$$

The variables $n_\mathrm{Ortho}(t)$ and $n_\mathrm{Para}(t)$ represent the time-dependent population of the ortho- and para-molecular states[11]; e_Ar, f and h are the atomic physics parameters; and the hydrogen-related kinetic rates λ_op, Λ_pf, Λ_S, Λ_O and Λ_P are included. The initial conditions for this system of equations are

$$
\begin{aligned}
n_{\mu p}(t=0) &= 1 - f\\
\text{and } n_{\mu\mathrm{Ar}}(t=0) &= f,\\
\text{where } n_\mathrm{Ortho}(t=0) &= 0\\
\text{and } n_\mathrm{Para}(t=0) &= 0.
\end{aligned}
$$

The physical time distribution of decay electrons, $n_e^{\mathrm{Phy.,Ar}}(t)$, and capture neutrons, $n_n^{\mathrm{Phy.,Ar}}(t)$, events in the argon-doped gas are defined as

$$
n_e^{\mathrm{Phy.,Ar}}(t) = \lambda_\mu \left(n_{\mu p}(t) + n_\mathrm{Para}(t) + n_\mathrm{Ortho}(t) \right) + h\lambda_\mu n_{\mu\mathrm{Ar}}(t) \qquad (4.11)
$$

and

$$
n_n^{\mathrm{Phy.,Ar}}(t) = \Lambda_\mathrm{S} n_{\mu p}(t) + \Lambda_\mathrm{O} n_\mathrm{Ortho}(t) + \Lambda_\mathrm{P} n_\mathrm{Para}(t) + \Lambda_\mathrm{Ar} n_{\mu\mathrm{Ar}}(t), \qquad (4.12)
$$

respectively. The disappearance rates of the μp and μAr states, $r_{\mu p}$ and $r_{\mu\mathrm{Ar}}$ respectively,

[11] The variables $n_{\mu p}(t)$, $n_{\mu\mathrm{Ar}}(t)$ are likewise the time-dependent population functions for the μp and μAr states as first defined.

are expressed as

$$r_{\mu p} = \lambda_\mu + \Lambda_{pp\mu} + \Lambda_{p\mathrm{Ar}} + \Lambda_{\mathrm{S}} + \Lambda_{\mathrm{pf}} \tag{4.13}$$

and

$$r_{\mu\mathrm{Ar}} = h\lambda_\mu + \Lambda_{\mathrm{Ar}}. \tag{4.14}$$

These are notably the rates of interest in the analysis of the capture neutron time spectrum, which will be discussed in Chapter 6.

The observed electron time spectrum, however, is still subject to the relative efficiency of the μAr state decay electrons, and in full is expressed as

$$n_e^{\mathrm{Obs.,Ar}}(t) = \lambda_\mu \left(n_{\mu p}(t) + n_{\mathrm{Para}}(t) + n_{\mathrm{Ortho}}(t)\right) + e_{\mathrm{Ar}} h\lambda_\mu n_{\mu\mathrm{Ar}}(t). \tag{4.15}$$

The relative efficiency e_{Ar} affects the relative contribution of $n_{\mu\mathrm{Ar}}(t)$ in the time spectrum of decay electrons. Prompt μAr formation, f, and theμAr decay rate parameter h affect the time spectrum in a similar way. In contrast the hydrogen kinetics rates directly affect the time-dependence of the μp, μAr and ortho- and para-molecular state populations.

The expression for $n_e^{\mathrm{Obs.,Ar}}(t)$ represents the full description of the decay electron time spectrum for this analysis. The practical fit function additionally assigns a free amplitude A and constant background B to the time spectrum, as in

$$A \cdot n_e^{\mathrm{Obs.,Ar}}(t) + B.$$

The fit has five free parameters $\Lambda_{pp\mu}$, $\Lambda_{p\mathrm{Ar}}$, Λ_{Ar}, A and B; where the muon decay rate λ_μ is fixed as are the parameters implementing the atomic physics and hydrogen kinetics systematic corrections. Implementing those systematic corrections in the fit function is motivated by the correlation and non-linearity of the kinetic rates in the time spectrum, which makes linear extrapolation methods insufficient for this analysis. Applying corrections in this way reflects a priority to extract information as directly from the data as possible.

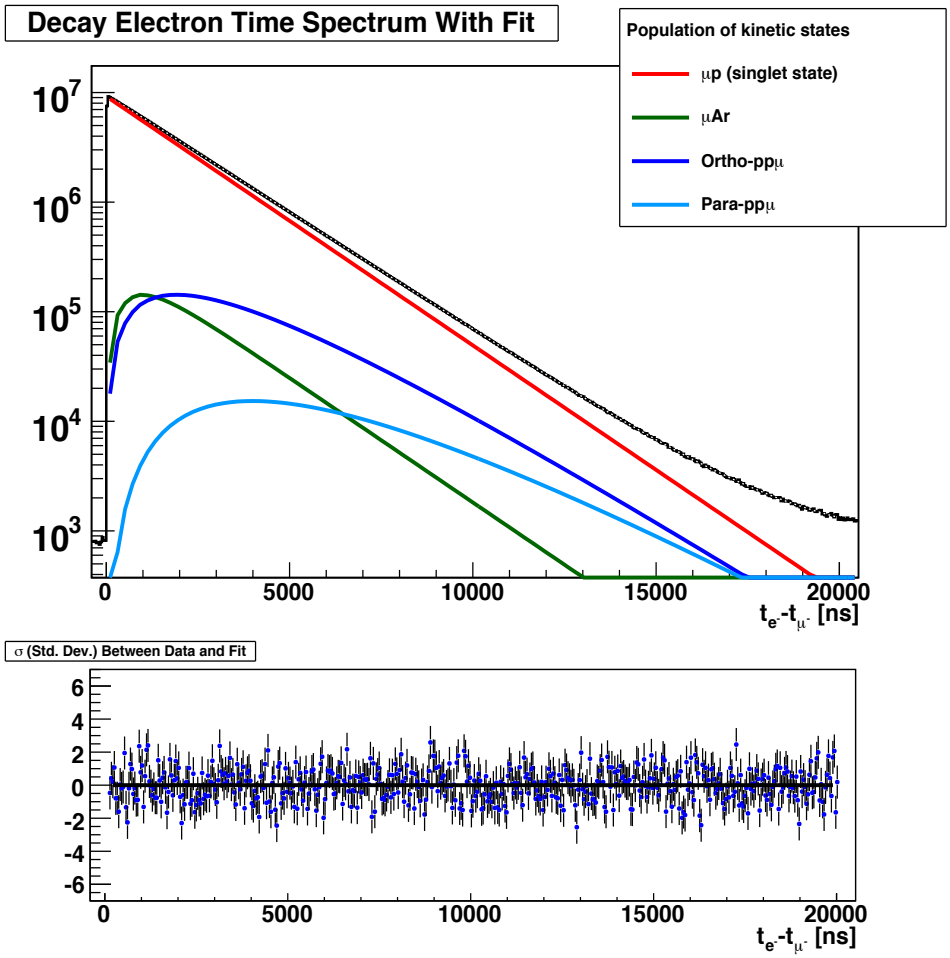

Figure 4.5: Upper Panel: Fit to the decay electron time spectrum data implementing the full model of the muon chemistry and atomic physics effects in the time spectrum shown in Figure 4.4 and Eq. 4.15. The curves in color depict the time-dependent populations of the kinetic states. The lower panel of this figure reports the level of agreement between the data and the fit function (i.e. a pull plot) in the 120 - 20000 ns time window.

The fit to the data is illustrated in Figure 4.5. The upper panel of this figure shows the decay electron time spectrum (black). The associated population time distributions $n_{\mu p}(t)$, $n_{\mu \mathrm{Ar}}(t)$, $n_{\mathrm{Ortho}}(t)$ and $n_{\mathrm{Para}}(t)$ are each shown. In the lower panel of Figure 4.5 the significance of the difference between the data and the fitted function is shown in units of sigma of the data histogram (the "pull plot" of the fit) for the 120 - 20000 ns time window. The agreement of the data with the fit function shown by this plot is demonstrated further by a normalized χ^2/Ndf of 0.983(64). The fitted results for the kinetic rates are $\Lambda_{pp\mu} = 2.208(62) \times 10^4$ s^{-1}, $\Lambda_{p\mathrm{Ar}} = 4.529(15) \times 10^4$ s^{-1} and $\Lambda_{\mathrm{Ar}} = 1.302(14) \times 10^6$ s^{-1}.

A final systematic effect is implemented in the fit to the data. The spectrum of decay electron events includes multiple exponential terms with different time-constants. Calibrating the time-of-arrival of the decay electrons is required to precisely determine the contribution of each term in the time spectrum. A 2.0 ns uncertainty in that calibration is a source of error to the fit results[12]. Each e^{-rt} term is implemented as $e^{-r(t-t_0)}$ in the fit function. The systematic errors for this effect are determined by the change in the fit results when t_0 is varied by $\pm$2.0 ns.

4.3 Oxygen Impurity Correction

Any $Z > 1$ element in the target gas represents a potential channel of transfer from the singlet μp state (and subsequent capture) for the muon. In the context of these data explicit use of this is made with the 18.5 ppm (atomic) concentration of argon. The presence of other $Z > 1$ elements in the gas represents additional perturbations to the decay electron time spectrum. The most prevalent impurity elements for the MuCap experiment are oxygen and nitrogen, which both enter via outgassing from the vessel wall of the TPC target detector.

[12]This calibration is assessed from fits to the first $\approx$50 ns of the time spectrum with 1.25 ns binning. In this limit the data appears as an error-function transition, and the average time of arrival t_0 and spread in the time of arrival can be obtained. The variation of the timing calibration is checked for stability versus the eSC segment associated with the electron hit, and eight chronological sub-groups of the data. The observed level of variation in the timing calibration has an upper limit of 2.0 ns.

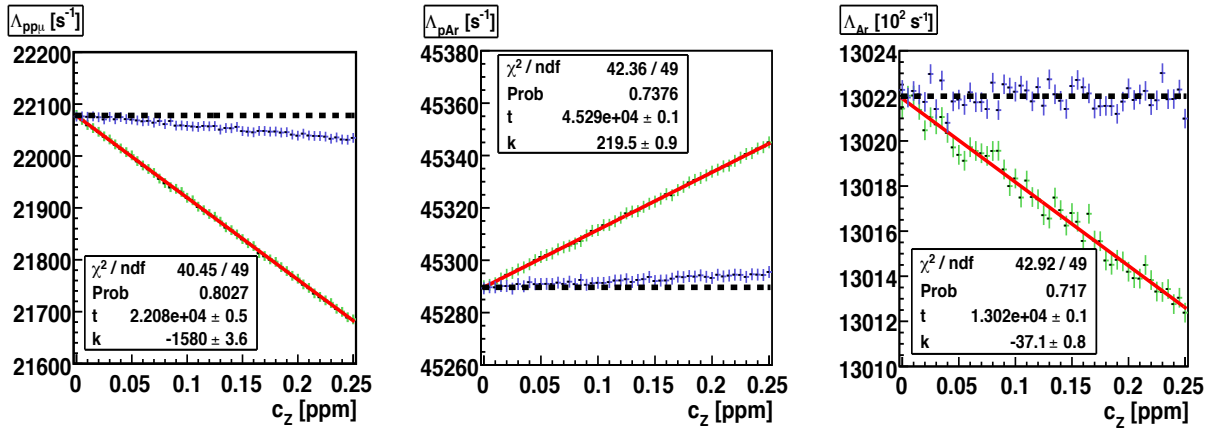

Figure 4.6: Fit results of a Monte Carlo simulation to determine the systematic effect of 0.0 - 0.25 ppm of oxygen and nitrogen in the target gas. Pseudo-data histograms of the electron time distribution are generated assuming the full model of the muon kinetics, as well as the effect of oxygen and nitrogen impurities. The fit results illustrate the effect of oxygen (green) and nitrogen (blue) for each of the extracted rates. A linear ($t + kc_Z$) fit (red) to the oxygen simulation points (and the numerical results) are shown in each panel. In the two left-most panels the error bars for the simulated $\Lambda_{pp\mu}$ and $\Lambda_{p\mathrm{Ar}}$ fit results appear enlarged by a factor or five, to better illustrate the fit to the data. The truth values of the simulation for $\Lambda_{pp\mu}$, $\Lambda_{p\mathrm{Ar}}$ and Λ_{Ar} are shown by the dotted lines black.

These elements are of sufficient mass ($Z = 7$ and 8 for nitrogen and oxygen respectively) that trace (< 1.0 ppm) concentrations represent potentially significant distortions in the time spectrum. Gas chromatography analysis of the argon-doped gas indicates 0.23 ppm of both oxygen and nitrogen at the end of the measurement period[13].

A Monte Carlo simulation is performed to evaluate the effects in the electron time spectrum due to oxygen and nitrogen impurities. The simulation physics includes the full muon kinetics of the argon-doped hydrogen gas as described to this point, as well as muon transfer to and capture onto oxygen and nitrogen. A series of 51 pseudo-data histograms of hypo-

[13]The measured concentrations of oxygen and nitrogen are larger than those obtained in the analysis of the pure hydrogen target gas. In that experiment these elements are continuously cleaned from the gas by the circulating gas purification system, CHUPS. The concentrations of these impurities are maintained at ≈ 0.01 ppm under those conditions; as demanded by the precision of that measurement. Argon is removed by the same purification system, which is counter to the design of this measurement. For this reason the TPC chamber vessel was taken out of circulation with the purification system while taking these data. Consequently a greater build-up of these impurity elements from outgassing was observed than in the pure hydrogen gas.

thetical decay electron time spectra are generated with the assumed concentration of oxygen, c_Z, varying between 0.00 and 0.25 ppm; a second series independently assesses the effect of nitrogen. The generated time spectra use the data fit results as truth values for $\Lambda_{pp\mu}$, $\Lambda_{p\mathrm{Ar}}$ and Λ_{Ar}. The analysis fit function is applied to the simulated data to test the variation in the fit results due to the gas impurity elements. The statistics of the simulation histograms are 10^5 times larger than the data sample (4.8×10^8) in order to statistically resolve this effect.

The simulation fit results are shown in Figure 4.6 for both oxygen (green) and nitrogen (blue). The linear variation of the fit results relative to the truth values of the simulation quantifies the systematic effect for each of the extracted rates. This is obtained for the oxygen (green) data with a linear ($t + kc_Z$) fit to each simulation curve, where k is the coefficient of variation and t is the y-axis intercept of the curve, which are also the truth values of the simulation. The linear fits to the oxygen simulation data (red), and the numerical results are likewise reported in each panel of Figure 4.6.

The kinetic rates assumed for oxygen and nitrogen are an input to this simulation and the values used are taken from previous experimental reports. The normalized transfer rate for nitrogen[14], $\lambda_{p\mathrm{N}}$, is 0.34×10^{11} s^{-1} [64]; and the rate of muon capture onto nitrogen, Λ_{N}, is 0.069×10^6 s^{-1} [18]. The reported value of the oxygen transfer rate, $\lambda_{p\mathrm{O}}$, is 0.85×10^{11} s^{-1} [65]. MuCap experimental efforts to measure $\lambda_{p\mathrm{O}}$ suggest this transfer rate could be twice as fast. A factor of 2 is applied to this value to estimate the full potential significance of this effect. The transfer rates dominate the linear variation of the fit results with c_Z, and priority is given to not underestimate the values chosen. The oxygen capture rate, Λ_{O}, is 0.102×10^6 s^{-1} [18].

In Figure 4.6 the simulated variation of the fit results due to nitrogen is significantly smaller than that due to oxygen, which follows from the fact that the muon transfer rate for

[14]Recall that the effective rate of transfer from the μp state to a μZ state will be

$$\Lambda_{pZ} = c_Z \cdot \phi \cdot \lambda_{pZ},$$

where ϕ is the density of the hydrogen gas relative to liquid hydrogen which has been assumed to 0.0115(1).

nitrogen is slower than for oxygen. Assessing the systematic effect oxygen alone is sufficient for each of the extracted rates. The coefficient of variation k of each of the kinetic rates and the concentration of oxygen c_Z determines the systematic correction Δ to be applied for each rate, where $\Delta = k \cdot c_Z$. The oxygen concentration is estimated to be $c_Z = 0.12(11)$ ppm.[15] The systematic corrections for the $\Lambda_{pp\mu}$ and $\Lambda_{p\mathrm{Ar}}$ kinetics rates are (191 ± 175) s^{-1} and (-27 ± 24) s^{-1} respectively. These corrections are smaller than the statistical error of either rate, 618 s^{-1} and 150 s^{-1} respectively. The argon capture rate, Λ_{Ar}, is sufficiently insensitive to this effect that any systematic correction is neglected.

[15]The concentration of oxygen may have increased during or appeared at the beginning of the measurement period. Contamination from air in the gas sample or in the sample analysis is not excluded from a single measurement and method. Determining the average concentration of oxygen from data is difficult because it represents a sub-statistical effect in the time spectrum. The concentration of oxygen during the measurement could vary between the 0.01 ppm concentration of the pure protium gas and the observed 0.230 ppm, i.e. $c_Z = 0.12(11)$ ppm.

4.4 Electron Time Spectrum Analysis Results

Table 4.2 reports the magnitude of each systematic correction, Δ, and corresponding error, σ, applied to the $\Lambda_{pp\mu}$, $\Lambda_{p\mathrm{Ar}}$ and Λ_{Ar} results. The first row of the table reports the analysis fit results, and statistical errors, and is emphasized with double lines. The entries in italics emphasize corrections applied in the fit function (See Eq. 4.15). The values reported for these corrections (Δ) are the change in the results when each systematic effect is independently included or dropped from the fit function. The reported errors for these effects (σ) are likewise determined by the change in the fit results when each systematic parameter is independently varied by its known error. The oxygen impurity correction is the only systematic effect not incorporated into the fit to the data, but applied as a separate correction. The systematic corrections and errors applied to the fit results are shown in the row labeled "Total", and the final physics results appear at the bottom of Table 4.2 (emphasized with double lines).

For $\Lambda_{pp\mu}$ the μAr decay rate effect, prompt μAr formation, and the oxygen impurity in the gas each result in a correction with a magnitude $\approx$1/3 of the statistical error. The largest correction to $\Lambda_{pp\mu}$ is for the effect of proton capture, and is similar in magnitude to the statistical error. The reported corrections and errors in Table 4.2 for this effect include the contributions of proton capture from the ortho- and para-molecular states.[16] The effect of proton capture induces the largest correction to the $\Lambda_{p\mathrm{Ar}}$ transfer rate and Λ_{Ar} capture rate results. The systematic correction to $\Lambda_{p\mathrm{Ar}}$ due to proton capture is notably the most significant in this analysis, $\approx 4\ \sigma$ of the statistical error.

For each of the extracted rates, none of the systematic errors in Table 4.2 are greater than $\approx$1/3 of the statistical error. The final physics results are dominated by the statistical errors

[16] The Λ_{O} and Λ_{P} molecular state capture rates are parameterized in terms of the Λ_{S} capture rate in the fit function (as introduced in Section 1.1.2). The systematic error due to proton capture is the change in the fit results when Λ_{S} is varied by 17.4 s^{-1}, and Λ_{O} and Λ_{P} are simultaneously varied in assessing this error. The reported corrections likewise represent the change in the fit results when Λ_{S} is varied from 0 to 711.5 s^{-1}, with the molecular state capture rates simultaneously changed.

Table 4.2: Table of systematic corrections (Δ) and errors (σ) for the $\Lambda_{pp\mu}$, $\Lambda_{p\mathrm{Ar}}$ and Λ_{Ar} results of the electron time spectrum analysis. The first and final rows of the table report the fitted and final physics results for comparison, and are emphasized with double lines. The second to last row of the table reports the total systematic error and correction applied to the fit results of each of the extracted rates. Note: The values in italics emphasize systematic corrections (Δ) due to effects taken into account in the fit function (Eq. 4.15), which are not applied externally to the results in the first row as explained in the text.

Table of Systematic Corrections and Errors						
Rate	$\Lambda_{pp\mu}$ [s^{-1}]		$\Lambda_{p\mathrm{Ar}}$ [s^{-1}]		Λ_{Ar} [10^2 s^{-1}]	
Fit result	22078	619	45290	150	13022	142
	Δ	σ	Δ	σ	Δ	σ
Timing calibration		39		13		35
Relative efficiency: e_{Ar}	*63*	37	*21*	13	*-61*	34
Atomic decay rate: h	*218*	45	*73*	15	*-141*	27
Prompt μAr formation: f	*221*	46	*60*	12	*-202*	39
Proton capture: Λ_{S}, (Λ_{O}, Λ_{P})	*611*	13	*-628*	16	*-220*	5
Ortho-para transition: λ_{op}	*-75*	31	*-8*	3	*5*	2
Direct para-state formation: Λ_{pf}	*-87*	9				
Oxygen impurity correction	191	175	-27	24		
Total	+191	198	-27	39	n/a	68
Final result	22269	650	45263	155	13022	157

of the fit. The significance of the statistical errors to these results motivates an examination of the fit procedure, and more so because of the correlated and non-linear features of the time spectrum.

4.5 Examining the Fit to Data

The fit is done with a χ^2 map method [66] intended for challenging fits with correlated parameters. Table 4.3 reports the normalized correlation coefficients from the covariance matrix of the fit to the data. Although the correlations shown in Table 4.3 are significant, the fit result is interpretable and reproducible.

The correlation of the fit parameters is interpretable with the formalism that the covariance matrix, C_{ij}, for a generic fit function $f(t)$ with parameters p_i is equal to the inverse of

Table 4.3: Table of normalized correlation coefficients of the free parameters in the electron time spectrum fit.

Table of Correlation Coefficients				
Rates	$\Lambda_{pp\mu}$	$\Lambda_{p\mathrm{Ar}}$	Λ_{Ar}	A
$\Lambda_{p\mathrm{Ar}}$	0.9548	...	...	...
Λ_{Ar}	-0.8021	-0.9011	...	...
A	0.0495	0.0269	0.0234	...
B	-0.6603	-0.5479	0.4189	-0.1082

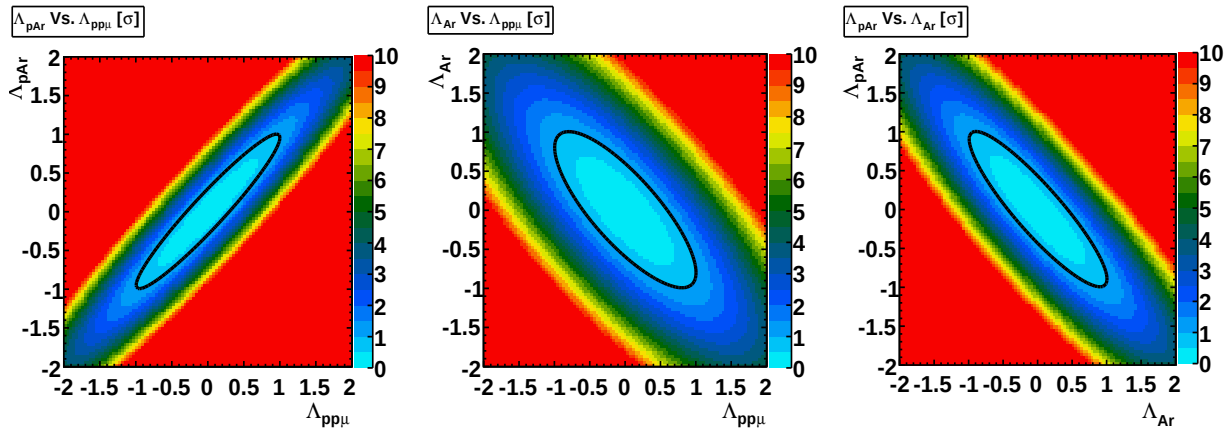

Figure 4.7: The variation of the χ^2 (relative to the minimum value χ^2_{min}) is plotted here in each two dimensional plane of the $\Lambda_{pp\mu}$, $\Lambda_{p\mathrm{Ar}}$ and Λ_{Ar} parameter space. For clarity the horizontal and vertical axes have been labeled in units of standard deviations of the reported errors of the fit to data. This assists in illustrating the significance of the variation of the χ^2 as presented here. The $\chi^2 - \chi^2_{\mathrm{min}} = 1$ is also shown for comparison (black).

the matrix S_{ij} where the elements of S_{ij} are calculated by the following

$$S_{ij} = \int_{t_{\mathrm{Start}}}^{t_{\mathrm{Stop}}} \frac{\left(\frac{df}{dp_i}(t)\right)\left(\frac{df}{dp_j}(t)\right)}{f(t)}\, dt,$$

and where t_{Start} and t_{Stop} represent the range of t in which the fit is applied. This is analytically descriptive of the correlations between the fit parameters and how the fit uncertainty takes them into account.

The variation of the χ^2 in the $\Lambda_{pp\mu}$, $\Lambda_{p\mathrm{Ar}}$ and Λ_{Ar} parameter space also illustrates the fit. Figure 4.7 plots the variation of the χ^2, relative to the minimum value χ^2_{min}, in each

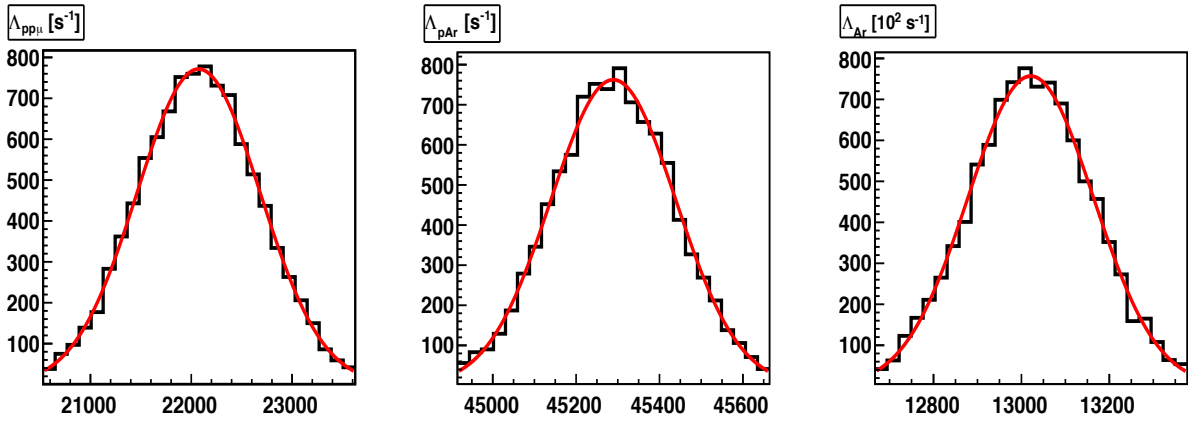

Figure 4.8: The distribution of results (black) from fits to 10^4 pseudo-data histograms is show here for the $\Lambda_{pp\mu}$, $\Lambda_{p\mathrm{Ar}}$ and Λ_{Ar} rates. Each histogram is randomly generated from the fit function of the data. A gaussian fit is applied to the distributions of the fit results (red), where the resulting mean and width agree favorably with the data.

two-dimensional plane of this parameter space. Each point in the two-dimensional plots shows the relative change in the χ^2 determined from a fit with two kinetic rates fixed to the indicated values in the range of ± 2 σ of the fit errors of each rate, with the remaining parameters of the fit function varying. The $\chi^2 - \chi^2_{\mathrm{min}} = 1$ contour (black) is consistent with the 1.0 σ range of the fit errors. These plots depict the correlations of the kinetic rates, which are consistent with the values shown Table 4.3, and show that the variation of the χ^2 is controlled in this parameter space.

The reproducibility of the results is demonstrated in a simulation of 10^4 pseudo-data histograms generated from the data fit function, with the statistics as the summed data histogram. The distributions of the $\Lambda_{pp\mu}$, $\Lambda_{p\mathrm{Ar}}$ and Λ_{Ar} results from fits to the pseudo-data are shown in Figure 4.8. Each distribution is plotted for the range of values 2 sigma of the errors in the fit to data. Gaussian fits (red), provide values for the mean and width of the simulated distributions. The values obtained from the gaussian fits are reported in Table 4.4, and are consistent with the the data fit results in the first row of Table 4.2. The agreement of the simulation and data fit results highlights the reproducibility of the statistical errors, which the final errors of $\Lambda_{pp\mu}$, $\Lambda_{p\mathrm{Ar}}$ and Λ_{Ar} are dominated by.

Table 4.4: Results of the gaussian fits to the distribution of pseudo-data fit results shown in Figure 4.8. The fitted χ^2/Ndf, mean and width of each distribution are reported for the three simulated distributions. The mean and width of the $\Lambda_{pp\mu}$ and $\Lambda_{p\mathrm{Ar}}$ distributions are shown in units of s^{-1}, and $\times 10^2$ s^{-1} for Λ_{Ar}.

Table of Gaussian Fit Results			
Rates	χ^2/Ndf	Mean	Width
$\Lambda_{pp\mu}$	12.86/23	22072.8(6.4)	612.1(5.3)
$\Lambda_{p\mathrm{Ar}}$	26.38/23	45289.3(1.6)	149.9(1.3)
Λ_{Ar}	33.23/23	13021.1(1.5)	143.2(1.3)

4.6 Disappearance Rate Results

The results of this analysis can be understood in the context of the effective disappearance rates of the μp and μAr states, $r_{\mu p}$ and $r_{\mu\mathrm{Ar}}$ respectively. These rates are determined to be

$$r_{\mu p} = 0.52350(80) \times 10^6 \ \mathrm{s}^{-1} \text{ and}$$

$$r_{\mu\mathrm{Ar}} = 1.750(16) \times 10^6 \ \mathrm{s}^{-1},$$

respectively[17], following from Equations 4.13 and 4.14.

The results of the decay electron time spectrum analysis is a significant contribution to the world knowledge of the molecular formation rate, and also of the muon transfer and capture rates for argon. The implications of these results in that context will be discussed in the concluding chapter of this work. The next chapter will discuss other consistency checks of the data to further examine the findings of the electron time spectrum analysis.

[17]The error $\sigma_{r_{\mu p}}$ reported for $r_{\mu p}$ follows from the correlated error of $\Lambda_{pp\mu} + \Lambda_{p\mathrm{Ar}}$ (see Eq. 4.13), where

$$\sigma^2_{r_{\mu p}} = \sigma^2_{\Lambda_{pp\mu}} + 2C_{\Lambda_{pp\mu},\Lambda_{p\mathrm{Ar}}}\sigma_{\Lambda_{pp\mu}}\sigma_{\Lambda_{p\mathrm{Ar}}} + \sigma^2_{\Lambda_{p\mathrm{Ar}}},$$

$\sigma_{\Lambda_{pp\mu}}$ and $\sigma_{\Lambda_{p\mathrm{Ar}}}$ are the final errors of $\Lambda_{pp\mu}$ and $\Lambda_{p\mathrm{Ar}}$ reported in Table 4.2, and $C_{\Lambda_{pp\mu},\Lambda_{p\mathrm{Ar}}}$ is the normalized $\Lambda_{pp\mu} : \Lambda_{p\mathrm{Ar}}$ correlation coefficient shown in Table 4.3. The error for $r_{\mu\mathrm{Ar}}$ follows from the final error of Λ_{Ar} in Table 4.2, and the uncertainty in h as motivated by Eq. 4.14.

Chapter 5

The Decay Electron Time Spectrum Analysis: Consistency Studies

The previous chapter discussed the systematic effects accounted for in the decay electron time spectrum analysis, and the extracted $\Lambda_{pp\mu}$, $\Lambda_{p\mathrm{Ar}}$ and Λ_{Ar} results. Additional studies will be presented in this chapter to demonstrate the consistency of the results for sub-groups of the full data set. The systematic effects considered in this chapter relate to the selection of events and time-dependent distortions in the decay electron time spectrum.

The first of these studies is the fit start- and stop-time scans, which test for sensitivity to distortions in the data that are larger than statistically probable. The remaining studies examine the stability of the selection criteria for the muon decay events. The variation of the time spectrum fit results is examined versus the vertical (y) and longitudinal (z) coordinates of the muon stop location in the TPC. Those studies test the stability of the fiducial volume cuts applied to the muon stop location. The variation of the time spectrum fit results versus which eSC segment the observed electron hit is found, is examined. This procedure checks the stability of the event timing and geometric acceptance of events. The impact parameter cut, which is applied to the electron track and muon stop location, is tested. A final study is made of the consistency of the results for eight chronological sub-groups of the data.

5.1 Start- and Stop-time Consistency of Fit

The variation of the fit results with start- and stop-time is sensitive to time-dependent distortions in the data. The standard fit range for this analysis is 120 - 20000 ns. When the start-time is set to a later time (or stop-time set to an earlier time) a correlated statistical

subset of the data is selected. If the statistical error of a fit parameter p is $\sigma_{\rm F}$, and $\sigma_{\rm S}$ for a sub-set of data, the allowed 1 σ limit of variation for p relative to the full-statistics result is

$$\sqrt{\sigma_{\rm S}^2 - \sigma_{\rm F}^2}.$$

The variation of each fit parameter with start- or stop-time can be compared to this statistical limit. The χ^2/Ndf should also be stable with the change of statistical sub-set included in the fit.

The start-time scan of the decay electron time spectrum fit is shown in Figure 5.1. The fit start-time is scanned from 120 to 3200 ns while the 20000 ns stop-time is kept constant. The amplitude and background constants are fixed to the values obtained from the 120 - 20000 ns fit with those parameters freely varying for the results reported here. The fit results for $\Lambda_{pp\mu}$, $\Lambda_{p\rm Ar}$ and $\Lambda_{\rm Ar}$ (black) are shown against the 1.0 standard deviation (σ) statistical limit of variation (red) for each parameter in the three panels of Figure 5.1(a). The variation of the central values of the fit (blue) is within statistically allowed limits for each of the kinetic rates. The stability of these results substantiates the 120 ns start-time for this analysis. The presence of statistically-significant distortions in the time spectrum not accounted for in the fit function is found to be improbable. The consistency of the χ^2/Ndf shown in Figure 5.1(b) is also favorable.

The fit stop-time scan is presented in Figure 5.2. The stop-time is varied between 14000 and 20000 ns, with the 120 ns start-time kept constant. The variation of the kinetics rate fit results and the χ^2/Ndf shown here is again shown to be statistically consistent. The stability of the results out to 20000 ns illustrates that the chosen stop-time is appropriate for this analysis. The stop-time scan results demonstrate the stability of the background and pileup suppression criteria implemented in the event selection. Any time-dependent distortion in the background due to pileup events or instability in the muon beam on the time-scale of this measurement is shown to be statistically improbable. The start- and stop-

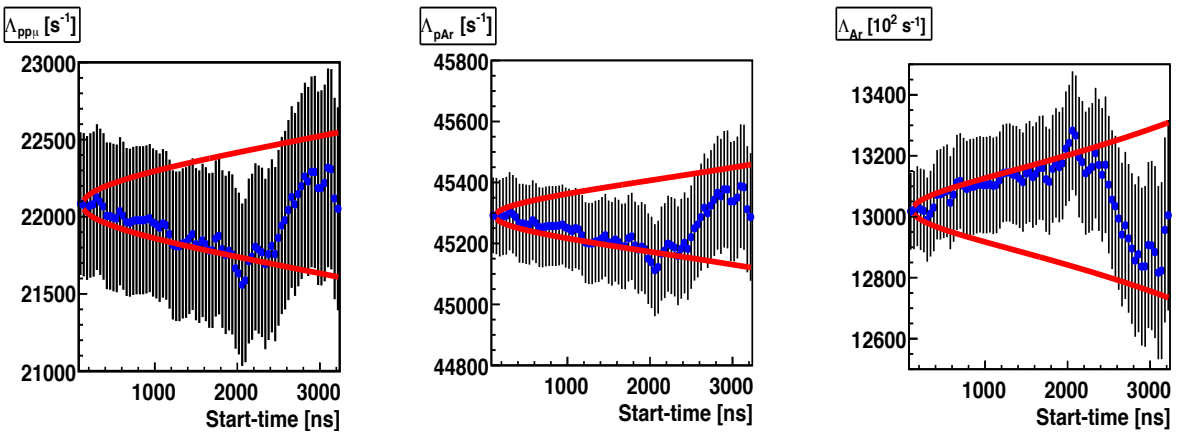

(a) $\Lambda_{pp\mu}$, $\Lambda_{p\mathrm{Ar}}$ and Λ_{Ar}

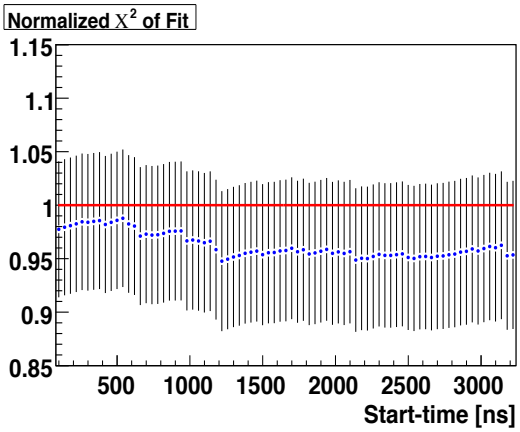

(b) χ^2/Ndf

Figure 5.1: The start-time scan fit results (black), with the stop-time fixed to 20000 ns. Figure 5.1(a) shows the kinetic rate fit results (black) in three panels. The variation of the central values (blue) is shown compared to the 1 σ. statistical limit of variation (red) for each rate. Figure 5.1(b) plots the χ^2/Ndf (blue) of each fit (blue), compared to a χ^2/Ndf of 1.0 (red). The amplitude and background constants are fixed to the values obtained from the 120 - 20000 ns fit with these parameters freely varying to obtain the results reported here.

time studies indicate that that systematic issues relating to the selection of events are not a source of instability for the results of this analysis. The following studies will do that more explicitly.

5.2 Muon Stop Location

The consistency of the fit results with the muon stop location in the TPC is a check of the stability of the fiducial volume cut. Figure 5.3 shows the fit results for the data as sorted by the z coordinate of the muon stop location. The first bin at left in each panel of the figure represents the fit to the full data set, which here represents the selected events that meet the fiducial volume and other criteria described in Section 3.1.2. A constant-line fit (red) tests the variation of the $\Lambda_{pp\mu}$, $\Lambda_{p\mathrm{Ar}}$ and Λ_{Ar} fit results, which is shown here to be within statistical limits for each rate. The z coordinate is also associated with the anode wire on which the muon stop is observed. The anode wire gain and efficiency can vary by $\approx 10\%$ [67], providing a source of instability to the event read-out and selection, and subsequent distortion to the time spectrum. The statistical agreement of the fit results shown in Figure 5.3 shows that such a distortion is not statistically significant.

The scan of fit results versus the vertical (y) coordinate of the muon stop is shown in Figure 5.4. The same procedure for quantifying the variation of the $\Lambda_{pp\mu}$, $\Lambda_{p\mathrm{Ar}}$ and Λ_{Ar} results for sub-groups of the full data set with constant-line fits is applied here as in the previous figure. The variation of the fit results is within statistical limits for the y coordinate of the muon stop location as well. The consistency of the fit results in the y coordinate is not only of interest to test the stability of the fiducial volume cut, however. The higher the muon stop location is in the TPC the longer the deposited charge takes to reach the bottom wire chamber plane, potentially affecting the threshold discrimination and read out of the event. The results of Figure 5.4 show that such an effect is statistically improbable and the muon stop selection criteria are stable.

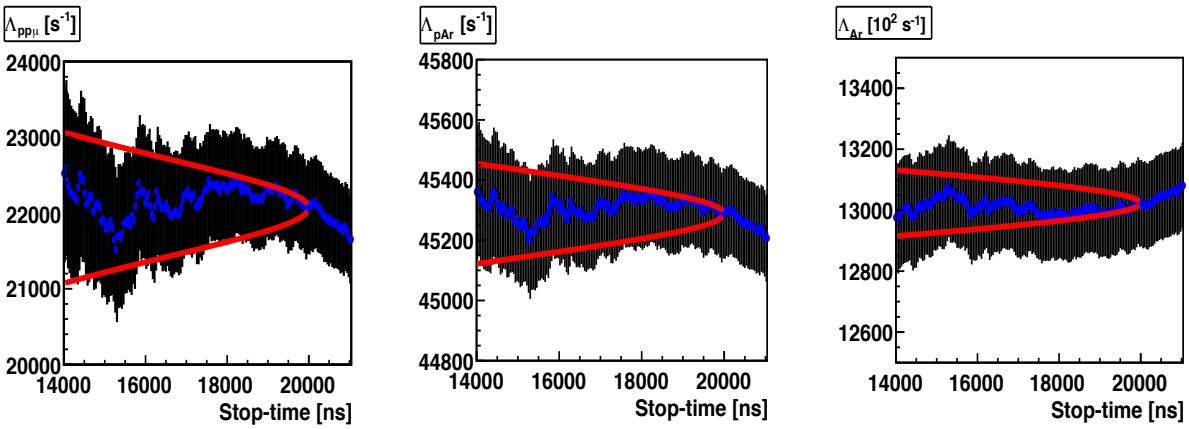

(a) $\Lambda_{pp\mu}$, $\Lambda_{p\mathrm{Ar}}$ and Λ_{Ar}

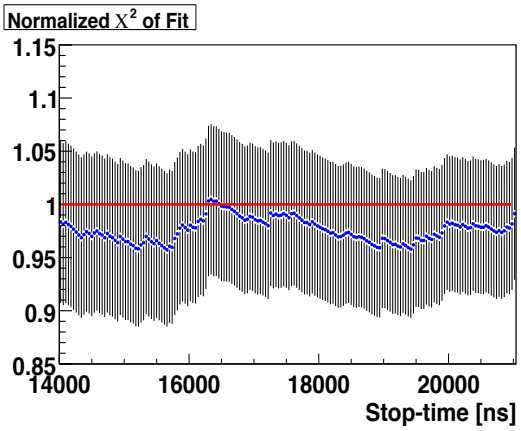

(b) χ^2/Ndf

Figure 5.2: The electron time spectrum stop-time scan (black) is shown for start-time fixed to 120 ns. Figure 5.2(a) shows the kinetic rate fit results in three panels. The variation of the central value of the fit (blue) results is shown compared to the 1 σ statistical limit of variation (red) for each rate. Figure 5.2(b) plots the χ^2/Ndf (blue) of each fit (blue), compared to a χ^2/Ndf of 1.0 (red). The amplitude and background constants are not fixed in the fits reported here.

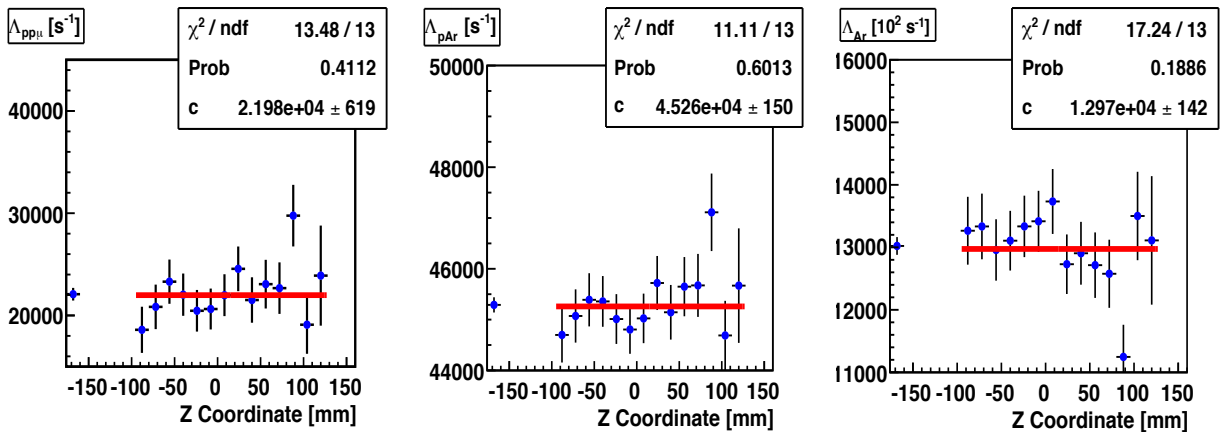

Figure 5.3: The time spectrum fit results for the data as sorted by the z coordinate of the muon stop in the TPC. The data is sorted into 14 sub-groups, corresponding to 16 mm ranges along the z axis of the detector, where 0 mm represents the center of the detector. The sorted sub-groups each correspond to a set of four contiguous anodes of the wire chamber. The fit results of $\Lambda_{pp\mu}$, $\Lambda_{p\mathrm{Ar}}$ and Λ_{Ar} are plotted in the three panels shown here. The first bin at the left in each panel (at -170 mm) represents the fit to the full statistics time spectrum. Constant-line fits (red) to the kinetic rate results test if the variation of the time spectrum is consistent with statistics. The χ^2, probability of agreement and average value c obtained from the constant-line fits are reported in each panel.

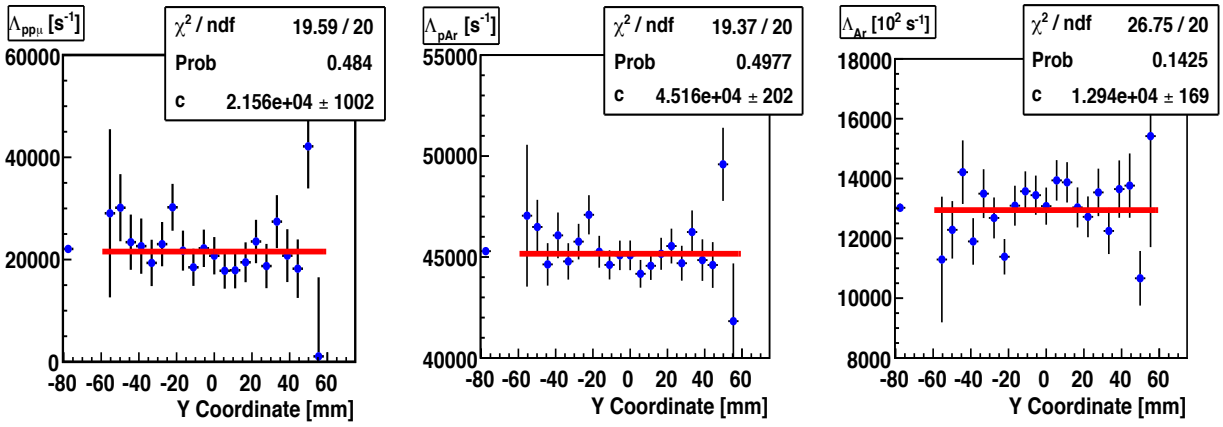

Figure 5.4: The $\Lambda_{pp\mu}$, $\Lambda_{p\mathrm{Ar}}$ and Λ_{Ar} fit results shown for the data as sorted into 21 sub-groups by the vertical y coordinate of the muon stop location in the TPC, corresponding to ranges of $\approx$5.7 mm in the vertical axis, where 0 mm represents the vertical center of the TPC and the elevation of the muon beam. The fit results of the three kinetic rates are plotted in three panels. The first bin at the left (-80 mm) of each plot represents the fit to the full data set. Constant-line fits (red) test if the observed variation of the fit results is consistent with statistics.

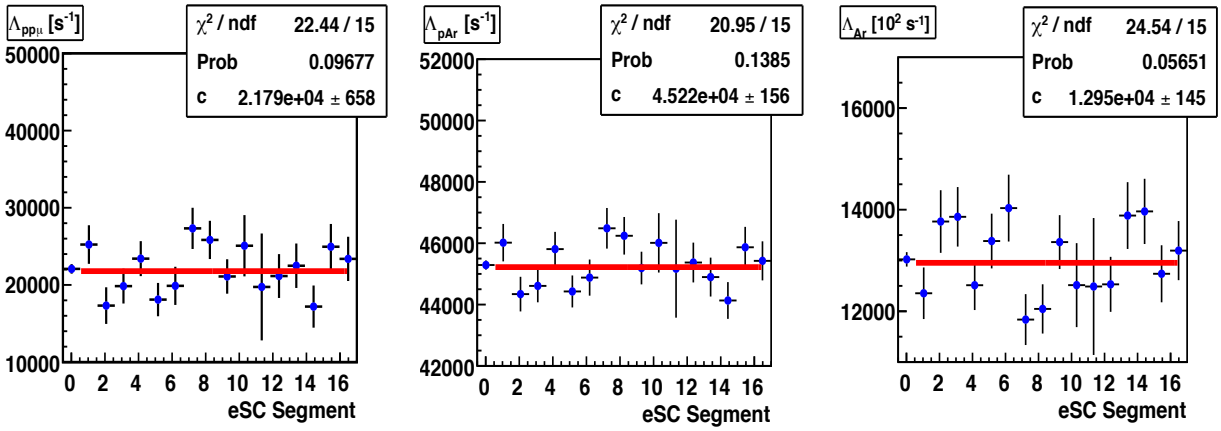

Figure 5.5: The $\Lambda_{pp\mu}$, $\Lambda_{p\mathrm{Ar}}$ and Λ_{Ar} fit results to the data sorted by the segment of the eSC in which the electron hit is found. The kinetic rate results are plotted versus eSC segment number in three panels. The first bin at the left in each panel represents the fit to the full data set. A constant-line fit (red) quantifies the variation in the kinetic rate results in each panel. The results of the constant-line fits are likewise reported in each panel.

The stability of the fit results in Figures 5.3 and 5.4 show that the applied fiducial volume cuts are appropriate for this analysis. No distortions to the time spectrum associated with the muon stop location are indicated for events within the fiducial volume of the TPC. Additional documentation for the stability of the fiducial volume cut is available in reference [37], as presented for the higher-statistics analysis of the pure hydrogen data set.

5.3 Electron Track Timing and Geometry

The electron timing is determined by the eSC hodoscope detector, and variation in the 16 segments of the eSC is a potential source of systematic distortion in the data. Figure 5.5 shows the fit results sorted by the segment of the eSC in which the coincident electron hit is found. The variation of the fit results versus eSC segment additionally tests the stability of the time spectrum with respect to the angle of emission for the decay electron in the transverse plane of the TPC; i.e., the plane of cylindrical symmetry of the electron detector.

The variation of the fit results versus eSC segment shown in Figure 5.5 is higher than in any other consistency studies. The lowest probability of statistical agreement shown here

is $\approx 1/20$ for the Λ_{Ar} capture rate results, which is an improbable but allowable result. The variation of the results shown in Figure 5.5 is not considered a systematic effect of concern for this analysis. The reason for this can be explained by first describing the physical explanations for this effect.

The track of an electron emitted in the downward direction leaves a line of ionized charge beneath the muon stop in the TPC. Interference causes the charge deposition from the muon stop to have an increased density as observed in the wire chamber, due to the ionization induced by the electron. The analysis requires at least one anode excited in an event to exhibit a pixel at the EH energy threshold. Electron track interference can promote a muon stop event to meet the EH threshold condition in a time-dependent way, where the same event would otherwise be cut from the analysis. The time-dependence appears because the ionization induced by the electron track is increasingly spatially separated from that of the muon stop the later in time the decay occurs, which makes the promotion of an event less likely. The time-dependent bias to select muon events that have been affected by interference leads to a distortion in the data. The electron-track interference effect is furthermore asymmetric in the transverse plane of the TPC, because the emitted electron is moving downward from the location of the muon stop in such events, and correlates to a distortion of the time spectrum versus eSC segment.

Events of $\mu + p$ scattering in the target gas can be erroneously selected as fiducial muon stops in the analysis. An event of this kind may be accepted if sufficient charge is deposited near the location of the scatter to excite the EH energy threshold in the wire chamber below. (The electron hit being either due to background or the muon itself.) The probability of such events being promoted into the analysis is subject to charge interference, being greater if the scattered muon moves in the downward direction.

The electron-track interference and scattering effects are highlighted by events in which the muon stop exhibits a single continuous anode excited at the EH energy threshold; i. e., those events most susceptible to being promoted into the analysis due to interference.

A comparison of the fit results when including or excluding these events shows a relative change that is 10^{-3} or smaller, which is statistically negligible for this analysis. Interference effects are consequently not considered a systematic concern for this analysis, and the same conclusion is applied to the variation of results shown in Figure 5.5.

5.4 Electron Track Impact Parameter Cut

A study of the 120.0 mm impact parameter cut is motivated by the observation of μp diffusion in the target gas. Once formed the μp atom may diffuse macroscopic distances in the hydrogen gas on the time scale of 1000 ns before muon decay occurs. The diffusion constant of μp atoms in the hydrogen target gas has been measured internally to be $k = 0.01552(23)$ mm/$\sqrt{\text{ns}}$ [51]. The consequence of diffusion is that the point of origin of the decay electron track may be displaced from the location of the muon stop in the TPC.

The impact parameter cut is applied to the distance of closest approach of the electron track to the muon stop location, which must be less than a maximum threshold value. This criterion removes background events where the observed electron is not causally connected with the stopped muon. In the limit of a very tight impact parameter cut of 10.0 mm, μp diffusion induces significant distortions in the time spectrum. Diffusion causes the μp atom to be more than 10.0 mm away from the muon stop location for a statistically significant fraction of events, and this is increasingly likely with time due to diffusion. The impact parameter cut rejects these events in a time-dependent way, inducing the said distortions in the time spectrum. The 120.0 mm impact parameter cut must also be checked for stability against such distortions.

A consistency scan of fit results versus the impact parameter cut applied is shown in Figure 5.6. The $\Lambda_{pp\mu}$, $\Lambda_{p\text{Ar}}$ and Λ_{Ar} fit results are reported for impact parameter cut thresholds between 10.0 mm and 150.0 mm. The right-most point of each plot represents the data with no impact parameter cut applied. The analysis result for the 120.0 mm cut (red) is

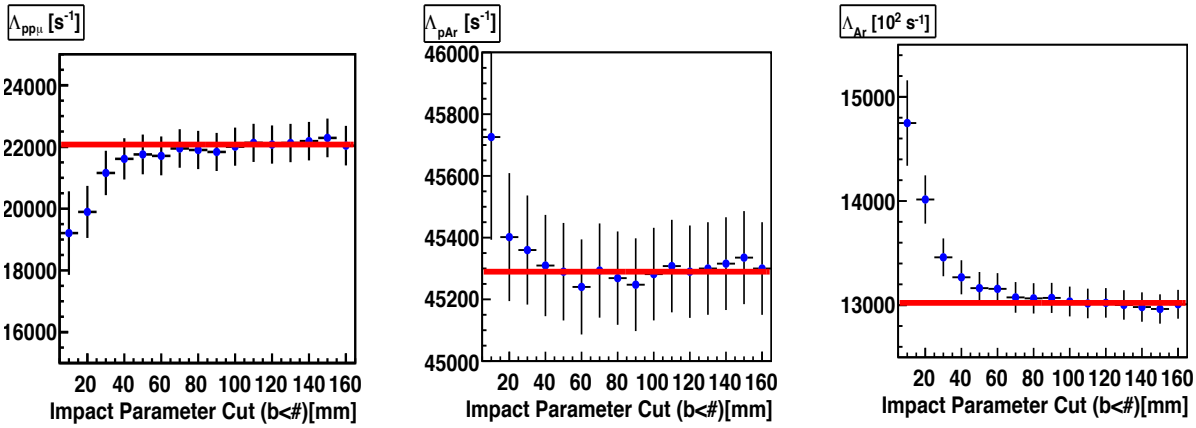

Figure 5.6: The fit results for the data with varying impact parameter cut threshold. In each panel the fit results are shown for threshold values between 10.0 and 150.0 mm; the rightmost bin at 160.0 mm represents the data with no impact parameter cut applied. The fit result for the 120.0 mm impact parameter cut condition is illustrated (red) for comparison.

highlighted for comparison. As the cut becomes more selective from 150.0 mm to 90.0 mm the fit results show no significant variation, illustrating that the 120.0 mm cut is stable. The fit results for more selective cuts ($<$ 80.0 mm) illustrate the anticipated variation of fit results due to distortions in the time spectrum connected with μp diffusion.

5.5 Chronological Subgroup

The final consistency check is to the data as sorted into 8 chronological sub-groups. Any changes in experimental conditions can manifest as a variation in the fit results over the measurement period. Figure 5.7 shows the results of such a consistency check. As in Figures 5.3 - 5.5 the consistency of the data results is tested with a constant-line fit (red). The variation of the $\Lambda_{pp\mu}$, $\Lambda_{p\mathrm{Ar}}$ and Λ_{Ar} results is shown to be within statistical limits. This is the final example of the consistency studies done in the course of this analysis. The work presented in this chapter illustrates the most important ways in which the consistency of the data is examined, and how well understood the measurement of the decay electron time spectrum is.

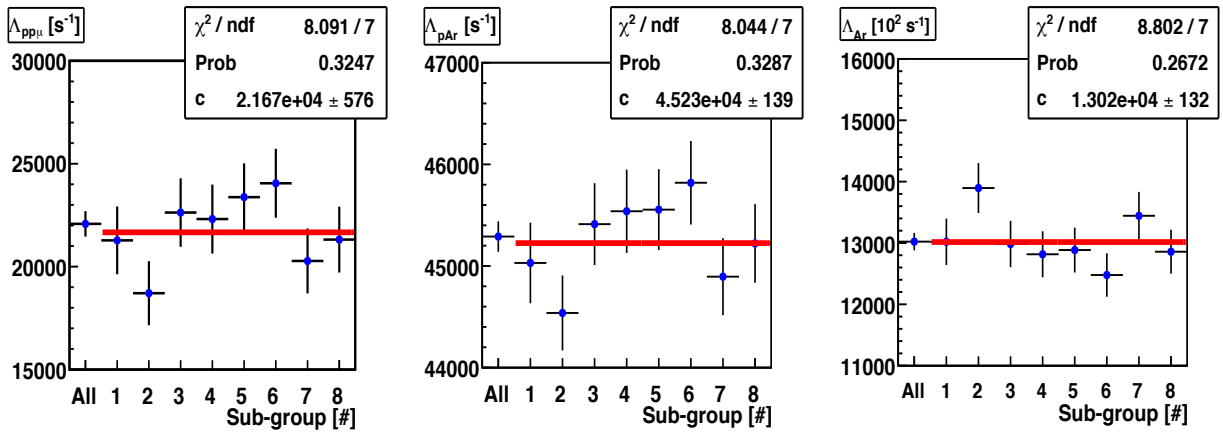

Figure 5.7: The $\Lambda_{pp\mu}$, $\Lambda_{p\mathrm{Ar}}$ and Λ_{Ar} fit results shown for the data as sorted into 8 chronological subgroups. The points in the left most bin of each panel represent the fit to the full data set, and results for each sub-group are shown in chronological order from left to right. The consistency of the data versus sub-group is again tested with a constant-line fit (red) to the results of each extracted kinematic rate.

Chapter 6

The Capture Neutron Time Spectrum Analysis

The goal of the analysis of the capture neutron time spectrum is the extraction of the μp and μAr state disappearance rates, $r_{\mu p}$ and $r_{\mu\mathrm{Ar}}$, respectively. The results of this analysis are an internal consistency check to those extracted from the decay electron time spectrum, which include determinations of $r_{\mu p}$ and $r_{\mu\mathrm{Ar}}$. This chapter will first discuss the systematic effects relevant to the neutron time spectrum analysis. The final $r_{\mu p}$ and $r_{\mu\mathrm{Ar}}$ results are presented in the concluding section, along with the status of the comparison with the results extracted from the decay electron time spectrum.

The systematic effects considered in this analysis include several that have already been discussed. The contribution of μp and ortho-molecular state capture events to the neutron time spectrum as well as prompt μAr formation are both considered. The kinetic rates and processes associated with the hydrogen states are reported in Section 4.2, and prompt μAr formation is discussed in Section 4.1.1. These corrections are applied in the fit function, as they were in the analysis of the decay electron time spectrum. Additionally, the systematic effect of the trace 0.12(11) ppm concentration of oxygen in the target gas is considered.

Additional systematic effects are unique to this analysis. The first of these is the time-dependent neutron background, which is correlated with the muon beam. The resulting distortion in the time spectrum is corrected from the data with a subtraction method. Another systematic concern in this analysis is charge interference induced by the capture process. Muon capture onto argon results in charge deposition in the TPC due to the recoiling product nucleus, and potentially due to charged particle emission as well, as discussed in Section 3.1.6. Such charge deposition is associated with interference effects for the data

analysis of muon stop events. Emitted charged particles, in particular, are a source of time-dependent bias in the selection of events, and consequently of distortion in the neutron time spectrum. A correction for this effect is based on a survey of capture events and applied from the data.

Two other systematic effects are due to the difference in the energies of neutrons emitted from the hydrogen and μAr states. The neutrons produced in muon capture onto argon are predominantly between 1.0 and 3.0 MeV in energy, and dominate the time spectrum. Capture from the hydrogen states produces mono-energetic 5.2 MeV neutrons, which are detected with greater efficiency than those from the μAr state. The difference in efficiency is in part a result of the non-linear response of the liquid scintillator detectors with neutron energy [44], along with other detector-related effects. The relative efficiency e_{H} for detecting the 5.2 MeV neutrons is determined from the yield of capture events in the pure hydrogen and the argon-doped gas data, and applied as a correction in the fit function.

The hydrogen state capture neutrons also have a shorter time-of-flight than the lower-energy neutrons produced in muon capture onto argon. The timing calibration and spread in the time-of-flight for both sources of neutrons is determined from data and detector geometry information. The timing calibration is implemented in the fit function as well.

The results of this analysis are subject to a complex series of systematic corrections. The magnitude of each effect is determined to support results for the $r_{\mu p}$ and $r_{\mu\mathrm{Ar}}$ disappearance rates that are comparable in precision to those extracted from the electron time spectrum. The final results will be shown to be a confirmation of the more precise results determined from the decay electron time spectrum analysis.

6.1 The Decay Electron Veto and Neutron Background

Identifying capture neutron events requires the discrimination of pulses induced by neutrons and gamma particles (discussed in Section 3.1.5), as well as a veto of decay electron events. Applying such a veto is motivated because a decay electron is inconsistent with a capture event, as both processes cannot occur for a single muon. A decay electron can additionally induce a pulse in the liquid-scintillator detectors that is potentially misidentified as a neutron signal. Moreover, the decay electrons have a different time spectrum than the capture neutrons and are produced in $\approx 93.0\%$ of all muon events entering the detector. For these reasons the decay electrons are a potential source of distortion in the neutron time spectrum, which further motivates vetoing such events in this analysis. As discussed in Section 3.1.6 a paired hit in the eSC scintillator detector within $0 - 20000$ ns of a muon entrance is interpreted as a decay electron signal and defines a veto condition applied for capture neutron events[1].

Neutron events with an electron hit found in the $0 - 20000$ ns time window after the same muon stop are additionally associated with cases where the observed neutron is from a background source. Two sources of background are considered, the first is random ambient neutrons that are not time-correlated with the muon stop events. The other source of background events is correlated with the muon beam and is time-dependent. Neutrons are produced in several beam processes, such as the stopping and subsequent capture of muons in the materials of beamline components. The kicked time structure of the beam allows for a neutron background to be generated that is correlated with a muon entrance into the experiment.

[1]The reverse concern does not apply to the decay electron time spectrum analysis. No electron events are rejected based on an identified neutron pulse. That analysis relies on time-coincident ePC wire chamber information for electron tracking. An electron signal cannot be induced by a capture event because the neutrons cannot trigger hits in the wire chambers.

Figure 6.1 depicts the vetoing of decay electron events and the neutron background. The histogram shown at the left in Figure 6.1(a) represents events where at least one neutron and one electron are observed in coincidence with the same muon stop. The time-correlation of neutrons and electrons is shown here in the $-1000 - 5000$ ns window with respect to the muon stop. The vertical and horizontal axes represent the time of the observed neutron and electron, respectively. Cases of a decay electron generating a pulse that is misidentified as a neutron signal are indicated by the prompt coincidence (-150$< t_e - t_n <$50 ns) peak that exists along the diagonal ("$x = y$") axis. The other distinguishing feature of this histogram is that the time spectrum of neutrons shows a "ledge" structure at ≈600 ns (in the vertical axis) away from the prompt coincidence peak, which illustrates the time-dependent background. The range of the statistical axis of the histogram (right) is set to emphasize the characteristics of the neutron background, and the prompt peak appears as a red line along the diagonal.

The time spectra of the background and the prompt-coincident events in the liquid scintillator detectors are shown in Figure 6.1(b). The events represented in these plots are the same as for Figure 6.1(a). Note the feature of the background time spectrum (red) at 600 ns, which emphasizes the time-dependent distortion introduced by such events. The spectrum of the prompt coincidence events (blue) is a monotonically decreasing distribution after $t_n - t_\mu = 0$, and indicates that these events are induced by decay electrons.

Beam-correlated Background Subtraction

The time spectrum of the background is defined by selecting electron-neutron coincidence events where $0< t_e - t_\mu <$20000 ns, and rejecting those meeting the prompt coincidence condition (-150$< t_e - t_n <$50 ns). The background time spectrum (red) is shown in Figure 6.2, and is most significant in the first 600 ns after the muon stop, where it has a clear time-dependent feature. The analysis time spectrum (blue) is subject to the $0 - 20000$ ns electron veto, but contains a component of the time-dependent background. The background contribution to that spectrum is illustrated by the distribution of events where the neutron

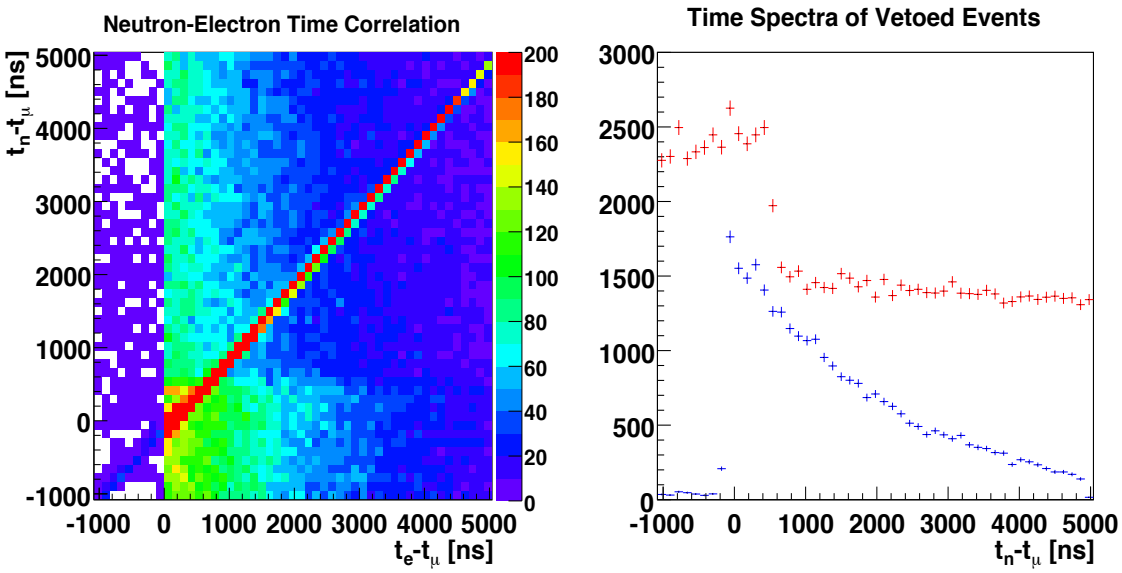

(a) Time Correlation

(b) Spectra of Vetoed Events

Figure 6.1: Right: A two-dimensional histogram of the neutron and electron time correlation relative to a muon stop. The vertical axis represents the time of a neutron relative to the coincident muon stop. The horizontal axis represents the time of an observed electron relative to the same muon stop. As discussed in the text, this histogram shows elements of structure that motivate the electron veto applied for the event selection of this analysis. The histogram also depicts the time-dependent neutron background, which is correlated with the muon beam and corrected for by a subtraction method. Left: The one-dimensional time spectra of the vetoed events separated into the neutron background (red) and prompt coincidence events (blue).

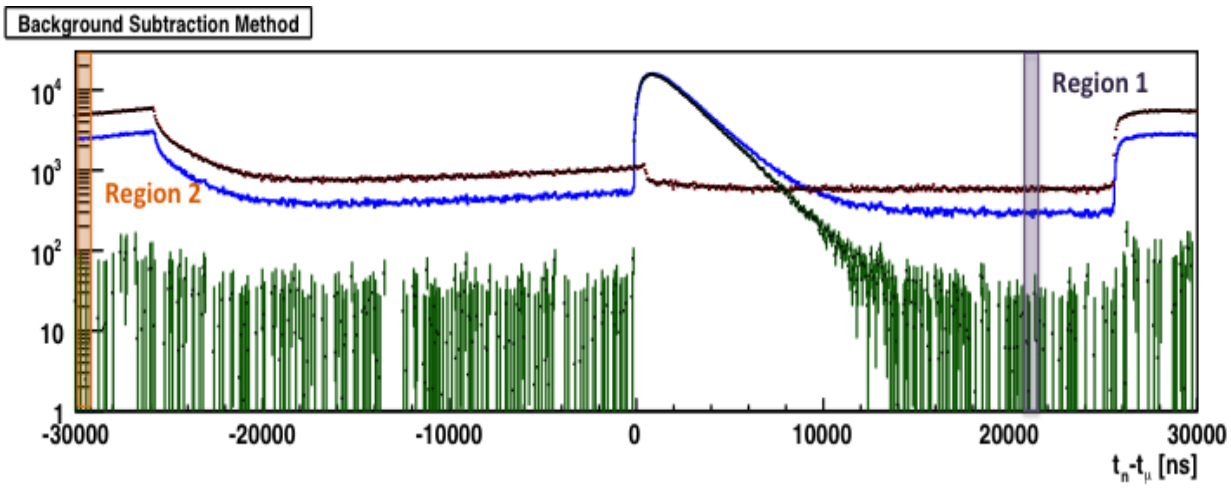

Figure 6.2: The time-dependent neutron background correction: The time spectrum of background neutrons (red) is shown here in the ±30000 ns time window relative to a muon stop. Although the analysis time spectrum (blue) has been subject to a veto of electron events it includes a component of the background as well, shown in the $t_n - t_\mu < 0$ time region of this plot. The fraction of the background (red) appearing in the analysis spectrum (blue) is determined by comparing the number of counts in two time regions (violet and orange) for both of these spectra. The corrected neutron time spectrum (green) is obtained after subtracting the background, as explained in the text.

has arrived before the muon (where $t_n - t_\mu < 0$ ns). The systematic distortion to the time spectrum is corrected for with a subtraction method [68].

Two time regions are defined to determine the normalized fraction k of the background (red) present in the analysis time spectrum[2] (blue), which are −24300 to −24000 ns and 21000 to 21300 ns as highlighted in Figure 6.2. The difference between the integral number of counts in each time region (I_1 and I_2 respectively) quantifies the background component of the analysis time spectrum. Taking the difference of the two integrals ($I_1 - I_2$) additionally removes the constant (flat) background from the comparison. The ratio of the values obtained from the analysis ($I_1^a - I_2^a$) and background ($I_1^b - I_2^b$) time spectra determines the fraction k, where

$$k = \frac{I_1^a - I_2^a}{I_1^b - I_2^b}.$$

[2]The analysis results are, however, found to be insensitive to the specific choice of the time range for region 2.

The background spectrum (red) is scaled by k, along with the statistical errors, and subtracted from the analysis spectrum. The systematic error due to the time-dependent background is accounted for in fits by the enlarged uncertainties of the corrected time spectrum (green in Figure 6.2). The integral statistics of that spectrum between 0 and 20000 ns is 8.3×10^5.

6.2 Charged Particle Emission Interference Correction

The process of muon capture onto argon results in charge deposition in the TPC, which leads to the possibility of interference with the charge deposition of the muon stop and the interpretation of events. A product nucleus is recoiled in muon capture onto a $Z > 1$ element. The recoiling nucleus induces a < 1200 ns pulse of ionization charge, which corresponds to a charge distribution with a vertical extent of < 7 mm in the TPC. An example of such an event is shown in Figure 3.4 as depicted in the MuCap TPC event display (introduced in Section 3.1.2). The majority of capture events in this analysis are of this type.

The second time-dependent effect in the neutron time spectrum is due to charged particle emission (CPE) in the process of muon capture onto argon. The product nucleus may be left in an unstable state following capture, and a proton or alpha particle may be emitted in the de-excitation process. CPE is observed for 5.90(33)% of capture events in the argon doped gas. The CPE process occurs simultaneously with the nuclear recoil and is an additional source of charge deposition in the TPC. The emitted particle can induce sufficient charge density in the hydrogen gas to excite the EL and EH threshold levels of the wire chamber, and potentially results in an independently identifiable track in the analysis of an event. A secondary track of this kind is a unique signature of CPE. The emitted particle can have sufficient energy to leave the fiducial volume of the detector and exit the TPC.

Interference between a CPE track and a muon stop is more likely at early times

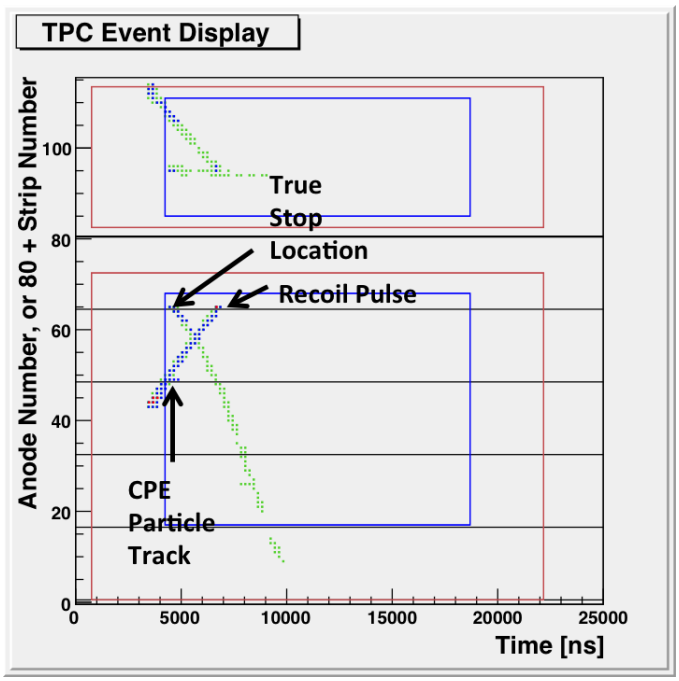

Figure 6.3: An example of a connected CPE capture event as displayed in the MuCap TPC event display. The horizontal axis represents time and y coordinate of the TPC, and the vertical axis represents the TDC read out of the anode wires (1-80), and cathode strips (81-115) in time. The "Track" and "Muon Stop" fiducial volumes, are also shown by line boxes (red and blue, respectively). The muon stop location, nuclear recoil pulse and CPE track are each noted. The connected CPE track leaves the fiducial volume (blue boxes) of the detector, which leads this event to be rejected in the analysis. The true location of the muon stop is within the fiducial volume for the stop location (blue), and without CPE interference this event would be accepted. Such an event represents the majority of the early-time, connected-CPE events that fail the standard analysis conditions for a muon stop.

($t_n - t_\mu < 1000$ ns) than at later times. In such events the charge deposition of the emitted particle and the muon stop is connected (contiguous). The probability that one of these events is rejected in the analysis is determined to be $p_{\mathrm{C}} = 60.8(7.0)\%$. The most frequent cause for this is that the event fails the fiducial volume conditions for a muon stop. Figure 6.3 displays an example of a connected CPE event that is rejected for this reason.

At later times ($t_n - t_\mu >$1000 ns) the charge deposition from the emitted charged particle track is increasingly spatially and temporally separated from that of the muon stop, and disconnected CPE events are observed. The selection of disconnected events is stable after 2000 ns. Of these events $p_{\mathrm{D}} = 15.1(3.7)\%$ fail the analysis cuts and are rejected. Given the

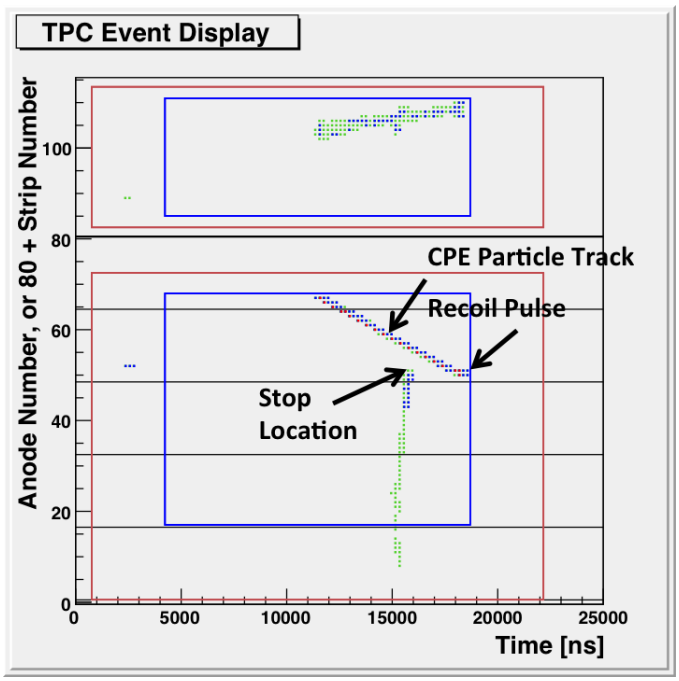

Figure 6.4: An example of a disconnected CPE event. The charge deposition of the muon stop and the emitted CPE particle are well separated. The event is an example of the emitted particle depositing sufficient energy to excite the EH and even EVH energy thresholds in the wire chamber readout. The CPE track is independently identified as a particle track in the analysis. The time spectrum of events like this is used for the CPE interference correction. Note: The pulse induced by the recoiling nucleus is present in CPE events, but it is not separated from the charge induced by the emitted particle. The arrow indicating the recoil pulse also indicates the location of the capture event, and the point of origin of the emitted particle.

disconnected topology, the rejection of these events is due to the standard cuts applied to select good muon stop events, as described in Section 3.1.2, and not due to charge interference from CPE. In $p_{\mathrm{T}} = 35.7(6.2)\%$ of the disconnected events the CPE particle charge deposition is identified by the analysis as a particle track in the TPC. Figure 6.4 shows an example of a disconnected CPE event as it appears in the TPC event display. The event shown here is an example where the emitted charged particle is identified in the analysis as an independent track in the TPC.

The CPE process results in a distortion in the neutron time spectrum due to the biased rejection of events at early times. CPE is consistent with the capture process and the time spectrum of all such events is the same as for the rest of the data, but under-represented at

early times. In order to consistently represent all CPE capture events a correction is made by subtracting the time spectrum of the disconnected CPE events with a secondary track identified in the TPC. The fraction of that time spectrum to subtract, f_{CPE}, is

$$f_{\mathrm{CPE}} = \frac{p_{\mathrm{C}} - p_{\mathrm{D}}}{p_{\mathrm{T}}} = 1.28(31).$$

The systematic errors introduced by this procedure are determined by the change in the time spectrum fit results when 0.31 times less or more of the correction time distribution is subtracted. The resulting systematic errors are 3.1 $\times 10^2$ s^{-1} and 1.42 $\times 10^4$ s^{-1} for $r_{\mu p}$ and $r_{\mu\mathrm{Ar}}$, respectively. With this correction, and the background correction discussed in the previous section, the definition of the analysis time spectrum is complete.

Nuclear recoil pulses, found in the majority of capture events and shown in Figure 3.4, can induce a distortion in the neutron time spectrum due to interference. The recoil pulse is not more than < 7.0 mm in spatial extent in any dimension, and it is unable to affect the determination of the muon stop location in the TPC beyond that distance scale. These events are less susceptible to failing the fiducial volume conditions due to interference than the connected CPE events. The probability of the early-time recoil events with interference being rejected in the analysis is found to be 17.6(1.9)%. The later-time capture recoil events (without interference) are rejected with a probability of 19.5(7)%. The conclusion is that the selection of recoil-only events is stable, and it is CPE interference alone that must be corrected for.

6.3 Model of the Capture Neutron Time Spectrum Kinetics

In this experiment $\approx 7.0\%$ of events result in the muon capturing onto an argon nucleus, which dominates the neutron time spectrum. Capture neutrons from the μp and ortho-

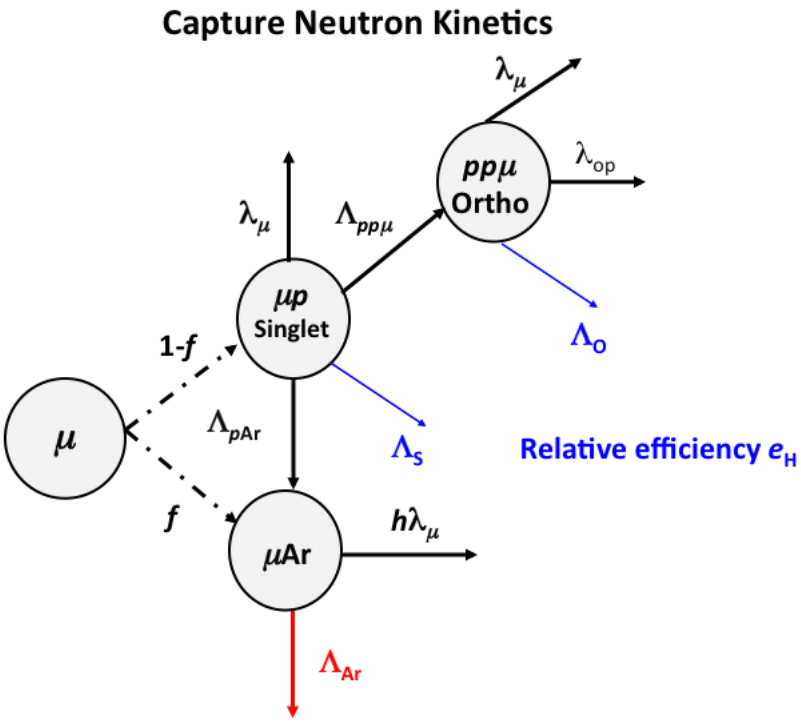

Figure 6.5: Diagram of the kinetics taken into account in the capture neutron time spectrum fit function. As explained in the text, prompt μAr formation, and the kinetics associated with the μp and ortho-molecular states are taken into account. The relative efficiency ($e_{\rm H}$) of the 5.2 MeV hydrogen capture neutrons is taken into account as well.

molecular states and prompt μAr formation are also accounted for in the fit to the data. Figure 6.5 diagrams the kinetic processes and systematic effects included in the fit function. In the decay electron time spectrum analysis, most of the systematic corrections are implemented in the fit function, and the same approach is taken here.

The description of the observed capture neutron time spectrum, $n_n^{\rm Obs.,Ar}(t)$, is detailed in the following equations:

$$\begin{aligned}
n'_{\mu p}(t) &= -r_{\mu p} n_{\mu p}(t), \\
n'_{\mu \rm Ar}(t) &= \Lambda_{p\rm Ar} n_{\mu p}(t) - r_{\mu \rm Ar} n_{\mu \rm Ar}(t), \\
n'_{\rm Ortho}(t) &= \Lambda_{pp\mu} n_{\mu p}(t) - (\lambda_\mu + \lambda_{\rm op} + \Lambda_{\rm O}) n_{\rm Ortho}(t), \\
\text{and } n_n^{\rm Obs.,Ar}(t) &= e_{\rm H}(\Lambda_{\rm S} n_{\mu p}(t) + \Lambda_{\rm O} n_{\rm Ortho}(t)) + (r_{\mu \rm Ar} - h\lambda_\mu) n_{\mu \rm Ar}(t). \qquad (6.1)
\end{aligned}$$

The initial conditions for this system of equations are

$$\begin{aligned} n_{\mu p}(t=0) &= 1-f, \\ n_{\mu\mathrm{Ar}}(t=0) &= f, \\ \text{and } n_{\mathrm{Ortho}}(t=0) &= 0. \end{aligned}$$

The above equations represent the same physics as in Equations 4.7 - 4.10, but with the disappearance rates $r_{\mu p}$ and $r_{\mu\mathrm{Ar}}$ substituted in the expressions for $n'_{\mu p}(t)$ and $n'_{\mu\mathrm{Ar}}(t)$. The notable difference in the observed and physical time distributions, $n_n^{\mathrm{Obs.,Ar}}$ and $n_n^{\mathrm{Phy.,Ar}}$ (Eq. 4.12) respectively, is due to the relative efficiency e_{H} of the capture neutrons produced from the hydrogen states. The contribution of para-molecular state capture neutrons is neglected in this analysis. The fraction of events produced from that state is less than 10^{-4}, which can be compared to the relative statistical precision that is greater than 10^{-3}.

An amplitude A and a background B constant are applied to $n_n^{\mathrm{Obs.,Ar}}(t)$ in the fit function, where

$$A \cdot n_n^{\mathrm{Obs.,Ar}}(t) + B.$$

The fit to the capture neutron time spectrum has four independent variables: $r_{\mu p}$, $r_{\mu\mathrm{Ar}}$, A and B. The $\Lambda_{p\mathrm{Ar}}$ and $\Lambda_{pp\mu}$ rates appear in the fit function to constrain the relative contributions of the μAr and ortho-molecular state capture neutrons. The $\Lambda_{p\mathrm{Ar}}$ and $\Lambda_{pp\mu}$ results of the decay electron time spectrum analysis are used for this purpose, without compromising the determination of the $r_{\mu p}$ and $r_{\mu\mathrm{Ar}}$ rates. The associated systematic error from this procedure is reported in Section 6.7. The μAr state contribution to the time spectrum scales as $\Lambda_{\mathrm{Ar}} n_{\mu\mathrm{Ar}}(t)$ in Eq. 4.12, yet $r_{\mu\mathrm{Ar}} - h\lambda_\mu$ replaces Λ_{Ar} in order to not use that rate as a parameter in the fit function. The rates Λ_{S}, Λ_{O}, λ_{op} and λ_μ determine the time distribution of the μp and ortho-molecular state capture neutrons, and are fixed to the values reported previously in Section 4.2. The μAr state decay rate parameter, h, is fixed

to the value determined in Section 4.1.2.

6.4 Hydrogen Capture Neutron Efficiency Calibration

The relative efficiency, e_{H}, of detecting capture neutrons from the hydrogen states is determined with a comparison of the yield of neutron events in the pure hydrogen and the argon-doped gas data. The expected ratio of the number of capture neutron and decay electron events in the pure hydrogen gas is

$$f_{\mathrm{H}} = \frac{\int_{0\ \mathrm{ns}}^{20000\ \mathrm{ns}} n_n^{\mathrm{H}}(t)dt}{\int_{0\ \mathrm{ns}}^{20000} n_e^{\mathrm{H}}(t)dt} \approx \frac{\Lambda_{\mathrm{S}}}{\lambda_\mu + \Lambda_{\mathrm{S}}} = 0.00154(4),$$

where $n_n^{\mathrm{H}}(t)$ and $n_e^{\mathrm{H}}(t)$ are the physical time distributions of capture and decay events in that gas. The observed ratio of capture neutron and decay electron events in the pure hydrogen data is $r_{\mathrm{H}} = 6.42(12) \times 10^{-5}$. The quantity $r_{\mathrm{H}}/f_{\mathrm{H}}$ scales with the detection efficiency of the 5.2 MeV neutrons, ϵ_{H} such that

$$\frac{r_{\mathrm{H}}}{f_{\mathrm{H}}} \propto \frac{\epsilon_{\mathrm{H}}}{\epsilon_e},$$

where ϵ_e represents the probability of detection for the decay electron events.

The expected ratio of capture and decay events in the argon-doped gas, f_{Ar}, is likewise determined from the physical time spectra of these events

$$f_{\mathrm{Ar}} = \frac{\int_{0\ \mathrm{ns}}^{20000\ \mathrm{ns}} n_n^{\mathrm{Phy.,Ar}}(t)dt}{\int_{0\ \mathrm{ns}}^{20000\ \mathrm{ns}} n_e^{\mathrm{Phy.,Ar}}(t)dt} = 0.0707(21)\ \left(\approx \frac{\int_{0\ \mathrm{ns}}^{20000\ \mathrm{ns}} n_{\mu\mathrm{Ar}}(t)dt}{\int_{0\ \mathrm{ns}}^{20000\ \mathrm{ns}} n_e^{\mathrm{Phy.,Ar}}(t)dt} + \mathcal{O}(2\ \%)\right),$$

as defined in Equations 4.11 and 4.12. The fraction f_{Ar} is determined by the electron time spectrum analysis results for $\Lambda_{pp\mu}$, $\Lambda_{p\mathrm{Ar}}$ and Λ_{Ar}, and the known values of the hydrogen kinetic rates. The relative contribution to f_{Ar} from capture in the hydrogen states is $\approx 2.1\%$. A 3% relative error is applied to account for this, which is reflected in the value reported above and is larger than the combined error in f_{Ar} from the experimental values of $\Lambda_{pp\mu}$,

$\Lambda_{p\mathrm{Ar}}$ and Λ_{Ar}. The approximation that the yield of neutron events in argon-doped gas data represents the yield of μAr state capture neutrons works to the level of precision necessary to determine e_{H} for this analysis. The observed ratio of the number of capture neutron and decay electron events in the argon-doped gas data is $r_{\mathrm{Ar}} = 0.001607(12)$. The efficiency of the predominantly 1.0 - 3.0 MeV μAr capture neutrons, ϵ_{Ar}, scales as

$$\frac{r_{\mathrm{Ar}}}{f_{\mathrm{Ar}}} \propto \frac{\epsilon_{\mathrm{Ar}}}{\epsilon_e},$$

in analogy to above for the hydrogen neutrons.

The relative efficiency of the hydrogen and argon capture neutrons is determined by

$$e_{\mathrm{H}} = (r_{\mathrm{H}}/f_{\mathrm{H}})/(r_{\mathrm{Ar}}/f_{\mathrm{Ar}}) = \epsilon_{\mathrm{H}}/\epsilon_{\mathrm{Ar}} = 1.833(80),$$

where the efficiency of detection for the decay electrons cancels[3]. The 5.2 MeV hydrogen capture neutrons contribute $\approx 4.0\%$ of the observed events in the data, instead of $\approx 2.1\%$ as expected from the kinematics.

The detector efficiency is one source of the difference in the yield of capture neutrons produced in the hydrogen states relative to those originating from the μAr state. Another source is that capture onto elements like argon results in no neutron being emitted with finite probability. The fraction of events in which this is the case has been measured for capture onto aluminum and calcium, and was found to be ≈ 10 and 30% for those elements, respectively [69]. A similar fraction of neutron-less events is anticipated for capture onto argon.. The calibrated efficiency e_{H} represents the relative probability that capture onto argon or capture from a hydrogen state will produce an identified event in the neutron time spectrum.

[3]Although the relative efficiency of μAr state decay electrons, e_{Ar} was discussed in the context of the electron time spectrum analysis, this effect is at the level of 10^{-3} in the number of all decay events, and consequently r_{Ar}. This source of error is neglected relative to the percent-level errors applied in this calculation.

6.5 Timing Calibration

The time-of-flight of the neutrons from the location of a capture event to the detectors outside the TPC vessel is an additional feature of the time spectrum. A 5.2 MeV neutron requires ≈ 18 ns to travel the 566 mm from the center of the TPC to the center of one of the liquid scintillator detectors. The time-of-flight of the neutrons determines the average time at which these events appear in the time spectrum, t_{H}. The events which occur on either the far or near side of the TPC relative to a give scintillator detector arrive in a distribution before and after the average time of arrival. That distribution is assumed to have a width s_{H} which will be referred to as the spread in the time-of-flight. The effective spread in the timing of events in the data is also associated with variation in the time definition implemented in the waveform analysis of the neutron events. The average time of arrival of the hydrogen capture neutrons (t_{H}) is calibrated to ±(2) ns precision, and the spread in the time-of-flight is determined to be $s_{\mathrm{H}} = 15.5(5.9)$ ns directly from fits to the pure hydrogen data[4].

The timing calibration for the argon capture neutrons is not as directly available from the data. The spectrum of these events has no transition feature at early times, because it is dominated by the

$$\approx e^{-r_{\mu p}t} - e^{-r_{\mu \mathrm{Ar}}t}$$

time-dependence of the μAr state population. A bound for the spread of the time-of-flight of these capture neutrons, s_{Ar}, is placed at $s_{\mathrm{Ar}} = 15.5(10.9)$ ns from fits to the data. Efforts to extract the timing calibration t_{Ar} are, however, not reliable.

A 2.0 MeV neutron takes ≈11.0 ns longer than a 5.2 MeV neutron to travel the 566 mm from the center of the TPC to the center of a liquid scintillator detector. The average time of arrival of these events in the time spectrum is estimated to be $t_{\mathrm{Ar}} = t_{\mathrm{H}} + 11.0$ ns. A 1.0 or 3.0 MeV neutron arrives in a time window ≈8.0 ns before and after a 2.0 MeV

[4]The pure hydrogen time spectrum has a clear transition feature at early times and can be fitted directly to extract such information.

neutron, which determines an average time of arrival of $t_{\mathrm{Ar}} = t_{\mathrm{H}} + 11.0 \pm 8$ ns. As described this may appear to be an effect that belongs to the spread in the time of flight, s_{Ar}, of these capture neutrons. The obstacle is that the average energy (and subsequently the average time-of-flight) of these events is not well understood.

Knowledge of the average energy of argon capture neutrons can facilitate a determination of the average time-of-flight, and reduce the 8 ns uncertainty for t_{Ar}. The response of the liquid scintillator detectors is not linear with neutron energy [44]. The physical energy distribution of the capture neutrons is not directly interpretable from the pulse integral spectrum of the detector events. Any such interpretation requires a unfolding procedure of that spectrum that is precise. The energy spectrum of the argon capture neutrons is not sufficiently determined (experimentally or theoretically) to constrain this calibration to better than 8.0 ns, and the $t_{\mathrm{Ar}} = t_{\mathrm{H}} + 11.0 \pm 8$ ns result above is used.

The timing calibration is implemented for each e^{-rt} term of the fit function. The spread in the time-of-flight is applied analytically as a gaussian convolution over t, where

$$e^{-rt} \rightarrow \int_{t_{\mathrm{H}}}^{\infty} e^{-r(v-t_{\mathrm{H}})} \times \frac{1}{\sqrt{2\pi} s_{\mathrm{H}}} e^{-(v-t)^2/2s_{\mathrm{H}}^2} dv = e^{-r(t-t_{\mathrm{H}})+(s_{\mathrm{H}}^2 r^2/2)} \times \frac{1}{2}\left(1 + \mathrm{erf}\left(\frac{r s_{\mathrm{H}}^2 - t + t_{\mathrm{H}}}{\sqrt{2} s_{\mathrm{H}}}\right)\right). \tag{6.2}$$

The parameters t_{H} and s_{H} are specific to the 5.2 MeV hydrogen capture neutrons, and implemented for those terms representing μp and ortho-molecular state capture in the fit function. The timing calibration of the dominant argon capture neutrons is likewise implemented for the $n_{\mu\mathrm{Ar}}(t)$ terms in the fit function.

6.6 Fit Consistency and Systematic Corrections

The fit to the capture neutron time spectrum is depicted in Figure 6.6. The upper panel shows the corrected time spectrum (black), with the fit function result (red). The lower panel illustrates the agreement of the data and fit function in the 600 - 20000 ns time

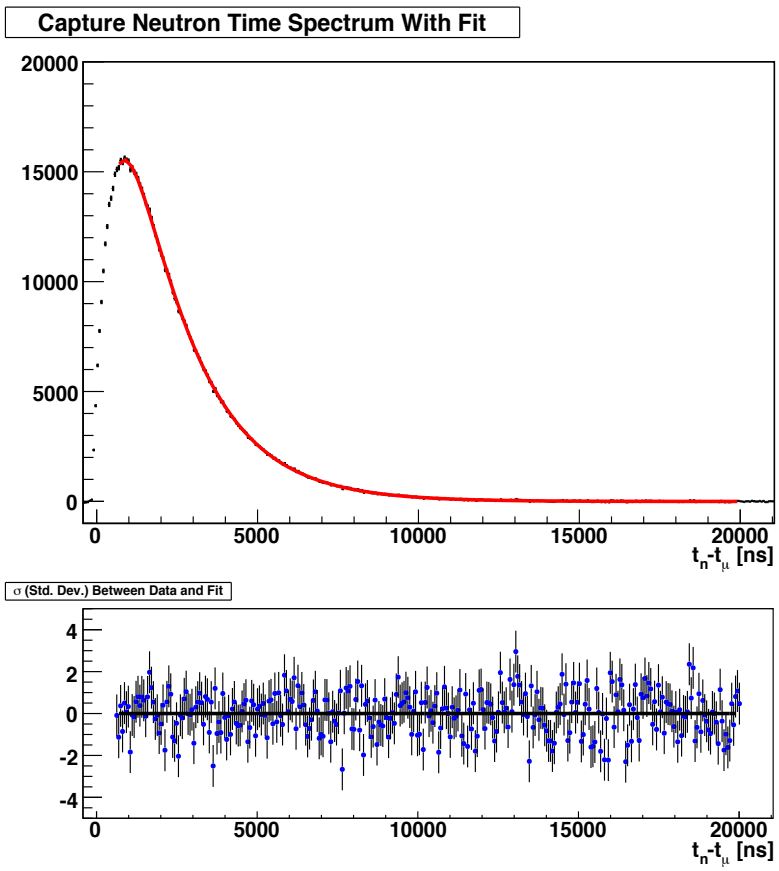

Figure 6.6: Upper panel: The neutron time spectrum (black) shown with the fitted function (See Eq. 6.1) for a 600 - 20000 ns time range (red). Lower Panel: The agreement of this fit is further shown by the pull plot in the same fit window.

window of the fit, in units of σ of the data histogram. The normalized $\chi^2/Ndf = 0.978(79)$ reflects the agreement between the data and the fit as well. The extracted results are $r_{\mu p} = 0.5214(16)\ \times 10^6\ \mathrm{s}^{-1}$ and $r_{\mu \mathrm{Ar}} = 1.737(15)\ \times 10^6\ \mathrm{s}^{-1}$.

Figure 6.7 shows the 0 and 2000 ns start-time scan of the fit. The results for $r_{\mu p}$ and $r_{\mu \mathrm{Ar}}$ appear in the top and middle panels (black). The bottom panel shows the probability of agreement for the fit results (black). The fit probability is used because it quantifies the goodness-of-fit on a finite 0.0 - 1.0 scale for direct comparison, whereas the χ^2 is not bounded. The variation of the central values of the results (blue) is shown compared to the allowed statistical limits (red), as discussed in Section 5.1. Finally, the change in the results when the argon capture neutron timing calibration, t_{Ar}, is varied by ± 4 ns (orange) and

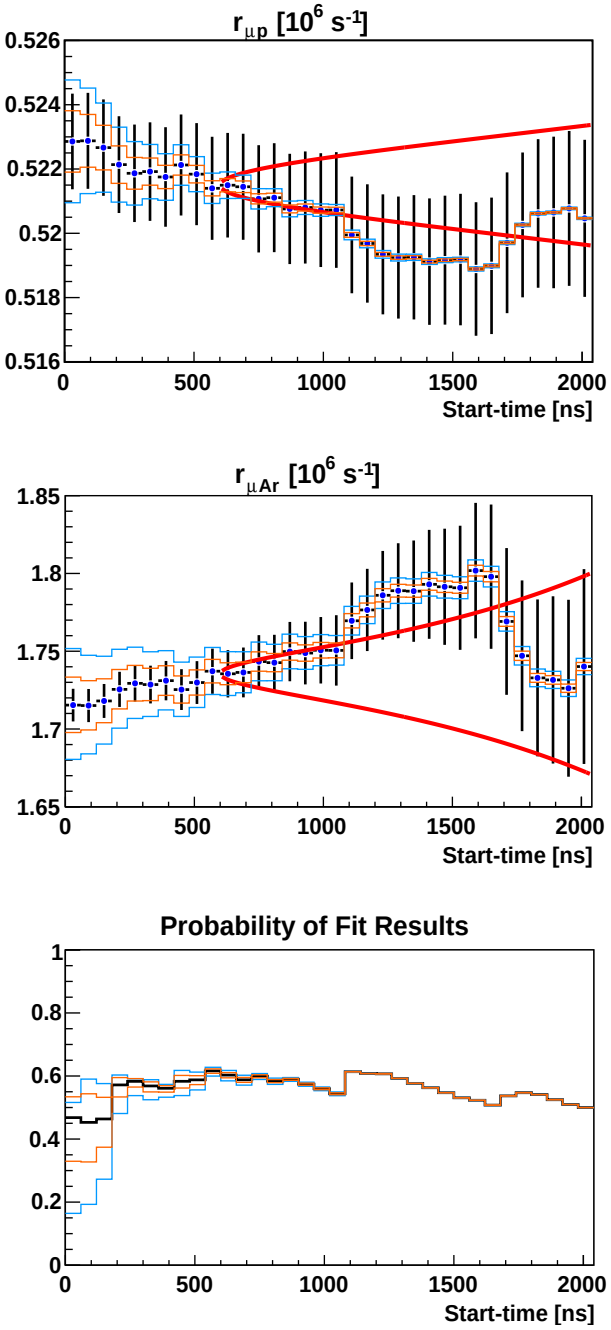

Figure 6.7: The start-time scan (black) for the capture neutron time spectrum fit. The start-time is varied between 0 and 2000 ns, where the fit stop-time is constant at 20000 ns. The variation of the fit results (blue) is shown compared to the allowed set-subset limit of variation (red), and is favorable from 600 ns. The variation in the fit results when the argon capture neutron timing calibration, t_{Ar}, is varied by ± 4 ns (orange) and ± 8 ns (light blue) is presented as well.

± 8 ns (light blue) is shown, which depicts the magnitude of the systematic error for that effect. A start-time of 600 ns is chosen both because the fit results are consistent from this time, and to minimize the systematic error from the timing calibration.

The systematic variation of the fit results shown in Figure 6.7 is a consequence of the fact that the $r_{\mu\mathrm{Ar}}$ disappearance rate dominates the capture time spectrum in the first 2000 ns. The $r_{\mu\mathrm{Ar}}$ fit result relies on the statistics in this time window to determine this rate, which induces the sensitivity to the timing calibration shown in the middle panel of Figure 6.7. The disappearance rates are correlated in the fit function, which manifests as the variation observed for $r_{\mu p}$ in the top panel of Figure 6.7. The consequence of this characteristic of the fit is that while the statistical error decreases the earlier the start-time is set, the systematic error can increase. The sensitivity of the results to the t_{Ar} timing calibration is one example of this.

Figure 6.8 depicts start-time scan results for $r_{\mu p}$, $r_{\mu\mathrm{Ar}}$ and the fit probability as in Figure 6.7, depicts the significance of the remaining systematic corrections applied in the fit function. The corrections are included one by one in the fit function in the following order:

- No systematic correction (red);
- Prompt μAr formation (pink);
- Capture from the μp state (green);
- Relative efficiency of the μp state events (blue);
- Capture from the ortho-molecular state (black), including the relative efficiency of such events (black).

The fit results with none of these corrections applied (red) show a magnitude of variation that is greater than the statistical errors for both of the extracted rates (top and middle panels). The probability of the fit under this condition (bottom panel) is also start-time-dependent. The statistically significant magnitude of variation in the fit results is incrementally reduced

as each effect is taken into account. The magnitude of the correction for ortho-molecular state capture is shown by the difference between these results (blue) and the corrected results (black), which is ≈1/3 of the statistical error for the $r_{\mu p}$ rate. The pattern of the fit results shows that the 600 ns start-time, motivated in Figure 6.7, limits sensitivity to the systematic effects depicted here.

6.7 Results and Summary

The systematic corrections and errors applied to the disappearance rate results are reported in Table 6.1. The reported values for each correction included in the fit function are shown in italics to emphasize that they are not applied externally to the results in the first row of the table. The reported values for each of these corrections is the change in the extracted results each effect is individually included or excluded in the fit function. The associated systematic errors are likewise determined by the change in the fit results when each systematic parameter is varied by its known uncertainty. The only correction applied externally to the fit results is that for the effect of oxygen in the target gas.

The effect of oxygen in the target gas was discussed in Section 4.3 in the context of the electron time spectrum. The effective transfer and capture rates to oxygen are $\Lambda_{\mathrm{pO}} = 121\ \mathrm{s}^{-1}$ and $\Lambda_{\mathrm{O}} = 0.102\ \times 10^{6}\ \mathrm{s}^{-1}$, respectively for the conditions of this experiment. The relative fraction of oxygen capture events is $\approx 6 \times 10^{-4}$, which indicates corrections to $r_{\mu p}$ and $r_{\mu \mathrm{Ar}}$ that are smaller in magnitude than the statistical errors of these rates. In analogy to the work discussed previously, a simulation is used to determine the magnitude of the corrections and errors due to this effect[5]. Those results are reported in Table 6.1. The magnitude of the systematic correction and error for this effect is determined to be 1/10 or less of the statistical errors of both $r_{\mu p}$ and $r_{\mu \mathrm{Ar}}$.

[5]A series of pseudo-data histograms representing hypothetical capture neutron time spectra is generated, with the concentration of oxygen varied between 0.00 and 0.25 ppm. The assumed values for $\Lambda_{pp\mu}$, $\Lambda_{p\mathrm{Ar}}$ and Λ_{Ar} in the simulations are those determined from the electron time spectrum analysis, and the remaining kinetic rates for the hydrogen chemistry processes are the known values as discussed in Section 4.2. The

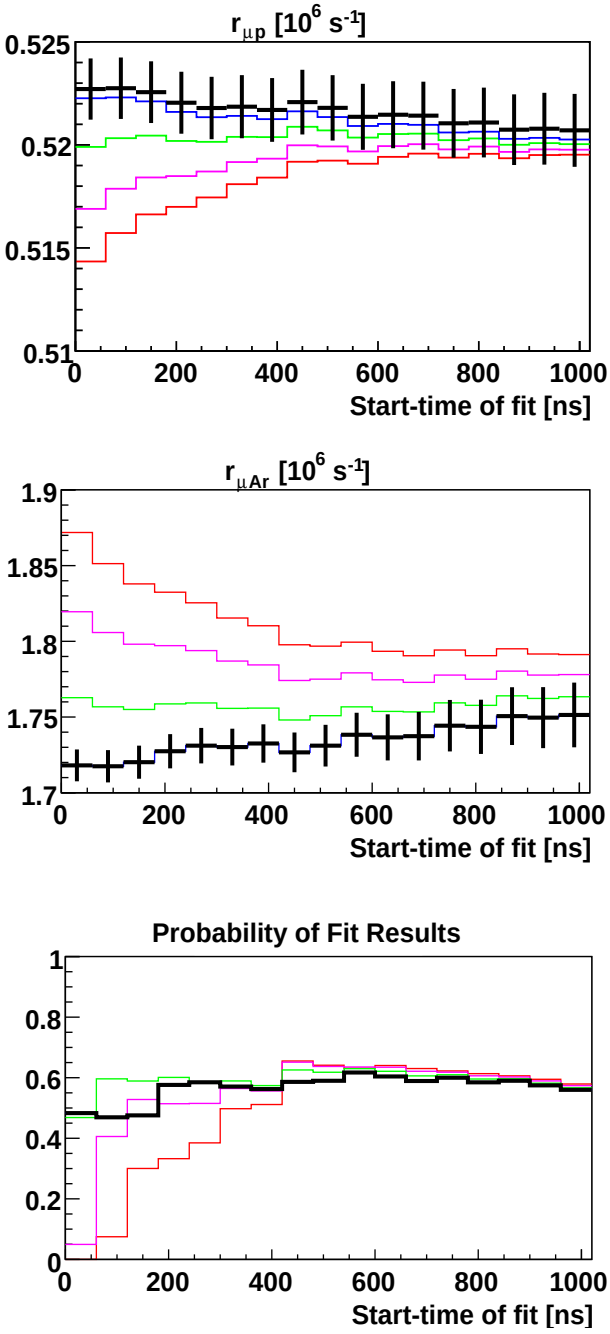

Figure 6.8: The fit results taking all systematic effects into account (black) are shown here for start-times between 0 and 1000 ns, as in Figure 6.7. The curves in color represent the change in fit results when: no systematic corrections are made (red); when prompt μAr formation is accounted for (pink); when μp state capture is additionally considered (green); when the effect of the relative efficiency of the μp state capture neutrons is included (blue), and lastly when capture from the ortho-molecular state (including the relative efficiency of these events) is included (black). Note: The magnitude of ortho-molecular state capture correction is sufficiently small for $r_{\mu\mathrm{Ar}}$ that the curve representing results including this effect (black), covers those that exclude it (blue), and are not distinguishable in the middle panel.

Table 6.1: Table of systematic corrections and errors for the $r_{\mu p}$ and $r_{\mu \mathrm{Ar}}$ results of the capture neutron time spectrum analysis. The analysis fit results are reported in the first row of the table, and are emphasized with double lines. The total systematic errors and the final results (emphasized with double lines) in the bottom rows of the table. Note: The combined error from fixing the $\Lambda_{pp\mu}$, $\Lambda_{p\mathrm{Ar}}$ rates and h in the fit function is determined to be 1.5 $\times 10$ s^{-1}, and 2.0 $\times 10^2$ s^{-1} for $r_{\mu p}$ and $r_{\mu \mathrm{Ar}}$, respectively. The magnitude of these errors are negligible compared to the statistical errors of both disappearance rates, and are not included below.

Table of Systematic Corrections and Errors				
Rate	$r_{\mu p}$ [$\times 10$ s^{-1}]		$r_{\mu \mathrm{Ar}}$ [$\times 10^2$ s^{-1}]	
Fit result	52147	163	17365	152
	Correction	Error	Correction	Error
Timing Calibration: t_{Ar}		41		142
Prompt μAr formation: f	*52*	10	*-188*	35
Proton capture : Λ_{S} (Λ_{O})	*83*	4	*-209*	10
Relative efficiency: e_{H}	*69*	7	*-171*	16
Ortho-para transition: λ_{op}	*18*	8	*6*	3
CPE interference correction		31		127
Oxygen impurity correction	16	15	3	3
Total	16	56	3	192
Final result	52163	173	17368	244

The corrections due to prompt μAr formation and capture from the hydrogen states (Λ_{S} and e_{H}) are the most significant in this analysis. The magnitude of these corrections is greater than the statistical error of $r_{\mu \mathrm{Ar}}$, and between 1/2 and 1/3 of the statistical error for $r_{\mu p}$. The effect of the ortho-para molecular state transition is smaller in magnitude than the statistical error of both extracted rates.

The systematic errors applied to the $r_{\mu p}$ and $r_{\mu \mathrm{Ar}}$ results are dominated by the timing calibration of the μAr state capture neutrons[6] (t_{Ar}), and CPE interference. The rate $r_{\mu \mathrm{Ar}}$, in

input values for the oxygen transfer and capture rates are as reported in Section 4.3. The linear variation of the $r_{\mu p}$ and $r_{\mu \mathrm{Ar}}$ fit results to the pseudo-data histograms is likewise quantified with a linear fit, and used to determine the associated systematic correction and errors. The same concentration of oxygen ($c_{\mathrm{O}} = 0.12(11)$ ppm) is assumed as explained in Section 4.3. One assumption made is that the efficiency of detecting neutrons produced from capture onto oxygen is the same as for those involving argon. The relative efficiency of the oxygen capture events is not explicitly determined, but the large relative uncertainty applied for the concentration of oxygen and the magnitude of this correction make this a practical assumption.

[6]The combined systematic errors due to t_{H}, s_{H} and s_{Ar} are found to be 2.6×10 s^{-1} and 9.1×10^2 s^{-1} for $r_{\mu p}$ and $r_{\mu \mathrm{Ar}}$, respectively. These errors contribute negligibly to the reported error for t_{Ar}.

particular, acquires a total systematic error that is greater in magnitude than the statistical error. Capture from the μp and ortho-molecular states is a significant correction to the results of this analysis, but is determined to induce systematic errors[7] (via Λ_S, e_H and λ_{op}) which are of the order of 1/10 of the statistical error for both $r_{\mu p}$ and $r_{\mu Ar}$. The error introduced by neglecting capture from the para-molecular state is smaller in magnitude than the reported errors for the ortho-para transition rate.

The final results of the capture neutron time spectrum analysis are

$$r_{\mu p} = 0.5216(17) \times 10^6 \text{ s}^{-1}$$

and

$$r_{\mu Ar} = 1.737(24) \times 10^6 \text{ s}^{-1}.$$

The neutron time spectrum analysis is an internal consistency check to the results of the electron time spectrum, which include determinations of $r_{\mu p}$ and $r_{\mu Ar}$. The results for $r_{\mu Ar}$ ($1.750(16) \times 10^6$ s^{-1} as determined by the electron time spectrum analysis) are consistent to 0.5 σ The μp state disappearance rate, $r_{\mu p}$, is sensitive to $\Lambda_{pp\mu}$ (per Eq. 4.13), and the consistency of the decay electron and capture neutron time spectrum analyses for this rate is notably a consistency check for the molecular formation rate result. The electron time spectrum analysis determined $r_{\mu p}$ to be $0.5235(8) \times 10^6$ s^{-1}. The $r_{\mu p}$ disappearance rates results agree to 1.0 σ.

Figure 6.9 depicts the consistency of the results of the decay electron (blue) and capture neutron (red) time spectra analyses. The displayed ellipses correspond to the 1.0 and 2.0 σ contours of the final results in the $r_{\mu p} : r_{\mu Ar}$ parameter space. In two dimensions a 2.0 σ contour corresponds to a ≈ 91 % confidence level.

The $r_{\mu Ar}$ result is potentially a contribution to the world knowledge of the μAr capture rate, which is determined to be

[7]The error reported for the effect of proton capture is the change in the fit results when Λ_S is varied by the experimental uncertainty for this rate, 17.4 s^{-1}. The ortho-molecular state capture rate Λ_O is varied simultaneously because it is parameterized in terms of Λ_S in the fit function.

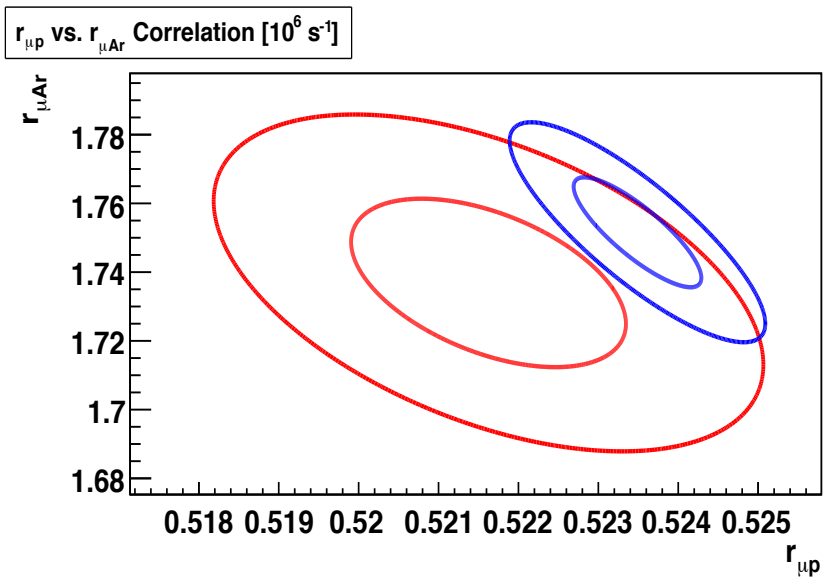

Figure 6.9: The consistency of the $r_{\mu p}$ and $r_{\mu \mathrm{Ar}}$ results of the decay electron (blue) and capture neutron (red) time spectra analyses is illustrated in this two dimensional plot. For each analysis result an ellipse is shown for the 1.0 and 2.0 σ contour of the errors in the $r_{\mu p} : r_{\mu \mathrm{Ar}}$ parameter space. The correlation of $r_{\mu p}$ and $r_{\mu \mathrm{Ar}}$ rates in each result is represented in this way, too. The vertical and horizontal extent of each ellipse depicts the 1.0 and 2.0 sigma ranges of the reported results, which appear in the text.

$$\Lambda_{\mathrm{Ar}} = 1.288(25)\ \times 10^6\ \mathrm{s}^{-1}.$$

That determination is consistent to 0.5 σ with the 1.302(16) $\times 10^6$ s^{-1} result from the electron time spectrum analysis. The weighted average of these results is 1.298(13) $\times 10^6$ s^{-1}, and comparable to the most precise experimental report of 1.31(1) $\times 10^6$ s^{-1} [29].

Although a combined average of the two sets of results of this work can further minimize the errors of these results, the ambiguities of the neutron timing calibration (notably for the μAr state capture neutrons) are considerable systematic limitation. Additionally, the neutron time spectrum is subject to a background subtraction, and an interference correction, both of which represent statistically significant systematic effects. Although CPE interference has been quantified and corrected for in a data-motivated method, it cannot be fully excluded that there are not additional interference effects associated with the capture recoil events. Following from these uncertainties the decision is made to emphasize the results extracted from the well-understood electron time spectrum as the final results of this work.

Chapter 7

Conclusions and Summary

The experiment presented in this work is a dedicated measurement of the formation rate of $pp\mu$ molecules in hydrogen. The method is to obtain time spectra of both decay electrons and capture neutrons from muons stopping in a TPC detector containing pure protium hydrogen gas doped with 19.6(1.1) ppm (atomic) of argon. The design of the detector setup ensures the selection of events that stop in the target gas and not in heavier materials.

An analysis of the decay electron time spectrum provides independent determinations of the molecular formation and transfer rates, $\Lambda_{pp\mu}$ and $\Lambda_{p\mathrm{Ar}}$, as well as the muon capture rate onto argon, Λ_{Ar}. These data are obtained under identical conditions as the primary MuCap data set with a pure protium target, which is used for the measurement of the muon disappearance rate λ_-. The improved knowledge of the molecular formation rate is required to reduce the uncertainty of the extraction of Λ_{S} from λ_- due to a correction for molecular state effects, $\Delta_{pp\mu}$.

The main results of this work are derived from the electron time spectrum. Those are:

1. The effective rate of $pp\mu$ molecular formation from the μp state,

$$\Lambda_{pp\mu} = [2.227 \pm (0.062)_{\mathrm{stat}} \pm (0.020)_{\mathrm{sys}}] \ \times 10^4 \ \mathrm{s}^{-1}; \tag{7.1}$$

2. The effective muon transfer rate to argon from the proton,

$$\Lambda_{p\mathrm{Ar}} = [4.526 \pm (0.015)_{\mathrm{stat}} \pm (0.004)_{\mathrm{sys}}] \ \times 10^4 \ \mathrm{s}^{-1}; \tag{7.2}$$

3. The absolute μAr capture rate,

$$\Lambda_{\mathrm{Ar}} = [1.302 \pm (0.014)_{\mathrm{stat}} \pm (0.007)_{\mathrm{sys}}] \ \times 10^6 \ \mathrm{s}^{-1}. \tag{7.3}$$

The normalized formation and transfer rates, $\lambda_{pp\mu}$ and $\lambda_{p\mathrm{Ar}}$, can be compared to previous experiments. The gas density, $\phi = 0.0115(1)$, and atomic concentration of argon, $\mathrm{c_{Ar}} = 19.6(1.1)$ ppm, determine these normalized rates to be

$$\lambda_{pp\mu} = [1.937 \pm (0.054)_{\mathrm{stat}} \pm (0.024)_{\mathrm{sys}}] \times 10^6 \ \mathrm{s}^{-1} \tag{7.4}$$

and

$$\lambda_{p\mathrm{Ar}} = [2.008 \pm (0.067)_{\mathrm{stat}} \pm (0.115)_{\mathrm{sys}}] \times 10^{11} \ \mathrm{s}^{-1}. \tag{7.5}$$

7.1 The Molecular Formation Rate

The normalized molecular formation rate has $\approx 3\%$ relative precision, which is threefold more precise than previous results. To reduce the molecular formation rate systematic error for the final MuCap singlet capture rate, Λ_{S}, measurement to 2 s^{-1} or less, a measurement of $\lambda_{pp\mu}$ to $\approx 10\%$ relative precision is required. The present result exceeds this goal.

The updated world knowledge of the molecular formation rate is summarized in Figure 7.1. The previously reported results are presented in Section 1.2.2 and Figure 1.7. The present $\lambda_{pp\mu}$ result agrees well with the existing theoretical prediction [11], but differs from the previous result of Bystritskii et al. [21] at the level of 2.3 σ, which is the only experiment performed with a comparable gaseous target. The result obtained using a solid hydrogen target is 7.1 σ different from the present result, indicating systematic effects associated with the solid state.

An updated world average of the liquid and gaseous hydrogen target results, $\langle \lambda_{pp\mu} \rangle$, is

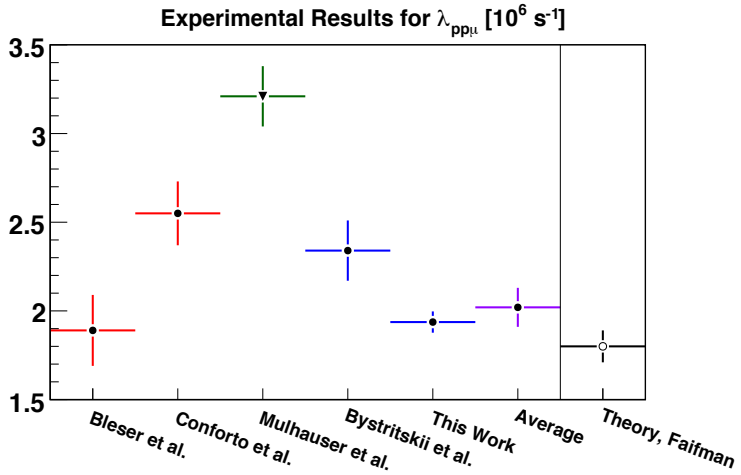

Figure 7.1: The plot shows updated experimental knowledge of the molecular formation rate, $\lambda_{pp\mu}$. The present result obtained from this experiment is now included (blue), as well as the updated average, as stated in the text.

determined to be[1]

$$\langle \lambda_{pp\mu} \rangle = 2.02(11) \times 10^6 \text{ s}^{-1}.$$

The error on this average is adjusted to account for the variation in the results and methods represented by the four experimental results included in this average.

7.1.1 The Molecular State Correction For The Λ_S Determination

The improved knowledge of the molecular formation rate reduces the uncertainty in the MuCap determination of Λ_S. The relative precision of $\lambda_{pp\mu}$ affects the systematic uncertainty of the molecular state correction, $\Delta_{pp\mu}$. The present measurement of $\lambda_{pp\mu}$ was extracted from data obtained under identical conditions as the pure protium gas data. Using this result guarantees that the molecular state correction, $\Delta_{pp\mu}$, used for the Λ_S determination is appropriate.

The linear approximation for $\Delta_{pp\mu}$ presented in Eq. 1.24 is not sufficient for this procedure, and more advanced simulation techniques are used. The approximate relation allows

[1]This follows from the weighted average of the four experimental results in question and inflating the error of that average by the square root of the reduced χ^2/Ndf of the independent results relative to that average. This follows from the Particle Data Group averaging procedure [1].

a first estimate of the magnitude of the correction, yielding[2] $\Delta_{pp\mu} = 24.08 \pm (0.49)_{\Lambda_{pp\mu}} \pm (3.68)_{\lambda_{\rm op}}$ s^{-1}. The simulation method to determine $\Delta_{pp\mu}$ is similar to that used to determine the oxygen impurity correction presented in Section 4.3. The simulation takes into account the full hydrogen kinetics (including direct para-molecular state formation from the μp singlet state), the effect of oxygen in the pure hydrogen conditions, and the rate of the accidental background. The average muon disappearance rate, λ_-, also changes with the time window of the fit used for the pure hydrogen data. This illustrates that simulation is necessary to correctly assess the molecular state correction for the final MuCap result.

A series of pseudo-data histograms are generated representing 10^{14} events, compared to 10^{10} in the pure hydrogen dataset. Fits applied to the pseudo-data determine a result for the simulated value of λ_-. The change in the fit results with varying values of $\lambda_{pp\mu}$ and $\lambda_{\rm op}$ assumed in the simulation determine the molecular state correction. The magnitude of this correction as determined from simulation is $\Delta_{pp\mu} = 17.72$ s^{-1}.

The sensitivity of the correction to several important parameters is summarized in results shown in Table 7.1. The simulation results are the work of Tishenko [70]. The change in $\Delta_{pp\mu}$ when $\lambda_{pp\mu}$ and $\lambda_{\rm op}$ are independently varied by their known uncertainties is shown in the first two rows of the table. These values represent the systematic uncertainties applied to $\Delta_{pp\mu}$ in the final extraction of $\Lambda_{\rm S}$.

The lower rows of Table 7.1 illustrate the sensitivity of this correction to other input parameters: the gas density, ϕ; the value of the singlet capture rate $\Lambda_{\rm S}$ assumed in the simulation; and the concentration of oxygen, $c_{\rm O}$. The variation of the correction $\Delta_{pp\mu}$ is shown in each case to be smaller than the uncertainties due to the knowledge of $\lambda_{pp\mu}$ and $\lambda_{\rm op}$. Determining this correction requires an assumed value for $\Lambda_{\rm S}$. The change when the assumed value of $\Lambda_{\rm S}$ is varied by 10 s^{-1} is 0.25 s^{-1} and is small compared to the uncertainty induced by $\lambda_{\rm op}$. This result is an important check that applying the correction $\Delta_{pp\mu}$ itself is an unbiased procedure. The change in the correction when the concentration of oxygen is

[2]The value used for $\lambda_{\rm op}$ is the updated experimental average of $6.6(3.4) \times 10^4$ s^{-1} [4].

changed by 0.01 ppm shows that this correction is sensitive to the effects of impurities, too, which is another indication of why simulation methods are necessary.

Table 7.1: The molecular state correction, $\Delta_{pp\mu}$, with several varying conditions.

Variation of $\Delta_{pp\mu}$ From Simulation	
Variable	Change in Δ_{ppmu} [s^{-1}]
$\lambda_{pp\mu} = 1.937(59) \times 10^6$ s^{-1}	+0.51 and -0.051
$\lambda_{\rm op} = 6.6(3.4) \times 10^4$ s^{-1}	+1.64 and - 1.86
ϕ=0.0115 varied[3] by $\pm$0.0002	+0.30 and -0.31
$\Lambda_{\rm S}$ varied by $\pm$10.0 s^{-1}	+0.25 and -0.18
$c_{\rm O} = 0 \rightarrow 0.01$ ppm	+0.14

The final correction is

$$\Delta_{pp\mu} = [17.72 \pm (0.51)_{\Lambda_{pp\mu}} \pm (1.86)_{\lambda_{\rm op}}] \ {\rm s}^{-1}. \tag{7.6}$$

The correction can be compared to $\Delta^{2007}_{pp\mu} = 23.5 \pm (4.3)_{\Lambda_{pp\mu}} \pm (3.9)_{\lambda_{\rm op}}$ s^{-1}, which was used for the first MuCap result [15]. The new measurement reduces the molecular formation systematic error by a factor of nine. With the result presented in this thesis the final MuCap value for the singlet capture rate is

$$\Lambda_{\rm S}^{\rm MuCap} = [714.9 \pm (5.4)_{\rm stat} \pm (5.0)_{\rm sys}] \ {\rm s}^{-1}, \tag{7.7}$$

and the final determination of g_P,

$$g_P^{\rm MuCap}(-0.88 m_\mu^2) = 8.04(56). \tag{7.8}$$

The experimental value for g_P agrees well with the χPT prediction of $g_P^{\chi{\rm PT}}(-0.88 m_\mu^2) = 8.26(23)$ [4].

[3]Notice the magnitude of the change in ϕ that produces the reported change is twice the uncertainty actually applied to this quantity.

7.2 The Muon Transfer Rate to Argon

The argon transfer rate, $\lambda_{p\mathrm{Ar}}$, has an inconclusive experimental history, as illustrated in Table 1.2. While the present experiment determines the effective transfer rate, $\Lambda_{p\mathrm{Ar}}$, to $\approx 3.4 \times 10^{-3}$ relative precision, knowledge of the concentration of argon, c_{Ar}, and the gas density, ϕ, is a source of systematic uncertainty in determining the normalizes transfer rate, $\lambda_{p\mathrm{Ar}}$, summarized in expressions 7.2 and 7.5.

Varying experimental conditions further affect the transfer rate. One example is thermalization effects, where the effective rate of transfer can be increased at times within 100 ns of the muon stop [28]. This is illustrated by comparing the present result $\lambda_{p\mathrm{Ar}} = 2.01(12) \times 10^{11}$ s^{-1} measured at $P = 10$ bar and $c_{\mathrm{Ar}} = 19.6(1.1)$ ppm with the most recent previously reported value $\lambda_{p\mathrm{Ar}} = 1.63(9) \times 10^{11}$ s^{-1} [28] ($P = 15$ bar, $c_{\mathrm{Ar}} = 0.3\%$). The complex kinetics might be responsible for the fact that these results agree to only 2.4 σ.

The variation of $\lambda_{pp\mu}$ and $\lambda_{p\mathrm{Ar}}$ results under different experimental conditions emphasizes the necessity to make a correction for the molecular formation rate from a measurement made under conditions identical to the main MuCap experiment. The measurement of $\lambda_{pp\mu}$ presented in this thesis is minimally biased by such uncertainties. Moreover, the rate $\Lambda_{p\mathrm{Ar}}$ is not fixed in the fit to the decay electron time spectrum. This is a key advantage of the method to measure the molecular formation rate presented in this work.

7.3 The Muon Capture Rate onto Argon

The measured value of the argon capture rate, Λ_{Ar}, agrees well with the reported experimental results at the level of 1.3 σ or better. The results and current average are presented in Table 7.2.

Table 7.2: Reported experimental determinations of the argon capture rate, Λ_{Ar}.

Experimental Determinations of Λ_{Ar}	
Reference	Result [$\times 10^6$ s^{-1}]
[29]	1.31(1)
[30]	1.20(8)
[31]	1.41(11)
Present work	1.302(16)
Updated ave.	1.307(8)

Appendix A

Symbol List and Glossary

A.1 Symbol List

A compiled list of the often-used symbols representing the physical quantities measured and discussed in this work.

λ_μ	The decay rate of a muon in vacuum via the weak interaction.
Λ_{S}	The capture rate of the muon on the proton from the singlet μp state.
Λ_{T}	The capture rate of the muon on the proton from the triplet μp state.
Λ_{O}	The rate of capture for the muon from the ortho-molecular state, $\approx \frac{3}{4}\Lambda_{\mathrm{S}}$ in magnitude.
Λ_{P}	The rate of capture for the muon from the para-molecular state, $\approx \frac{1}{4}\Lambda_{\mathrm{S}}$ in magnitude.
λ_{pf}	The rate of formation for the para-molecular state from the singlet μp state, as normalized to the density of hydrogen ϕ. This rate is suppressed relative to the dominant rate of ortho-molecular state formation, $\lambda_{pp\mu}$ by a factor of $\approx 3 \times 10^{-3}$.
Λ_{pf}	The effective rate for the formation of the para-molecular state from the singlet μp state. The rate of molecular formation is proportional to the density of hydrogen, $\Lambda_{\mathrm{pf}} = \phi \cdot \lambda_{\mathrm{pf}}$.
$\Lambda_{pp\mu}$	The effective rate for the formation of the ortho-molecular state from the singlet μp state. The rate of molecular formation is proportional to the density of hydrogen, $\Lambda_{pp\mu} = \phi \cdot \lambda_{pp\mu}$.
$\lambda_{pp\mu}$	The rate of formation for the $pp\mu$ molecular state as normalized to the density of hydrogen ϕ.
ϕ	The density of hydrogen relative to the density of liquid hydrogen. Under the standard MuCap conditions this is determined to be $\phi = 0.0115(1)$.

c_{Ar} The atomic concentration of argon in the hydrogen gas. In this work the experimental condition is determined to be $c_{Ar} = 19.6(1.1)$ ppm.

$\Lambda_{p\mathrm{Ar}}$ The effective rate of muon transfer from the μp singlet state to the μAr atomic state. state. Proportional to both the gas density ϕ and the atomic concentration of argon c_{Ar} such that $\Lambda_{p\mathrm{Ar}} = c_{Ar} \cdot \phi \cdot \lambda_{\mathrm{pAr}}$.

$\lambda_{p\mathrm{Ar}}$ The normalized rate of muon transfer to Ar from the μp singlet state. This is the globally comparable, independent of experimental conditions.

Λ_{Ar} The capture rate of the μ^- onto the argon nucleus from the atomic μAr state.

$r_{\mu p}$ The total rate of muon disappearance from the μp state, where $r_{\mu p} = \lambda_\mu + \Lambda_{pp\mu} + \Lambda_{p\mathrm{Ar}} + \Lambda_{\mathrm{S}} + \Lambda_{\mathrm{pf}}$. One of two rates obtained in the capture analyses.

$r_{\mu\mathrm{Ar}}$ The effective disappearance rate of the μAr state due to both muon decay and muon capture onto the Ar nucleus, where $r_{\mu\mathrm{Ar}} = h\lambda_\mu + \Lambda_{\mathrm{Ar}}$. This is one of two rates obtained in the capture analyses.

h The factor by which the rate of muon decay changes in the μAr state, where instead of decaying with the free muon decay rate λ_μ the muon decays with a reduced rate $h\lambda_\mu$.

e_{Ar} The relative efficiency of detecting muon decay electrons from the μAr state compared to those from the μp state.

f The fraction of events in which the muon stopping in the argon-doped H gas forms a μAr atom on a prompt (≈ 10 ns) time scale.

e_{H} The relative likelihood of detecting a neutron from muon capture onto a proton compared to a neutron from capture of a muon onto an argon nucleus. The energy difference in neutrons from proton capture and neutrons from capture onto argon makes this a significant correction in the capture neutron analysis.

t_{Ar} The average time of arrival for Ar capture neutrons in the neutron detectors. Represents an important systematic parameter in the fit to the capture neutron time distribution.

s_{Ar} The average spread in the time of arrival for Ar capture neutrons in the neutron detectors. Represents an important systematic parameter in the fit to the capture neutron time distribution.

t_{H} The average time of arrival for proton (H) capture neutrons. Represents an important systematic parameter in the fit to the capture n time distribution.

s_{H} The average spread in the time of arrival for proton (H) capture neutrons. Represents an important systematic parameter in the fit to the capture n time distribution.

A.2 Glossary

μPC A 2D MWPC detector situated at the entrance of the detector. Along with the μSC it provides important information for selecting instances of good muon entrances in the experiment..

eSC A segmented plastic scintillator hodoscope detector, also arranged cylindrically around the central TPC detector.

μSC A plastic scintillator detector in two components which combined implement 25 µs pileup protection for our muon entrance events, and collimate the muon beam.

EH The EH "high" energy threshold applied in the TPC read out identifies pixels in which the muon has deposited an increasing amount of charge associated with the muon slowing in hydrogen; used to identify events in which the muon has truly stopped in the target gas.

EL The "low" energy threshold implemented on the TDC threshold discriminator readout of the MWPC plane in the TPC. This threshold identifies pixels in which the muon is moving through the hydrogen gas and depositing this minimal threshold amount of energy.

ePC Two cylindrically symmetric MWPC detectors arranged outside the TPC vessel that provide tracking information for the muon-decay electrons.

EVH The EVH "very high" threshold identifies the charge deposited by a recoiling nucleus associated with muon capture onto a $Z > 1$ element in the gas. Applied only on the read out of the anode wires of the TPC wire-chamber plane.

MORE Muon on request mode. Names the one-by-one acceptance of single muon entrance events from the muon beam into the MuCap detector.

MWPC Multi-wire proportional chamber. This acronym is applied to detectors which work on the principle of placing anode and cathode wires under high (kV-scale) voltage in a volume filled with gas. A charged particle like a muon or electron traveling through the detector ionizes the chamber gas and this charge deposition induces an electrical pulse on the chamber wires. This facilitates a detection method for charged particles that also allows 3-D tracking.

pileup When two muons enter the detector within 25 µs of each other that event is a pileup event. The experiment implements pileup protection to ensure a one-by-one mode for muon stop events in the detector, or the MORE mode.

pixel A two-dimensional unit for the TPC detector. It represents a 200 ns time bin of a pulse on a single wire of the MWPC chamber that has been discriminated to be at at least the EL energy threshold. This forms a fundamental unit for the distribution of charge in the TPC and describing the muon stop events in the target.

PSI The Paul Scherrer Intitute, the laboratory home of the MuCap experiment in Villigen, Switzerland.

TDC Time-to-digital converter..

TPC Time projection chamber. The central detector is a target of hydrogen gas but also acts as an active volume, allowing a central component of our analysis: the identification and selection of muon stop events.

References

[1] K. Nakamura et al. 2011 Review of particle physics. *J. Phys. G*, 37:075021, 2010.

[2] D. M. Webber et al. Measurement of the positive muon lifetime and determination of the Fermi constant to part-per-million precision. *Phys. Rev. Lett.*, 106:041803, 2011.

[3] V. Bernard et al. Axial structure of the nucleon. *J. Phys. G*, 28:R1–R35, 2002.

[4] P. Kammel and K. Kubodera. Precision muon capture. *Annu. Rev. Nucl. Part. Sci.*, 60:327–353, 2010.

[5] T. Gorringe and H. W. Fearing. Induced pseudoscalar coupling of the proton weak interaction. *Rev. Mod. Phys.*, 76(1):31 – 91, 2003.

[6] A. Czarnecki et al. Electroweak radiative corrections to muon capture. *Phys. Rev. Lett.*, 99:032003, 2007.

[7] T.S. Jensen and V.E. Markushin. Collisional de-excitation of exotic hydrogen atoms in highly excited states. I. Cross-sections. *Eur. Phys. J. D*, 21:261–270, 2002.

[8] T.S. Jensen and V.E. Markushin. Collisional de-excitation of exotic hydrogen atoms in highly excited states. II. Cascade calculations. *Eur. Phys. J. D.*, 21:271–283, 2002.

[9] J.S. Cohen. Improved adiabatic calculation of muonic-hydrogen-atom cross section. I. Isotopic exchange and elastic scattering in asymmetric collisions. *Phys. Rev. A*, 43:4668, 1991.

[10] S. S. Gershtein and L. I. Ponomarev. *Muon Physics*, volume 3 - Chemistry and Solids, chapter VII, pages 142–225. Academic Press, Inc., 1975.

[11] M.P. Faifman. Nonresonant formation of hydrogen isotope mesic molecules. *Muon Catal. Fusion*, 4:341–364, 1989.

[12] G. Bardin et al. Measurement of the ortho-para transition rate in the $p\mu p$ molecule and deduction of the pseudoscalar coupling constant. *Phys. Lett. B*, 104:320, 1981.

[13] J. H. D. Clark et al. Ortho-para transition rate in μ-molecular hydrogen and the proton's induced pseudo scalar coupling g_p. *Phys. Rev. Lett.*, 96:073401, 2006.

[14] D.D. Bakalov et al. μ-capture and ortho-para transitions in the muonic molecule $pp\mu$. *Nucl. Phys. A*, 384:302–322, 1982.

[15] V. A. Andreev et al. Measurement of the rate of muon capture in hydrogen gas and determination of the proton's pseudoscalar coupling $g_{\rm p}$. *Phys. Rev. Lett.*, 99(032002), 2007.

[16] D. H. Wright et al. Measurement of the induce pseudoscalar coupling using radiative muon capture on hydrogen. *Phys. Rev. C*, 57(1):373–389, 1998.

[17] G. Bardin et al. A novel measurement of the muon capture rate in liquid hydrogen by the lifetime technique. *Nucl. Phys. A*, 352:365–378, 1981.

[18] T. Suzuki et al. Total nuclear capture rates for negative muons. *Phys. Rev. C*, 35(6):2212 – 2224, 1987.

[19] E. J. Bleser et al. Muonic molecules in liquid hydrogen. *Phys. Rev.*, 132(6):2679–2691, 1963.

[20] G. Conforto et al. Direct measurement of μ^--mesonic molecule formation rates in liquid hydrogen. *Phys. Rev. Lett.*, 9(10):432 – 434, 1962.

[21] V. M. Bystritskii et al. Direct measurement of the rates of formation of the molecules ppμ and pdμ in gaseous hydrogen. *Sov. Phys. JETP*, 43(4):606 – 611, 1976.

[22] F. Mulhauser et al. Measurement of muon transfer from proton to triton and ppμ molecular formation in solid hydrogen. *Phys. Rev. A*, 53(5):3069 – 3079, 1996.

[23] S. Cohen. Mu-mesonic molecules. I. Three-body problem. *Phys. Rev.*, 119(1):384–397, 1960.

[24] L. I. Ponomarev and M. P. Faifman. Calculation of rates of formation of μ-mesic hydrogen molecules. *Sov. Phys. JETP*, 44(5):886 – 891, 1976.

[25] J. D. Jackson. *Classical Electrodynamics*, chapter 9, pages 442–444. John Wiley and Sons, Inc., 3rd edition, 1999.

[26] A. Alberigi et al. Measurement of the transfer rates of muons from hydrogen to xenon and some other monatomic elements. *Nuovo Chimento B*, 47:92, 1967.

[27] L.A. Schaller and C. Petitjean, editors. *Muonic Atoms and Molecules*, pages 209–215. Birkhauser, 1993.

[28] R. Jacot-Guillarmod et al. Muon transfer from thermalized muonic hydrogen isotopes to argon. *Phys. Rev. A*, 55(5):3447–3452, 1997.

[29] T.N. Mamedov et al. Total rates of nuclear capture of negative muons in the isotopes ^{132}Xe and ^{40}Ar. *JETP Lett.*, 69(3):192 – 195, 1999.

[30] A. Bertic et al. Nuclear capture of muon in argon and neon. *Phys. Rev. A*, 7:2214, 1973.

[31] G. Carboni et al. Muonic X-rays and muon capture in low-pressure argon. *Phys. Lett. B*, 96B:206–208, 1980.

[32] F. Bienz et al. Transfer of negative muons from hydrogen to argon in gaseous H_2+Ar mixtures at high pressure. *J. Phys. B. At. Mol. Opt. Phys.*, 21:2725–2735, 1988.

[33] R. Jacot-Guillarmod et al. Muon transfer from hydrogen to argon and helium at 10-15 bars. *Phys. Rev. A*, 38(12):6151, 1988.

[34] E. Iacopini. A new measurement of the muon transfer rate from muonic hydrogen to argon. *Nuovo Chimento A*, 67:201, 1982.

[35] H. Daniel et al. Direct measurement of the transfer rate $p\mu + \mathrm{Ar} \rightarrow p + \mathrm{Ar}\mu$ at high gas pressure. *Nucl. Phys.*, A435:409–412, 1980.

[36] M. J. Barns and G. D. Waite. A 25-kV 75-kHz kicker for measurement of muon lifetime and a determination of the Fermi constant. *Plasma Science, IEEE Transactions on*, 32(5):1932–1944, 2004.

[37] B. Kiburg. *A Measurement of the Rate of Muon Capture In an Ultra-Pure Protium Gas Time Projection Chamber*. PhD thesis, University of Illinois at Urbana-Champaign, 2011.

[38] T. Banks. *A Measurement of the Rate of Muon Capture Hydrogen Gas and Determination of the Proton's Induced Pseudoscalar Coupling g_P*. PhD thesis, University of California at Berkeley, 2007.

[39] I. Alekseev et al. Deuterium removal unit for the MuCap experiment. Presented at the NHA Annual Hydrogen Conference, Sacramento, CA, 2008.

[40] V.A. Ganzha et al. A circulating hydrogen ultra-high purification system for the MuCap experiment. *Nucl. Instrum. Meth. A*, 578:485–497, 2007.

[41] P. Kravtsov and V. Tischenko. Sensor calibration errors and readout system. Private Communication, June 2012.

[42] NIST website for calculating thermodynamic properties of fluid systems. http://webbook.nist.gov/chemistry/fluid/.

[43] J. Egger et al. The 10 bar hydrogen time projection chamber of the MuCap experiment. *Nucl. Instrum. Meth. A*, 628:199–203, 2011.

[44] G. F. Knoll. *Radiation Detection and Measurement*, chapter 15, pages 558–565. John Wiley and Sons, Inc., 3rd edition, 2000.

[45] M. Moszynski et al. Study of n-γ discrimination by digital charge comparison method for a large volume liquid scintillator. *Nuc. Instrum. Meth.*, A317:262–272, 1992.

[46] R. A. Cecil et al. Improved predictions of neutron detection efficiency for hydrocarbon scintillators from 1 MeV to 100 MeV. *Nuc. Instrum. Meth.*, 161:439–447, 1979.

[47] M. Moszynski et al. Comparative study of new 130 mm diameter fast photomultipliers for neutron detectors. *Nuc. Instrum. Meth.*, A307:97–109, 1991.

[48] F. Gray. Hardware upgrades - new FADC electronics. MuCap 2006 PSI Progress Report, 2006.

[49] MIDAS software framework website. http://midas.psi.ch.

[50] The ROOT software package website. root.cern.ch.

[51] S. Clayton. *MEASUREMENT OF THE RATE OF MUON CAPTURE IN HYDROGEN GAS AND DETERMINATION OF THE PROTON'S PSEUDOSCALAR COUPLING*. PhD thesis, University of Illinois at Urbana-Champaign, 2007.

[52] T. Gorringe. Detector set-up and pulse discrimination calibration. Private Communication, October 2007.

[53] Y.-A. Thalmann et al. Investigation of charge transfer from excited muonic hydrogen atoms to argon. *Phys. Rev. A*, 56(1):468–472, 1997.

[54] R. W. Huff. Decay rate of bound muons. *Ann. Phys. (N.Y.)*, 16(2):288–316, 1961.

[55] H. Überall. Decay of μ^- mesons bound in the K shell of light nuclei. *Phys. Rev.*, 119(1):365, 1960.

[56] C.E. Porter and H. Primakoff. The effect of Bohr orbit binding on negative μ-meson β-decay. *Phys. Rev.*, 83(4):849–850, 1951.

[57] W.R. Johnson, R.F. O'Connell, and C. J. Mullin. Coulomb field effects on the decay of bound polarized muons. *Phys. Rev.*, 124(3):904–908, 1961.

[58] R. Watanabe et al. Asymmetry and energy spectrum of electrons in bound-muon decay. *At. Data and Nucl. Data Tables*, 54:165–178, 1993.

[59] R. Watanabe et al. Angular distribution of electrons in bound muon decay. *Prog. Theor. Phys.*, 78(1), 1987.

[60] A. Grossheim et al. Decay of negative muons bound in ^{27}Al. *Phys. Rev. D*, 80(5):052012 – 052019, 2009.

[61] A. Czarnecki et al. Muon decay in orbit: Spectrum of high-energy electrons. *Phys. Rev. D.*, 84(1):013006, 2011.

[62] J. Phillips. Simulation of electron detection efficiency versus energy. Private Communication, September 2011.

[63] GEANT4 software package website. http://geant4.cern.ch/.

[64] L. Schellenberg. Muon transfer in gas mixtures with hydrogen. *Muon Catal. Fusion*, 5:73–85, 1990.

[65] A. Werthmuller et al. Energy dependence of the charge exchange reaction from muonic hydrogen to oxygen. *Hyperfine Interact.*, 116:1, 1998.

[66] F. James and M. Goossens. MINUIT - Function minimization and error analysis. CERN Program Library entry D506, CERN, 1992.

[67] P. Kammel. Anode wire efficiency. Private Communication, June 2012.

[68] T. Gorringe. Neutron background subtraction procedure. Private Communication, January 2011.

[69] D. F. Measday and T. J. Stocki. Comparison of muon capture in light and in heavy nuclei. In *VII Latin American Symposium on Nuclear Physics and Applications*, number CP947, pages 253 – 257. American Institute of Physics, 2007.

[70] V. Tishenko. Simulation results for determining the molecular state correction for the extraction of singlet capture rate. Private Communication, June 2012.